Dissertation
submitted to the
Combined Faculties of the Natural Sciences and for
Mathematics
of the Ruperto–Carola University of Heidelberg, Germany
for the degree of
Doctor of Natural Sciences

Put forward by
Sean R. McConnell M.app.Sc.
Born in Brisbane, Australia
Oral examination: January 9th, 2013

Two centre problems in relativistic atomic physics

Referees: Priv.–Doz. Dr. Andrey Surzhykov
Prof. Dr. Dirk Schwalm

Units and constants

In the following table, a list of fundamental constants is given with their corresponding values in standard international, atomic and natural units. The column for atomic units represents by what factor the SI values in column 3 must be multiplied by to obtain the unit value for atomic units.

Table 1: Some fundamental quantities in natural units (N.U.) and their standard international (S.I.) and atomic units (A.U.) equivalents. The dimensionless fine structure constant α has the value $1/137.035999074(44)$

Constant	Label	SI	Atomic	Natural
Speed of light	c	299792458 ms^{-1}	α	1
Unit mass	m_e	$9.1093815 \times 10^{-31}$ kg	1	1
Unit time	$\frac{\hbar}{m_e c^2}$	$1.28808866 \times 10^{-21}$ s	$\frac{1}{\alpha^2}$	1
Unit length	αa_0	$3.86159265 \times 10^{-13}$ m	$\frac{1}{\alpha}$	1
Unit charge	$\frac{e_c}{\sqrt{\alpha}}$	$1.87554587 \times 10^{-18}$ C	$\sqrt{\alpha}$	1
Unit energy	$m_e c^2$	$8.18710438 \times 10^{-}14$ J	α^2	1

The atomic unit system takes the neutral Hydrogen atom as its standard and was conceived in order to simplify the Schrödinger equation. The binding energy of the ground state of the Hydrogen atom, the Bohr radius, the expectation value of the velocity of the electron in the ground state, to mention but a few measures, are all taken as unity in atomic units. In atomic units, the speed of light is equal to α.

Natural units on the other hand, are more centred on the properties of the electron as the basic unit. Natural units serve to simplify the Dirac equation, in the same way the Schrödinger equation is simplified by atomic units. The electron rest mass, the speed of light, and $\hbar$ are all set to unity. The fundamental constant equal to α is the square of the electronic charge e.

Publications

The author has contributed to the following publications

- S. R. McConnell, S. Fritzsche, and A. Surzhykov, "Dirac: A new version of computer algebra tools for studying the properties and behavior of hydrogen–like ions," *Comput. Phys. Commun.*, vol. 181, no. 3, pp. 711–713, 2010.

- S. R. McConnell, A. N. Artemyev, and A. Surzhykov, "Alignment of atomic inner–shells following alpha–decay–induced ionization," *J. Phys. B: At., Mol., Opt.*, vol. 44, no. 14, p. 145204, 2011.

- A. N. Artemyev, S. R. McConnell, A. Surzhykov, B. Najjari, and A. B. Voitkiv, "Coulomb excitation of highly charged projectile ions in relativistic collisions with diatomic molecules," *Phys. Rev. A*, vol. 84, p.042709, Oct 2011.

- S. R. McConnell, A. N. Artemyev, M. Mai, and A. Surzhykov, "Solution of two–center time–dependent Dirac equation in spherical coordinates: Application of the multipole expansion of the electron–nuclei interaction," *Phys. Rev. A*, 2012. *Accepted on 26 October 2012*, Available online: *arXiv:1208.4731v3 [physics.atom-ph]*

- S. R. McConnell, A. N. Artemyev, and A. Surzhykov, "Treatment of U^{92+}–U^{91+} collisions in spherical coordinates: Going beyond the monopole approximation," *Phys. Scripta*, 2012. *Accepted on 21 October 2012*

Abstract

The work contained within this thesis is concerned with the explanation and usage of a set of theoretical procedures for the study of static and dynamic two–centre problems in the relativistic framework of Dirac's equation. Two distinctly different theories for handling time–dependent atomic interactions are reviewed, namely semi–classical perturbation theory and a non–perturbative numerical technique based on the coupled channel equation to directly solve the time–dependent, two–centre Dirac equation. The non–perturbative numerical technique has been developed independently and the calculations performed with it are entirely new. Calculations for ionisation cross sections and state occupancies are conducted for both these methods.

The non–perturbative technique for relativistic two–centre problems is extensively explained and, given its novelty, a probity test is conducted between this technique and that of the well established perturbation theory in calculating K– and L–shell ionisation cross sections for the alpha decay of initially *Hydrogen–like* Polonium.

To that end, an in depth outline of the perturbative technique is also made for both collision and decay processes. As well as the comparison test mentioned, this technique is also applied to the analysis of cross sections of the promotion of a single electron into the positive continuum from either a K– or L–shell due to the alpha decay of heavy, *neutral* nuclei (Gadolinium, Polonium and Thorium). Dirac–Coulomb eigenfunctions centred on the parent nucleus of the decay pair are taken as the basis for use in the cross section calculations utilising first order, semi–classical pertubation theory.

The excellent congruence between both techniques justifies the usage of the non–perturbative algorithms in the subsequent analysis of collisions between very heavy, highly charged ions. As such, a set of calculations are performed examining the bound and continuum state occupancy of the electronic levels during a collision between U^{92+}–U^{91+}, at both over–critical and non–critical projectile velocities.

Overall, the non–perturbative method developed and implemented here, is shown to be reliable, compares well with available experimental data, and most importantly is flexible enough to find continued use in studies on more extreme/exotic atomic systems.

Zusammenfassung

Diese Arbeit beschäftigt sich mit der Erklärung und Umsetzung einer Reihe von theoretischen Verfahren, die der Untersuchung von statischen und dynamischen Zweikernproblemen im relativistischen Rahmen der Dirac Gleichung dienen. Zwei gänzlich verschiedene Theorien zur Behandlung von zeitabhängigen atomaren Wechselwirkungen werden näher untersucht, nämlich, halbklassiche Störungstheorie und ein nicht perturbatives numerisches Verfahren, das auf der coupled channel Gleichung basiert und die zeitabhängige Zweikern–Diracgleichung direkt löst. Das nicht perturbative Verfahren ist eine eigenständige Erzeugung, Berechnungen die damit erstellt werden sind also ganz neu. Ionisierungsquerschnitte und Zustandsbesetzungen für die beiden erwähnten Methoden werden berechnet.

Der nicht perturbativen Technik für relativistische Zweikernprobleme wird eine umfangreiche Erklärung gewidmet und, da diese Technik neu ist, wird eine Integritätsprüfung durchgeführt. Dies geschieht, indem die mit dieser Technik erhaltenen Resultate mit Resultaten der bewährten Störungstheorie, angewendet auf K– und L–Schalenionisierungsquerschnitte infolge des Alphazerfalls eines anfangs wasserstoffähnlichen Poloniumkerns, verglichen werden.

Zu diesem Zweck wird eine umfassende Erläuterung der perturbativen Technik für Stoß– und Zerfallsprozesse vorgestellt. Diese Methode wird sowohl für die oben genannte Integritätsprüfung angewandt, als auch auf die Analyse des Ionisierungsquerschnitts eines Elektrons aus einer K– oder L–Schale, das infolge des Alphazerfalls eines anfangs hochgeladenen, *neutralen* Kerns (Gadolinium, Polonium, Thorium), geschieht. Dirac–Coulomb Eigenfunktionen, die am Spendekern des Zerfallspaares zentriert sind, werden hier als Basis in der ersten Ordnung halbklassischer Störungstheorie der Querschnittsberechnungen verwendet.

Die herausragende Übereinstimmung der beiden Methoden rechtfertigt die anschließende Anwendung des nicht perturbativen Algorithmus zur Analyse von Stößen zwischen sehr schweren, hochgeladenen Ionen. Deswegen wird eine Reihe von Berechnungen bewerkstelligt, bei der die Besetzungen der gebundenen und kontinuuierlichen elektronischen Zustände während eines Stoßes zwischen U^{92+}–U^{91+} für über– und nicht kritische Projektilgeschwindigkeiten untersucht werden.

Die entwickelte nicht perturbative Methode, die hier umgesetzt wird, stellt sich insgesamt als zuverlässig heraus, eignet sich gut um die verfügbaren experimentellen Daten zu beschreiben und ist vor allem genügend flexibel um in zukünftigen Studien von extremeren/exotischeren atomaren Systemen noch eine Verwendung zu finden.

Acknowledgements

I'll deal with the dry stuff straight up: I'd like to extend my thanks to the Heidelberg graduate school of fundamental physics and to the International Max Planck research school in Heidelberg for allowing me to pursue my doctoral studies and for providing me with financial support.

To my supervisor and his partner in crime: Andrey Surzhykov and Anton Artemyev, I extend my most heartfelt gratitude. You have been my teachers over the past few years and I have learnt more about fundamental physics and programming from you than I ever anticipated. I really didn't know as much about our world as I thought I did before I came to Heidelberg, you have helped me open my eyes.

To the current and former colleagues and friends in my group and at Uni: Lalita Sharma, Filippo Fratini, Michael Siomau, Thorsten Jahrsetz, Manuel Mai, Oliver Matula, Jonas Gunst, Armen Hayrapetyan, Vlad Hahn and Sebastian Höltkemeier, thankyou for the enlightening discussion, your friendship und dass ihr mich Deutsch beigebracht habt, but mostly thanks for just being who you are, you are all awesome and it has been my honour to have spent (and hopefully continue to spend) so much time with you.

To my friends outside of the Uni: Sebastian Härle, Marc Jähnchen and Joice Biazoto, Veerle Sterken, Oli Krümmelbein and Karina Rickert, Gundi Pawasserat and all those in the short–track section of M.E.R.C and everyone I've ever lived with in Weingasse 24, you all have my thanks, it's an honour to have friends such as yourselves. You've all contributed to keeping me fit, happy and most importantly relaxed. A special thankyou goes to the two people who befriended me only a few weeks after arriving in Germany, Annika Neygenfind and Volker Theil, your selfless love and friendship I won't ever forget.

To my parents Diana and Iain: you've done everything for myself and my sister Natalie, so of course you have my deepest gratitude. It's unfortunate that neither of you will be able to fully comprehend the fruits of your labours, in terms of what is contained within this book at least, so I hope it's enough simply to tell you, I couldn't have written a single word, solved any equation, written any programs without your inspiration and your love. The content of this thesis I dedicate to you both.

List of Figures

List of Tables

Contents

Chapter 1

Introduction

In the study of atomic collisions, under certain circumstances, the electronic motion of the system can not be satisfactorily described by a basis of wavefunctions which are expanded about a single centre. After certain thresholds during an atomic collision, such as, when the projectile(s) passes within the radius of the target ground state *and* possesses a charge roughly equivalent to that of the target, only molecular wavefunctions can be used to describe the electronic state of this short–lived, so called "quasi–molecule." This represents a shift from the atomic two–body problem, to a three– or more body problem.

In the Schrödinger picture of non–relativistic quantum mechanics, systems where the electrons move at velocities small in comparison with c, approximate and complete solutions to the static and dynamic, atomic, three body problem, and its higher order derivatives, are already well elucidated. These solutions are employed in the study of molecular systems of at least two nuclei, a single nucleus to which multiple electrons are bound or even combinations of multiple centres and electrons. In spite of the comparatively rapid progress made in non–relativistic atomic physics regarding many body problems, the rate of development in relativistic many body problems, particularly concerning systems with multiple nuclei, has been understandably slower. In fact, the degree of complexity inherent with merely a relativistic two–centre system with a single electron is enough to render any further discussion of more complex configurations exceedingly precocious. To address this, the theory presented in this work focusses exclusively on relativistic atomic systems within Dirac's [1] framework which contain two nuclei[1]. It should be therefore noted, that the treatment made in this work comes at the exclusion of an explicit account of the typical corrections to the Schrödinger equation, i.e. Spin–Orbit coupling, the Darwin term or the relativistic correction to the kinetic energy, these can be found elsewhere [2].

[1] The term "relativistic atomic system" applies to systems containing a nucleus of charge Z, such that $\mathrm{O}(\alpha Z) \sim 1$

An important part of the exploration of this problem necessarily begins with a short recapitulation of the theoretical groundwork already performed in the treatment of the time–dependent and –independent two–centre problem. Not long after the advent of Schrödinger's equation, successful attempts had already been made at deriving a solution for the Hydrogen molecular ion [3, 4, 5, 6, 7, 8, 9, 10, 11, 10]. These solutions were found mostly using elliptic coordinates, or less often using the linear combination of atomic orbitals method (LCAO).

Within the relativistic regime, on the other hand, exact eigenfunctions and eigenvalues for a Hydrogen–like atom were first discovered in 1928 [12]. Since that time, progress has been slow in the development of a solution to the Dirac equation for two coulomb centres. It was only in the late 1960's that considerable strides were made to find a solution to the two–centre problem in the relativistic framework. Mostly, the results of the Greiner group [13, 14, 15, 16, 17, 18, 19, 20], among others [21], form the bulk of the initial research conducted in this field, which has predominantly relied upon a multipole expansion of the two–centre potential, in order to conserve the use of spherical coordinates. Furthermore, the possibility and plausibility of conducting experiments [22] to test this theory has fed the rising interest in this field in more recent times. Other authors have managed to derive solutions to the two–centre problem in more exotic coordinate systems, such as elliptic hyperbolic and even Cassini coordinates [23, 24, 20].

The major hurdle regarding two–centre problems within the relativistic framework is that no single choice of coordinate system can significantly simplify the problem in the same way that can be done for non–relativistic two–centre problems. Solutions to the Schrödinger equation for two–centre systems are usually found using elliptical coordinates either via an action minimisation procedure or quasi–analytically [4]. If a solution to the two–centre problem is to be found within the relativistic regime, the hand of the theoretician is forced to turn towards approximation methods. It is principally for this reason why the relativistic development of two–centre problems lags well behind its non–relativistic equivalent.

The approach developed for the solution of the time–independent, two–centre Dirac equation here is similar to the established technique of maintaining the use of spherical coordinates, expanding the two–centre potential in multipoles, and seeking eigenfunctions in terms of a sum over partial waves. This original procedure differentiates itself from other previous attempts at solving the static problem by using a two step approach. Firstly, a basis of eigenfunctions are generated which satisfy the monopole approximation to the two–centre potential, these monopole eigenfunctions are then re–used in the generation of a true two centre basis. Some advantages of this method, over other more direct approaches, are that the computational time is sharply reduced and the matrix elements involving eigenfunctions generated in spherical coordinates are already

well explained and easy to work with.

These static solutions are then used in the time–dependent Dirac equation to model cross sections of ionisation and excitation due to the collision of two heavy nuclei. The coupled channel equation, a type of finite element analysis, maps the static eigenfunctions onto a discretised time grid. This implementation of these pure two–centre eigenfunctions in the solution of the time–dependent Dirac equation is also completely new.

Assuming for the moment that one possesses solutions to the two–centre problem in the relativistic regime, one must be aware of how these solutions can be applied to real world interests. Obviously studies on charge exchange, eigenvalue spectrum classification and QED investigations for two centres could be of potential interest, however, the dynamic atomic systems chosen for investigation focus exclusively on the calculation of excitation and ionisation cross sections as a result of ion–ion collisions. The main task of this work is therefore to model a collision between two heavy, highly charged ions, and to predict the effects the collision has on a single bound electron. The ions chosen for this task are U^{92+} and U^{91+}.

Since this numerical procedure for the solution of the time–dependent, two–centre Dirac equation is new, a comparison with another proven, established technique must be conducted in order to verify the probity of this new approach. To that end, first order, time–dependent perturbation theory will be employed in the calculation of ionisation probabilities of an electron in the K– and L–shells of an initially Hydrogen–like, heavy nucleus which undergoes alpha decay. Accordingly, the numerical procedure will then be used to evaluate these probabilities and the results obtained from each approach will be compared. It should also be noted that the results extracted from perturbation theory are also partially original, usage of the Lienerd–Wiechert potential to account for the electron–alpha particle coulomb interaction and the relativistic recoil operator have not been applied previously to the study of alpha decay of heavy nuclei. As will be shown, the agreement between both approaches is quite convincing, and justifies the use of the numerical procedure in an investigation of a collision between very heavy, highly charged ions.

Having established then a broad scope for what is to come, it would be prudent to give a more concise overview of the forthcoming elucidation and realisation of a working two–centre theory. In preparation for the computational results which follow, a solid theoretical outline of relativistic atomic theory for single–centre problems will be presented first, both exact and numerical approaches will be treated. Though the single–centre solutions are simpler in nature, the formulation thereof exhibits a greater degree of familiarity which should make the extension to two–centre theory less conceptually challenging for the reader; moreover, the solution to the single–centre Dirac equation anyway forms the

basis for solving two–centre problems using perturbation theory.

Logically extending from here, the theory for the numerical solution of the two–centre Dirac equation will be explained for the time–independent case, after which, the finite element approach to the time–dependent two–centre Dirac equation (otherwise known as the coupled channel equation) will be explored and elucidated. An examination of time–dependent perturbation theory for two–centre problems then follows. The computational implementation of this theory will also receive some attention.

Finally, as mentioned, the electronic effects of the alpha decay of heavy atoms (section 6.1) will be explored using perturbation theory for a selection of nuclear spin–zero elements (Gadolinium, Polonium and Thorium) known to be susceptible to alpha decay. Specifically, the non–perturbative theory will be compared directly to the results garnered from perturbation theory for the alpha decay of Polonium. Furthermore, given that the comparison test is conducted for an initially Hydrogen–like ion, perturbation theory will also be used to investigate the same ionisation cross sections for neutral atoms, in order to lend this examination a greater link to naturally occurring elements as well as to give this work more experimental relevance. Finally, collisions between heavy, highly charged ions (section 6.2) for collision energies that both do and do not cause the diving of the ground state into the negative energy continuum will be examined given the exciting possibilities systems of heavy quasi–molecules offer for the spontaneous production of electron–positron pairs.

The overarching desire is that the reader will be able to clearly recognise and follow the increasing steps in complexity, firstly from the single–centre theory, to perturbation theory to non–perturbative theory. Not only this, but it will hopefully become clear to the reader, how one may, with minimal resistance, incorporate further degrees of freedom, such as non–zero impact–parameters or the presence of electromagnetic fields, into the two–centre problem and generate a truly *dynamic* method for modelling real world, relativistic two–centre systems.

Unless otherwise stated, all equations, tables and figures are presented in natural units (N.U.) ($\hbar = m_e = c = 1$)

Chapter 2

The relativistic single–centre problem

2.1 Analytic methods

The first step in the journey toward a full solution of the two–centre Dirac equation must surely begin with a brief recap of the analytic solutions to the single–centre problem for a single electron. More importantly for what is to come, an in depth look at how one may generate numeric solutions to the single–centre problem will also be provided. It is imperative that both methods be compared, and only if the numerical solutions show acceptable agreement with the analytic solutions, in terms of eigenvalues and eigenfunctions, can it then be used in the further development of a true two–centre basis.

All of the *analytic* equations elaborated upon in this section have been implemented in the *Mathematica* program *Dirac* [25, 26]. This program, and its in–built equations are used in the calculations presented in section 6.1; a very brief discussion of the program and its capabilities may be found in the appendix C.

The single–centre Dirac equation, where a single electron is acted upon only by a central field, is inherently a time–independent problem. All the properties of the system can be derived from the Dirac equation, which in spherical coordinates is given by

$$\hat{\mathbf{H}}\phi(\mathbf{r}) = E\phi(\mathbf{r}). \tag{2.1}$$

The form of the Hamiltonian in equation (2.1), for a spin $\frac{1}{2}$ particle acted upon by an external scalar field $V(r)$ is given by

$$\hat{\mathbf{H}} = \boldsymbol{\alpha} \cdot \mathbf{p} + V(r) + \boldsymbol{\beta}. \tag{2.2}$$

The various symbols contained within equation (2.2) are defined in A.1.

2.2 The coulomb field

For an electron in the vicinity of a single, point–like nucleus of positive charge Z for $Z < 137$, the central potential $V(r)$ reduces to

$$V(r) = -\frac{\alpha Z}{r}. \tag{2.3}$$

A complete disquisition of the methods of coordinate separation of equation (2.1) for central fields will not be provided here, ample resources exist already which may help in this regard, cf. [27, 28], after all, the salient features of any fundamental differential equation in quantum mechanics for the practitioner are always its eigenvalues and eigenfunctions, not specifically the mathematical methods for the treatment of partial differential equations.

Taking the z–axis as the quantisation axis, the separation ansatz used in determining the eigenfunctions and eigenvectors for equation (2.1) is

$$\phi(\mathbf{r}) \equiv \phi_{\kappa m_j}(\mathbf{r}) = \begin{pmatrix} g_\kappa(r)\,\chi_\kappa^{m_j}(\hat{\mathbf{r}}) \\ i f_\kappa(r)\,\chi_{-\kappa}^{m_j}(\hat{\mathbf{r}}) \end{pmatrix}, \tag{2.4}$$

where κ is the spin–orbit quantum number, and m_j is the projection of the total angular momentum of the electron onto the z–axis; the radial functions $g_\kappa(r)$ and $f_\kappa(r)$ are colloquially known as the "large" and "small" components respectively. The spinors $\chi_\kappa^{m_j}(\hat{\mathbf{r}})$ may be expressed as

$$\chi_\kappa^{m_j}(\hat{\mathbf{r}}) = \sum_{\mu=\pm\frac{1}{2}} \left\langle \begin{array}{cc|c} l & \frac{1}{2} & j \\ m_j-\mu & \mu & m_j \end{array} \right\rangle Y_{l,m_j-\mu}(\hat{\mathbf{r}}) \begin{pmatrix} \delta_{1/2,\mu} \\ \delta_{-1/2,\mu} \end{pmatrix}, \tag{2.5}$$

where

$$j = |\kappa| - \frac{1}{2} \quad \text{and} \quad l = \begin{cases} -\kappa - 1 & \kappa < 0 \\ \kappa & \kappa > 0 \end{cases}, \tag{2.6}$$

are the electron total angular momentum and orbital angular momentum quantum numbers respectively, the term in equation (2.5) in bra–ket parenthesis is a Clebsch–Gordan coefficient, and $Y_{l,m_j-\mu}(\hat{\mathbf{r}})$ are the spherical harmonics. From equation (2.6) it is possible to conclude that κ can assume any positive or negative integer value not equal to zero. Furthermore, states of even parity are those with $\kappa = -1, 2, -3, 4...$ and odd parity $\kappa = 1, -2, 3, -4....$ Insertion of equation (2.4) into (2.1) will yield the following differential equation for the radial solutions $G_\kappa(r) = r g_\kappa(r)$ and $F_\kappa(r) = r f_\kappa(r)$

$$\begin{aligned} \left(\frac{\mathrm{d}F_\kappa(r)}{\mathrm{d}r} - \frac{\kappa}{r}F_\kappa(r)\right) &= -\left(E - V(r) - 1\right) G_\kappa(r) \\ \left(\frac{\mathrm{d}G_\kappa(r)}{\mathrm{d}r} + \frac{\kappa}{r}G_\kappa(r)\right) &= \left(E - V(r) + 1\right) F_\kappa(r). \end{aligned} \tag{2.7}$$

For bound–state solutions, i.e. $-1 < E < 1$, with the help of the following notation

$$\xi^2 = \kappa^2 - \zeta^2, \quad \zeta = \alpha Z, \quad E_{n\kappa} = \frac{1}{\sqrt{1 + \left(\frac{\zeta}{n - |\kappa| + \xi}\right)^2}} \quad \text{and}$$

$$k = \sqrt{1 - E_{n\kappa}^2}, \tag{2.8}$$

solutions for $f_\kappa(r)$ and $g_\kappa(r)$ can be derived from (2.7) that take the following form

$$\begin{aligned} g_\kappa(r) &= N(2kr)^{\xi-1} e^{-kr} \Bigg((|\kappa| - n)\ {}_1F_1(|\kappa| - n + 1, 2\xi + 1; 2kr) - \\ &\quad \left(\kappa - \frac{\zeta}{k}\right)\ {}_1F_1(|\kappa| - n, 2\xi + 1; 2kr) \Bigg) \\ f_\kappa(r) &= -N(2kr)^{\xi-1} e^{-kr} \Bigg((n - |\kappa|)\ {}_1F_1(|\kappa| - n + 1, 2\xi + 1; 2kr) - \\ &\quad \left(\kappa - \frac{\zeta}{k}\right)\ {}_1F_1(|\kappa| - n, 2\xi + 1; 2kr) \Bigg) \sqrt{\frac{1 - E_{n\kappa}}{1 + E_{n\kappa}}}, \end{aligned} \tag{2.9}$$

where N is, using the integral condition

$$\int_0^\infty G_\kappa(r)^2 + F_\kappa(r)^2 \, \mathrm{d}r = 1, \tag{2.10}$$

determined to be

$$N = \frac{\sqrt{2} k^{5/2}}{\Gamma(2\xi + 1)} \sqrt{\frac{\Gamma(2\xi + n - |\kappa| + 1)(1 + E_{n\kappa})}{(n - |\kappa|)! \zeta (\zeta - \kappa k)}}. \tag{2.11}$$

If on the other hand $E > 1$, a *partial wave solution* for the radial coordinate of $\phi_{\kappa m_j}(\mathbf{r})$ contains representations for $f_\kappa(r)$ and $g_\kappa(r)$ as per

$$\begin{aligned} g_\kappa(r) &= N\sqrt{E + 1}\,(2kr)^{\xi-1} \\ &\quad \Re\left[e^{-i(kr - \delta_\kappa)}(\xi + i\eta)\ {}_1F_1(\xi + 1 + i\eta, 2\xi + 1; 2ikr)\right] \\ f_\kappa(r) &= -N\sqrt{E - 1}\,(2kr)^{\xi-1} \\ &\quad \Im\left[e^{-i(kr - \delta_\kappa)}(\xi + i\eta)\ {}_1F_1(\xi + 1 + i\eta, 2\xi + 1; 2ikr)\right]. \end{aligned} \tag{2.12}$$

The various coefficients contained within equation (2.12) are given by

$$k = \sqrt{E^2 - 1}, \quad \eta = \frac{\zeta E}{k}, \quad \delta_\kappa = \frac{1}{2}\arg\left(\frac{-\kappa + i\eta/E}{\xi + i\eta}\right),$$
$$N = \sqrt{\frac{2k}{\pi}} e^{\pi\eta/2} \frac{|\Gamma(\xi + i\eta)|}{\Gamma(2\xi + 1)} \quad \text{and}$$
$$\Delta_\kappa = \delta_\kappa - \arg\Gamma(\xi + i\eta) - \frac{\pi\xi}{2} + (l+1)\frac{\pi}{2}, \tag{2.13}$$

where N is set, as is customary, by normalising against both the radial coordinate r and against energy according to

$$\int_0^\infty r^2 \mathrm{d}r \left|\phi_{E\kappa m_j}(\mathbf{r})\right|^2 \frac{2\sin(r\Delta E)}{r} = 1, \tag{2.14}$$

here, ΔE is a small energy interval. If one is interested in calculating the cross sections of an emitted particle with energy $E > 1$, then the partial wave representation is no longer satisfactory. In this case, a transformation is required, whereby the emitted particle is classified only by its spin projection m_s, direction of propagation θ (the angle between the z–axis and the particle's momentum $\mathbf{k}$) and its energy E [29]

$$\Phi_{Em_s}(\mathbf{r}) = 4\pi \sum_{\kappa=\pm1}^{\pm\infty} \sum_{\mu=-j}^{j} i^l e^{-i\Delta_\kappa} \left\langle \begin{array}{ccc|c} l & & \frac{1}{2} & j \\ \mu - m_s & & m_s & \mu \end{array} \right\rangle \phi_{E\kappa\mu}(\mathbf{r}) Y^*_{l,\mu-m_s}(\theta, 0). \tag{2.15}$$

2.3 Bound state wavefunctions for extended nuclei

In this section, the next stage in the derivation of an adequate analytic basis for comparing the eigenvalues and eigenfunctions generated using numerical procedures shall be clarified. Since the numerical solution to the time–independent, two–centre Dirac equation is, in its simplest approximation, equivalent to the single–centre problem for extended nuclei, it would be remiss to conduct a comparison between both the numerical and analytic methods for any other type of potential. Furthermore, for the very heavy nuclei considered in section 3, an extended potential will more accurately replicate the true eigenvalues and eigenfunctions of the systems considered.

The treatment of the Dirac equation for point–like, central potentials laid out in section 2.2 no longer suffices when the nuclear charge exceeds $Z = 137$. For $s_{1/2}$ and $p_{1/2}$ states ($|\kappa| = 1$), this limit is even lower, regular solutions to equation (2.7) for these states cannot be generated if $Z > 118$, a consequence of the fact that for these charges, both regular and irregular solutions to equation (2.7) become normalisable, resulting in an unphysical *continuum* of solutions possessing no bound states.

Therefore, in this regime, the size of the nucleus must be accounted for in the analytic theory. In this section, a short summary of how one may obtain analytic bound state wavefunctions for extended nuclei is made. In section 2.4, the numerical methods for handling extended potentials will be explored, hence it shall prove useful to compare the agreement between eigenfunctions and eigenenergies produced using either exact or numerical methods. No such analytic investigation will be provided for continuum state wavefunctions of an extended potential, two excellent reviews of continuum wavefunctions for extended nuclei do however exist in the literature [27, 30]. The numerical procedure for generating wavefunctions that follows, unambiguously discretises the entire spectrum, if the purpose of introducing analytic wavefunctions is only to compare with wavefunctions obtained via numerical methods, a back to back comparison of the continuum wavefunctions of each method is at best an undertaking of questionable validity. It is much better then to conduct a comparison for the part of the spectrum, i.e. $-1 < E < 1$, where both methods produce discretised wavefunctions.

In order to correctly account for an extended nucleus, a modification to the potential (2.3) must be made, the simplest such modification is

$$V(r, R) = -\alpha Z \left(\frac{\Theta(-r + R)}{R} + \frac{\Theta(r - R)}{r} \right), \tag{2.16}$$

where R is the nuclear radius and Θ is the heaviside function, equation (2.16) is known as the charged spherical shell potential. A thorough dissection of the solution methods of the Dirac equation for extended nuclei is, for most intents and purposes not necessary, and anyway not entirely encompassed within the main thrust of this examination, for that, one is referred to the literature [30, 31, 13]. However, in the interests of furnishing the reader with a *computationally stable* platform for generating solutions to equation (2.7) in the region $r > R$ for the potential (2.16), the salient features of these prior investigations shall be given.

Essentially, one need only realise that equation (2.7) can be reduced to a form of the Whittaker equation. If one introduces a new radial wavefunction,

comprised of both $g_\kappa(r)$ and $f_\kappa(r)$

$$h_\kappa^\pm(r) = (2kr)^{3/2}\left(g_\kappa(r) \mp \sqrt{\frac{1+E}{1-E}} f_\kappa(r)\right),$$
$$g_\kappa(r) = \frac{h_\kappa^+(r) + h_\kappa^-(r)}{2(2kr)^{3/2}}, \qquad f_\kappa(r) = \frac{h_\kappa^-(r) - h_\kappa^+(r)}{2(2kr)^{3/2}} \tag{2.17}$$

where $k = \sqrt{1-E^2}$. If again the following variables are defined

$$\zeta = \alpha Z, \quad \xi^2 = \kappa^2 - \zeta^2, \quad \eta = \frac{\xi E}{k}, \quad \eta_\pm = \eta \pm \frac{1}{2}$$
$$\Delta(\eta_\pm, \xi) = \frac{\Gamma(2\xi+1)\,\Gamma\left(\frac{1}{2} - \xi - \beta_\pm\right)}{\Gamma(-2\xi+1)\,\Gamma\left(\frac{1}{2} + \xi - \beta_\pm\right)} \quad \text{and} \quad \frac{N_+}{N_-} = -\frac{\xi - \eta}{\kappa - \eta/E}, \tag{2.18}$$

one may write a solution for $h_\kappa^\pm(r)$ in the form

$$h_\kappa^\pm(r) = N_\pm\left(M_{\eta_\pm,\xi}(2kr) - \Delta(\eta_\pm, \xi)\, M_{\eta_\pm,-\xi}(2kr)\right). \tag{2.19}$$

It is a simple task to show, using equation (2.17) and the last of equations (2.18) that $g_\kappa(r)$ and $f_\kappa(r)$ are comprised of, and share one and only one normalisation constant. The solution in the region $r < R$ can be given in terms of the Bessel functions

$$g_\kappa(r) = \begin{cases} N_i \frac{1}{\sqrt{r}} J_{\kappa+\frac{1}{2}}\left(-ir\sqrt{1-(E-V_0)^2}\right), & \kappa > 0 \\ N_i \frac{1}{\sqrt{r}} Y_{\kappa+\frac{1}{2}}\left(-ir\sqrt{1-(E-V_0)^2}\right), & \kappa < 0 \end{cases}$$
$$f_\kappa(r) = \begin{cases} N_i e^{i\pi/2} \frac{1}{\sqrt{r}} \frac{\sqrt{E+V_0-1}}{\sqrt{E+V_0+1}} J_{\kappa-\frac{1}{2}}\left(-ir\sqrt{1-(E-V_0)^2}\right), & \kappa > 0 \\ N_i e^{i\pi/2} \frac{1}{\sqrt{r}} \frac{\sqrt{E+V_0-1}}{\sqrt{E+V_0+1}} Y_{\kappa+\frac{1}{2}}\left(-ir\sqrt{1-(E-V_0)^2}\right), & \kappa < 0, \end{cases} \tag{2.20}$$

where $V_0 = -\alpha Z/R$. It only remains to determine the normalising coefficients, N_i, N_- or N_+ and the energy E. With the introduction of the superscripts $>$ for the region $r > R$ and $<$ for the region $r < R$, the equation for determining bound state energies is

$$\frac{g_\kappa^>(R)}{f_\kappa^>(R)} = \frac{g_\kappa^<(R)}{f_\kappa^<(R)}. \tag{2.21}$$

Once a particular energy is determined, one may then make use of the typical boundary matching conditions to determine N_- or N_+ and N_i

$$\begin{aligned} g_\kappa^> (R) &= g_\kappa^< (R) \\ \frac{\mathrm{d}g_\kappa^> (R)}{\mathrm{d}r} &= \frac{\mathrm{d}g_\kappa^< (R)}{\mathrm{d}r}. \end{aligned} \tag{2.22}$$

The results of equations (2.22) and (2.21) thus completely determine the form of bound state wavefunctions for the hollow shell potential.

2.4 Numerical methods

Having elaborated on the *analytic* techniques at one's disposal for solving the Dirac equation for a central potential, attention is now brought to the methods that exist for treating this problem *numerically*. The starting point for this part of the discussion is once more the set of coupled differential equations for $G_{\epsilon\kappa}(r)$ and $F_{\epsilon\kappa}(r)$

$$\begin{aligned} \left(\frac{\mathrm{d}F_{\epsilon\kappa}(r)}{\mathrm{d}r} - \frac{\kappa}{r} F_{\epsilon\kappa}(r) \right) &= -\left(\epsilon - V(r) - 1\right) G_{\epsilon\kappa}(r) \\ \left(\frac{\mathrm{d}G_{\epsilon\kappa}(r)}{\mathrm{d}r} + \frac{\kappa}{r} G_{\epsilon\kappa}(r) \right) &= \left(\epsilon - V(r) + 1\right) F_{\epsilon\kappa}(r). \end{aligned} \tag{2.23}$$

The numerical approach to solving (2.23) proposed by Johnson [32], with the *dual–kinetically–balanced* (DKB) B–spline basis of Shabaev [33], is reproduced here. Usage of the DKB basis has proven popular in recent years [34, 35, 36] given its ability to eliminate so called "spurious states," something which will be briefly explained in section 2.4.1 below. Before beginning, a brief overview of the essentials of the B–spline basis as used in the following is necessary.

2.4.1 The B–spline basis

The manner in which B–splines are used as the basis for solving the time–independent Dirac equation for a central potential (and later on, a two–centre potential) is essentially no different to other traditional numerical solution methods for differential equations; a coefficient expansion of $G_{\epsilon\kappa}(r)$ and $F_{\epsilon\kappa}(r)$ comprised of B–spline polynomials, defined piecewise inside a box spanning some finite range $(r = 0..r_{max})$, is carried out over the complete set of splines. The reason B–splines have been chosen over other competing bases, e.g. a basis of

Gaussians or Legendre polynomials, is due to their guaranteed continuity over the entire space, their ability to replicate continuum eigenfunctions better than other competing bases, the high accuracy of integrals involving B–splines and their relatively fast computational evaluation.

The set of polynomial splines used here, as proposed in [37], is given by the following recursion equation

$$B_i^1(r) = \begin{cases} 1, & t_i \leq r < t_{i+1} \\ 0, & \text{elsewhere} \end{cases}, \quad \text{and}$$
$$B_i^k(r) = \frac{r - t_i}{t_{i+k-1} - t_i} B_i^{k-1}(r) + \frac{t_{i+k} - r}{t_{i+k} - t_{i+1}} B_{i+1}^{k-1}(r). \tag{2.24}$$

The spline $B_i^n(r)$ only has non–zero values in the range $t_i \to t_{i+n}$. The radial coordinate is divided onto a grid, spanning the range of $r = 0$ to $r = r_{\text{max}}$, consisting of N_m intervals. r_{max} is colloquially known as the box size. N_m+n+2 spline nodes are fixed at the start/end points of these intervals. The first and last n nodes are fixed at $r = 0$ and $r = r_{max}$ respectively, in other words, the position of these nodes t_i is such that

$$\text{for} \quad 1 \leq i \leq n \to t_i = 0 \quad \text{and} \quad N_m+3 \leq i \leq N_m+n+2 \to t_i = r_{\text{max}}. \tag{2.25}$$

The remaining $N_m - n + 2$ nodes are fixed sequentially at the end of each interval, that is, node $n + 1$ is fixed at the interface between interval 1 and 2, node $n + 2$ is fixed at the interface between intervals 2 and 3 and so forth.

For instance, if one is using splines of order 3, and a grid containing 10 equally spaced intervals extending from $x = 0$ to $x = x_{max} = 10$, then the position of the nodes in this case would be $t_1 = t_2 = t_3 = 0$, $t_4 = 1$, $t_5 = 2$ $\ldots t_{11} = 8$, $t_{12} = 9$, $t_{13} = t_{14} = t_{15} = 10$. An example of this set of splines and its distribution is shown in figure 2.1.

One particular property of equation (2.24) is that the first and last splines on the grid are both equal to 1 at $r = 0$ and $r = r_{max}$ respectively. For the purposes of normalisation, it is desirable to ensure that in the limit $r \to 0$ or $r \to \infty$ that $G_{\epsilon\kappa}(r) = F_{\epsilon\kappa}(r) = 0$. To accomplish this, the coefficient expansion for $G_{\epsilon\kappa}(r)$ and $F_{\epsilon\kappa}(r)$ is made whereby the *first* and *last* B–splines are omitted from the basis. In essence, the purpose of the first and last splines is simply to *define* their subsequent and previous splines respectively.

In the following passages, the *dual–kinetically–balanced* B–spline basis is employed in finding solutions for $G_{\epsilon\kappa}(r)$ and $F_{\epsilon\kappa}(r)$ for a spherical shell potential (2.16), this can be explicitly written as

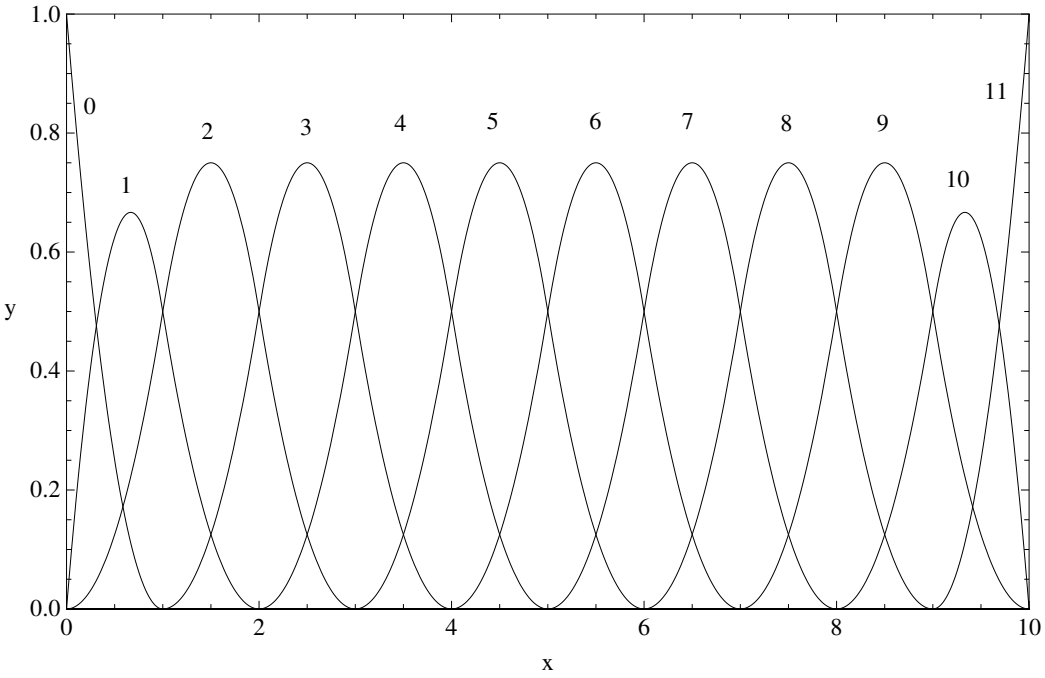

Figure 2.1: The set of twelve, third order B–splines $B_i^3(x)$ forming the basis over an equally spaced grid spanning $x = 0..10$.

$$G_{\epsilon\kappa}(r) = \sum_{i=1}^{N_m} \left(v_{\epsilon i\kappa} + v_{\epsilon\iota\kappa} \frac{1}{2} \left(\frac{\mathrm{d}}{\mathrm{d}r} - \frac{\kappa}{r} \right) \delta_{i,\iota-N_m} \right) B_{i+1}^n(r) = \sum_{i=1}^{N_m} \tilde{G}_{\epsilon\kappa}^i(r)$$
$$F_{\epsilon\kappa}(r) = \sum_{i=1}^{N_m} \left(v_{\epsilon\iota\kappa} \delta_{i,\iota-N_m} + v_{\epsilon i\kappa} \frac{1}{2} \left(\frac{\mathrm{d}}{\mathrm{d}r} + \frac{\kappa}{r} \right) \right) B_{i+1}^n(r) = \sum_{i=1}^{N_m} \tilde{F}_{\epsilon\kappa}^i(r), \tag{2.26}$$

subject to the customary normalisation condition

$$\int_0^{r_{max}} \mathrm{d}r \left(G_{\epsilon\kappa}(r)^2 + F_{\epsilon\kappa}(r)^2 \right) = 1. \tag{2.27}$$

The $v_{\epsilon i\kappa}$ in equation (2.26) are the aforementioned expansion coefficients. Furthermore, the spline nodes t_i are distributed exponentially with the density of nodes decreasing as r increases. One important consequence of equation (2.27), in contrast to the analytic procedure, is that this condition applies to all energies, not merely those where $-1 < E < 1$, this implies that numeric

solutions to (2.23) have discrete energies for the *entire* spectrum. Hereafter, it is assumed that the order of the B-splines is given (In all calculations which follow, splines of order eight have been used), thus the superscript designating spline order will be dropped.

A curious property of the *non–balanced–basis*, as implemented in [32], is its propensity to produce so called "spurious" states[1]. The reasons for this are well explained elsewhere [33], but essentially, usage of this basis does not impose one important condition that is present in the analytic theory, namely that $-n \leq \kappa < n$ (here, n is defined in equation (2.8)). Thus, a non–balanced basis unambiguously permits the presence of non–physical states such as 1p and 2d states.

2.4.2 Applying the B–spline basis to the spherical shell potential

With the classification of the basis in terms of piecewise B–spline polynomials complete, the focus can now shift to the linear algebra methods required for the determination of the expansion coefficients $v_{\epsilon i\kappa}$ of the functions $G_{\epsilon\kappa}(r)$ and $F_{\epsilon\kappa}(r)$ and their corresponding eigenenergies. Introducing the notation

$$|\varphi_{\epsilon\kappa}\rangle = \begin{pmatrix} G_{\epsilon\kappa}(r) \\ F_{\epsilon\kappa}(r) \end{pmatrix} = \sum_i \begin{pmatrix} 1 & D \\ D^\dagger & 1 \end{pmatrix} \begin{pmatrix} v_{\epsilon i\kappa} \\ v_{\epsilon\iota\kappa}\delta_{i,\iota-N_m} \end{pmatrix} B_{i+1}(r)$$

where

$$D = \frac{1}{2}\left(\frac{\mathrm{d}}{\mathrm{d}r} - \frac{\kappa}{r}\right) \quad \text{and} \quad D^\dagger = \frac{1}{2}\left(\frac{\mathrm{d}}{\mathrm{d}r} + \frac{\kappa}{r}\right), \tag{2.28}$$

and defining the action for a particular κ and fixed (but undetermined) energy, i.e. $|\varphi_{\epsilon\kappa}\rangle \equiv |\varphi\rangle$

$$S = \langle\varphi|\,\hat{\mathbf{H}}\,|\varphi\rangle - \epsilon\,\langle\varphi|\varphi\rangle\,, \tag{2.29}$$

one may, using the principle of least action $\delta S = 0$, derive an eigenvalue problem for $v_{\epsilon i\kappa}$. In pursuance of this, the variance of the action is minimised with respect to the coefficients $v_{\epsilon i\kappa}$ according to

$$\frac{\mathrm{d}S}{\mathrm{d}v_{\epsilon i\kappa}} = 0, \tag{2.30}$$

[1] In [38] it is claimed that usage of a non–balanced basis with splines of different order for the large and small components of the radial solution can also eliminate spurious states.

the equation for the undetermined coefficients $v_{\epsilon i\kappa}$ of a particular energy ϵ and κ is thus

$$\hat{\mathcal{H}}\vec{v} = \epsilon\hat{\mathcal{N}}\vec{v}. \tag{2.31}$$

While rather lengthy in their full representation, the elements of matrix $\hat{\mathcal{H}}$, under the restriction $1 \leq i \bigwedge j \leq N_m$, are written as

$$\begin{aligned}
\mathcal{H}_{ij} &= U_{ij} + \frac{3}{4}D_{ij} + \frac{3}{4}\kappa\left(\kappa+1\right)\mathcal{U}_{ij} \\
&\quad + \frac{1}{2}\left(V_{ij}^{1} + V_{ij}^{2} + \kappa^{2}V_{ij}^{3} + \kappa V_{ij}^{4}\right) \\
\mathcal{H}_{i+N_m j+N_m} &= -U_{ij} - \frac{3}{4}D_{ij} - \frac{3}{4}\kappa\left(\kappa-1\right)\mathcal{U}_{ij} \\
&\quad + \frac{1}{2}\left(V_{ij}^{1} + V_{ij}^{2} + \kappa^{2}V_{ij}^{3} - \kappa V_{ij}^{4}\right) \\
\mathcal{H}_{ij+N_m} &= \frac{1}{2}V_{ij}^{5} + \frac{1}{8}\left(\mathcal{D}_{ij}^{1} - \mathcal{D}_{ji}^{1}\right) + \frac{1}{8}\left(\mathcal{D}_{ij}^{2} + \mathcal{D}_{ji}^{3}\right) \\
\mathcal{H}_{i+N_m j} &= \mathcal{H}_{j+N_m i},
\end{aligned} \tag{2.32}$$

where the sub–matrices within equation (2.32) are, with the assistance of the coefficients $\mathfrak{i} = i + 1$ and $\mathfrak{j} = j + 1$ (which are used to ensure the exclusion of the first spline on the B–spline basis), given by

$$
\begin{aligned}
U_{ij} &= \int_0^\infty \mathrm{d}r \left(B_{\mathrm{i}}\left(r\right) B_{\mathrm{j}}\left(r\right)\right), \quad D_{ij} = \int_0^\infty \mathrm{d}r \left(\frac{\mathrm{d}B_{\mathrm{i}}\left(r\right)}{\mathrm{d}r}\right)\left(\frac{\mathrm{d}B_{\mathrm{j}}\left(r\right)}{\mathrm{d}r}\right), \\
\mathcal{U}_{ij} &= \int_0^\infty \frac{\mathrm{d}r}{r^2} \left(B_{\mathrm{i}}\left(r\right) B_{\mathrm{j}}\left(r\right)\right), \quad V^1_{ij} = \int_0^\infty \mathrm{d}r \left(B_{\mathrm{i}}\left(r\right) V\left(r\right) B_{\mathrm{j}}\left(r\right)\right), \\
V^2_{ij} &= \frac{1}{4}\int_0^\infty \mathrm{d}r \left(\frac{\mathrm{d}B_{\mathrm{i}}\left(r\right)}{\mathrm{d}r}\right) V\left(r\right)\left(\frac{\mathrm{d}B_{\mathrm{j}}\left(r\right)}{\mathrm{d}r}\right), \\
V^3_{ij} &= \frac{1}{4}\int_0^\infty \frac{\mathrm{d}r}{r^2} \left(B_{\mathrm{i}}\left(r\right) V\left(r\right) B_{\mathrm{j}}\left(r\right)\right), \\
V^4_{ij} &= \frac{1}{4}\int_0^\infty \frac{\mathrm{d}r}{r} \left(B_{\mathrm{i}}\left(r\right)\frac{\mathrm{d}B_{\mathrm{j}}\left(r\right)}{\mathrm{d}r} + B_{\mathrm{j}}\left(r\right)\frac{\mathrm{d}B_{\mathrm{i}}\left(r\right)}{\mathrm{d}r}\right) V\left(r\right), \\
V^5_{ij} &= \frac{1}{2}\int_0^\infty \mathrm{d}r \left(B_{\mathrm{i}}\left(r\right)\frac{\mathrm{d}B_{\mathrm{j}}\left(r\right)}{\mathrm{d}r} + B_{\mathrm{j}}\left(r\right)\frac{\mathrm{d}B_{\mathrm{i}}\left(r\right)}{\mathrm{d}r}\right) V\left(r\right), \\
\mathcal{D}^1_{ij} &= \int_0^\infty \mathrm{d}r \left(\frac{\mathrm{d}B_{\mathrm{i}}\left(r\right)}{\mathrm{d}r}\right)\left(\frac{\mathrm{d}^2B_{\mathrm{j}}\left(r\right)}{\mathrm{d}r^2}\right), \\
\mathcal{D}^2_{ij} &= \int_0^\infty \mathrm{d}r \left(B_{\mathrm{i}}\left(r\right)\frac{\mathrm{d}^2B_{\mathrm{j}}\left(r\right)}{\mathrm{d}r^2}\right)\frac{\kappa}{r} - \left(B_{\mathrm{j}}\left(r\right)\frac{\mathrm{d}B_{\mathrm{i}}\left(r\right)}{\mathrm{d}r}\right)\frac{\kappa\left(\kappa-1\right)}{r^2} \\
&\quad - \left(B_{\mathrm{i}}\left(r\right) B_{\mathrm{j}}\left(r\right)\right)\frac{\kappa^2\left(\kappa-1\right)}{r^3} \quad \text{and} \\
\mathcal{D}^3_{ij} &= \int_0^\infty \mathrm{d}r \left(B_{\mathrm{i}}\left(r\right)\frac{\mathrm{d}^2B_{\mathrm{j}}\left(r\right)}{\mathrm{d}r^2}\right)\frac{\kappa}{r} + \left(B_{\mathrm{j}}\left(r\right)\frac{\mathrm{d}B_{\mathrm{i}}\left(r\right)}{\mathrm{d}r}\right)\frac{\kappa\left(\kappa+1\right)}{r^2} \\
&\quad - \left(B_{\mathrm{i}}\left(r\right) B_{\mathrm{j}}\left(r\right)\right)\frac{\kappa^2\left(\kappa+1\right)}{r^3}.
\end{aligned} \tag{2.33}
$$

Gauss–Legendre integration is employed here for the evaluation of the integrals contained in equation (2.33). The normalisation matrix $\hat{\mathcal{N}}$ of equation (2.31) can be decomposed into the submatrices

$$
\begin{aligned}
\mathcal{N}_{ij} &= U_{ij} + \frac{1}{4}D_{ij} + \frac{\kappa\left(\kappa+1\right)}{4}\mathcal{U}_{ij} \\
\mathcal{N}_{i+N_m j+N_m} &= U_{ij} + \frac{1}{4}D_{ij} + \frac{\kappa\left(\kappa-1\right)}{4}\mathcal{U}_{ij} \\
\mathcal{N}_{i+N_m j} &= \mathcal{N}_{ij+N_m} = 0.
\end{aligned} \tag{2.34}
$$

The concluding step is to agglomerate matrices $\hat{\mathcal{N}}$ and $\hat{\mathcal{H}}$, and generate the $2N_m$ eigenvectors $v_{\epsilon i}$ for each of the $2N_m$ eigenvalues ϵ of the matrix $\hat{\mathcal{A}}$ via

$$
\hat{\mathcal{A}}\vec{v} = \left(\hat{\mathcal{H}} - \epsilon\hat{\mathcal{N}}\right)\vec{v} = 0. \tag{2.35}
$$

Obtaining $\vec{v}$ completes the process for generating numerical solutions to the stationary single–centre Dirac equation for an extended nuclear potential.

Chapter 3

Numerical solution to the time–independent, two–centre Dirac equation

In a purely two–centre regime, the analytical methods described in section 2 are no longer applicable. Only with the assistance of approximate numerical methods can eigenfunctions and eigenvalues of the static two–centre Dirac equation be found.

The approach used here for treating the two–centre potential involves decomposing this potential into a multipole sum, this is done to preserve the use of spherical coordinates. Fortunately, in the zeroth order approximation, this expansion of the potential is identical to the charged spherical shell potential, and as such, a comparison of eigenvalues and eigenfunctions will be conducted for this potential between numerical and analytic methods.

As mentioned in the introduction, the hand of the theoretician is not necessarily forced into working within spherical coordinates, pure two–centre coordinate systems, such as prolate spherical or Cassini coordinates (cf. [24, 23]) can be used in which the potential is automatically accounted for to all orders. Usage of a pure two–centre coordinate system can be of particular advantage in handling the Dirac equation *for homonuclear charges*. In this case, Cassini coordinates correspond very closely to the equipotential lines and the electric field gradient, furthermore, the lemniscate intersects at the barycentre.

However, should the system be heteronuclear, while the foci remain fixed at the nuclei, the coordinates no longer correspond to the equipotential lines, and the lemniscate is shifted from the barycentre[1]. This may prove disadvantageous

[1] a quasi-Cassini coordinate system which could fulfil these conditions, i.e. foci at the nuclei *and* a lemniscate that intersects at the barycentre, a "bowling pin" type lemniscate for

when one attempts to handle dynamic problems. Two benefits of persisting with spherical coordinates are firstly its flexibility in setting the coordinate centre at the most favourable position and secondly the large degree to which analytic simplifications can be made, these will be explored in the coming passages.

First of all however, a quick overview of the Hamiltonian of the two–centre system and how the system itself is spatially configured is provided to grant the reader a clear picture of the differences between the two– and single–centre scenarios. The time–independent Dirac equation for two, point–like coulomb centres is given by

$$\begin{aligned}
\hat{\mathbf{H}}_{TC}\phi(\mathbf{r}) &= E\phi(\mathbf{r}), \quad \text{where} \\
\hat{\mathbf{H}}_{TC} &= \boldsymbol{\alpha}\cdot\mathbf{p} - \frac{\alpha Z_1}{|\mathbf{r}-\mathbf{R}_1|} - \frac{\alpha Z_2}{|\mathbf{r}-\mathbf{R}_2|} + \boldsymbol{\beta}, \quad \text{and} \\
-\frac{\alpha Z_1}{|\mathbf{r}-\mathbf{R}_1|} - \frac{\alpha Z_2}{|\mathbf{r}-\mathbf{R}_2|} &= \sum_{L=0}^{2K} V_{TC}^{L}(\mathbf{r},\mathbf{R}) \\
V_{TC}^{L}(\mathbf{r},\mathbf{R}) &= -\alpha\left[P_L(\cos\vartheta)\left(\frac{Z_1\rho_{1<}^{L}(r,R_1)}{\rho_{1>}^{L+1}(r,R_1)}\right.\right. \\
&\quad \left.\left. + (-1)^L\frac{Z_2\rho_{2<}^{L}(r,R_2)}{\rho_{2>}^{L+1}(r,R_2)}\right)\right],
\end{aligned} \tag{3.1}$$

here, $\rho_{i<}(r,R_i) = \min(r,R_i)$ and $\rho_{i>}(r,R_i) = \max(r,R_i)$ for $i = 1,2$, $P_L(\vartheta)$ are the Legendre polynomials, and ϑ is the angle formed between $\hat{\mathbf{r}}$ and $\hat{\mathbf{R}}$, as can be seen in figure 3.1. The choice of the coordinate centre for the stationary problem is, strictly speaking, (almost) entirely irrelevant. However, since its importance will become clear in section 6.1 where the recoiling motion of two moving nuclei must be accounted for, it is prudent to set the coordinate centre at the barycentre.

$$R_1 = \frac{M_2}{M_1+M_2}R \qquad R_2 = \frac{M_1}{M_1+M_2}R, \tag{3.2}$$

where R is the internuclear distance, and M_i is the mass of the i*th* nucleus. Figure 3.1 pictorially reflects the arrangement of the spherical coordinates for a homonuclear system, i.e. $Z_1 = Z_2\,, M_1 = M_2$. Also illustrated in figure 3.1 is the exponential spline node distribution (concentric circles), and the maximum size of the box r_{max}.

heteronuclear systems, would be optimal

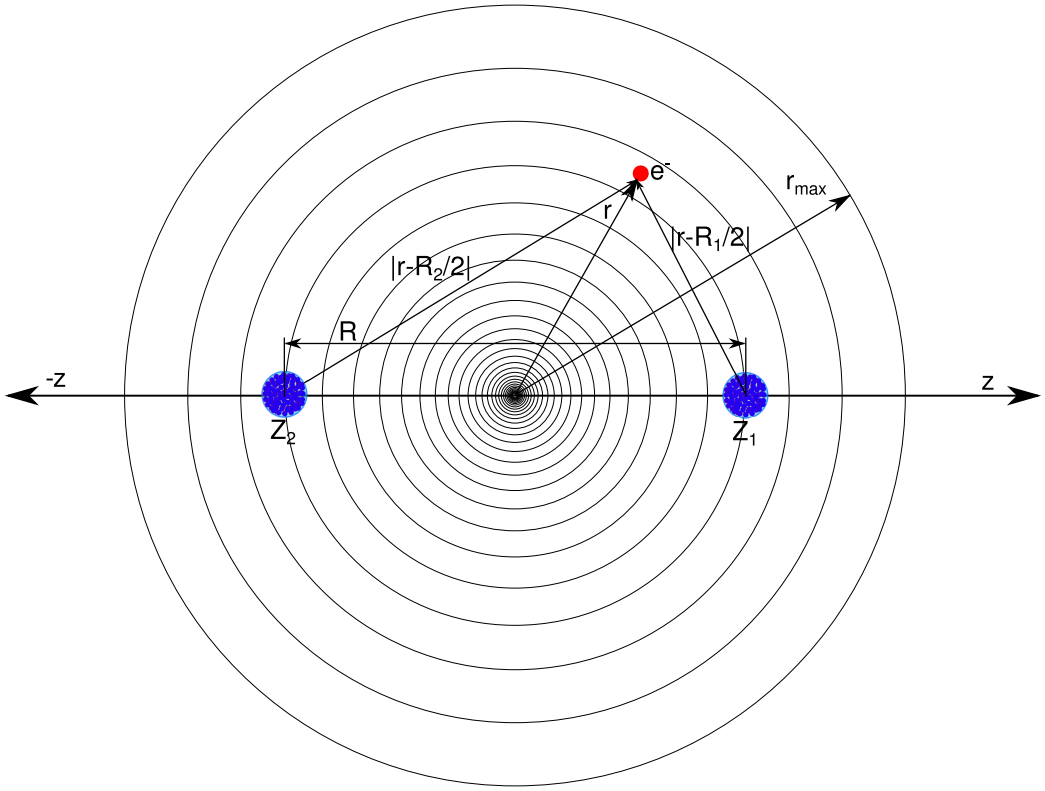

Figure 3.1: A homonuclear two–centre system in spherical coordinates. The concentric rings represent the B–spline node boundaries, r_{max} shows the extent of the box.

3.1 The monopole approximation

The first brick in the pathway towards a sophisticated theory for the stationary two–centre Dirac equation, for which a seamless computational implementation is guaranteed, begins with the monopole approximation to the two centre potential. One of the temptations the theoretician is faced with when choosing the means with which to handle the two–centre problem in spherical coordinates, is utilising the full expansion of the potential (3.1) to *directly* obtain two–centre wavefunctions. This approach, while valid, has a considerable tendency to increase the processing time required for the production of basis wavefunctions. The technique put forward here ensures a significant computational acceleration in the creation of a two–centre basis.

As a first step in the monopole approximation, one seeks the eigenvalues and eigenfunctions of the zeroth–order Hamiltonian of equation (3.1)

$$\hat{\mathbf{H}}^{0}_{TC} = \boldsymbol{\alpha} \cdot \mathbf{p} + V^{0}_{TC}\left(\mathbf{r}, \mathbf{R}\right) + \boldsymbol{\beta}, \tag{3.3}$$

which, when simplifying the potential V^{0}_{TC}, takes precisely the same form as the extended potential presented in equation (2.16). For a heteronuclear two–centre problem, the monopole approximation of the potential creates a type of double hollow shell potential, for a homonuclear two–centre potential of two charges Z, the monopole approximation is exactly the same as seeking a solution to the hollow shell potential for a single nucleus of charge $2Z$ and charge radius $R/2$.

The creation of a monopole basis can then be conducted either via the analytic procedure outlined in section 2.3 or the numerical procedure in section 2.4; one simply substitutes $V^{0}_{TC}\left(\mathbf{r}, \mathbf{R}\right)$ into equations (2.16) and (2.23) respectively. Since the ultimate goal is to utilise numerical methods in finding a two–centre basis for higher terms in the multipole expansion, a comparison between numerical and analytic techniques in generating eigenvalues and eigenfunctions would be of considerable use.

3.2 Comparison between numerical and exact methods for the hollow shell potential

As alluded to, before one can be certain of the merits and validity of any approximate method, a comparison with established techniques, where possible, is highly desirable. The procedure outlined in section 2.3 for obtaining analytic solutions to the Dirac equation for the hollow shell potential model should serve

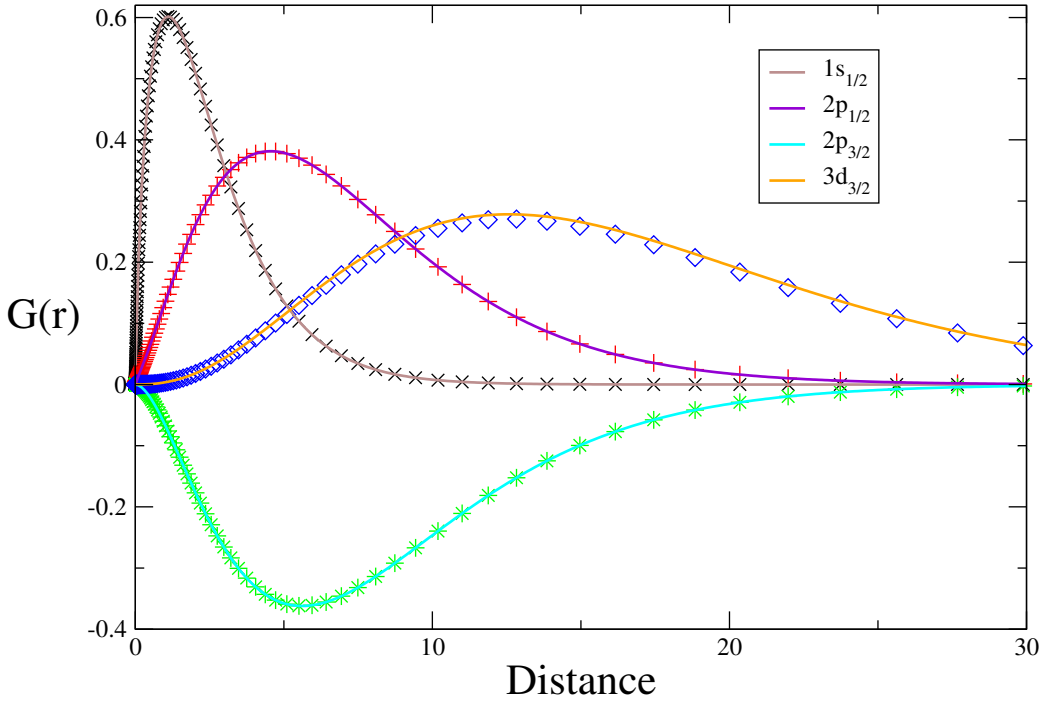

Figure 3.2: The large component of a Hydrogen–like Uranium ion, where the nuclear size is accounted for using the charged spherical shell model. The numerical techniques outlined in section 2.4 are represented here by the points $\times$ $+$ $\star$ and $\diamond$. Smooth curves are analytic wavefunctions obtained with the technique outlined in section 2.3. As is evident, very little difference between numerical methods, and analytic methods actually exists. The horizontal axis is the distance from the coordinate centre in natural units.

as an equitable standard, against which any numerical method would need to adequately compare, before attaining general acceptance.

In order to accomplish this, a small but relevant range of tests have been selected. The analytic large $G_{n\kappa}(r) = rg_{n\kappa}(r)$ and small $F_{n\kappa}(r) = rf_{n\kappa}(r)$ wavefunction components of equations (2.17)-(2.20) will be compared against their numerical counterparts as defined in equation (2.26) for a U^{91+} ion with a spherically charged shell of radius 7.4366 fm. Furthermore, a comparison between eigenvalues obtained via both methods, not only for the aforementioned U^{91+} ion, but also for a Pb^{81+}–Pb^{82+} quasi–molecule, shall be given. For the Lead quasi–molecule, the nuclei are separated by a distance of 1 N.U. ~ 386.16 fm. A Pb^{81+}–Pb^{82+} quasi–molecule has been chosen given its candidacy for eliciting ground state diving, should the two centres breach the critical distance R_c [16].

The eigenfunctions $G_{n\kappa}(r)$ and $F_{n\kappa}(r)$, of both the numerical and analytic

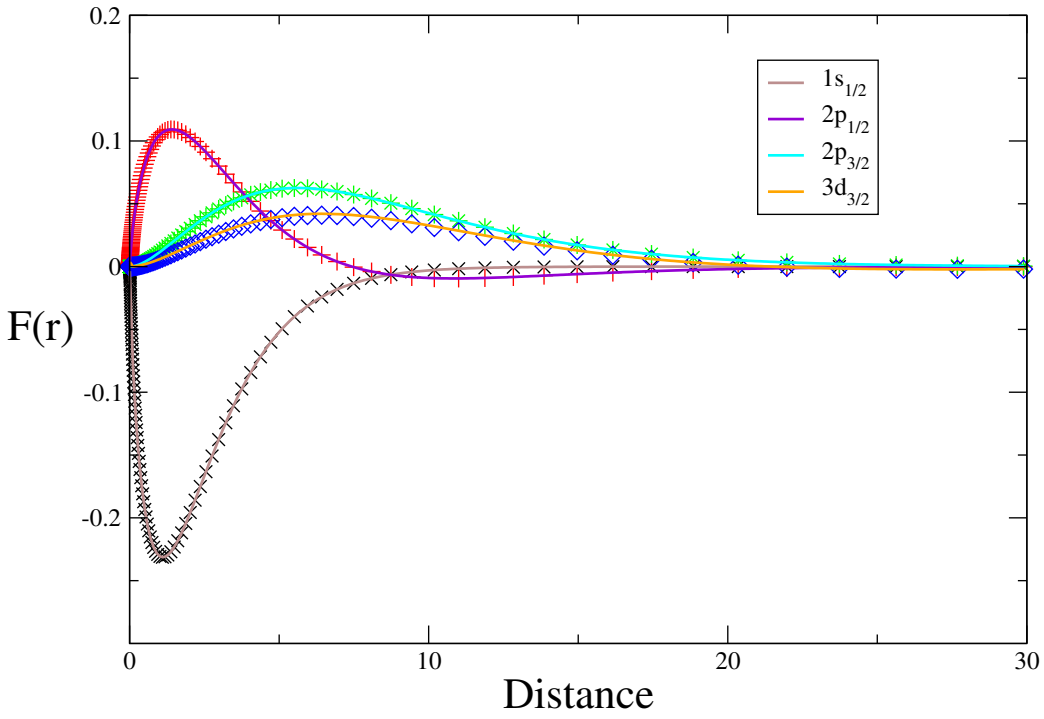

Figure 3.3: The small component of a Hydrogen–like Uranium ion, where the nuclear size is accounted for using the charged spherical shell model. Colours and curves are as per those shown in figure 3.2. The horizontal axis is the distance from the coordinate centre in natural units.

methods, for the extended U^{91+} ion are displayed in figures 3.2 and 3.3 respectively.

The eigenvalues of the extended Uranium nucleus are displayed in table 3.1, the eigenvalues of the Lead–Lead quasi–molecule can be seen in table 3.2. The results displayed in these tables were generated using basis functions on a grid with 200 splines, within a box extending to 10^5fm.

It is instantly inferable from both the tables and figures presented here, that numerical methods do indeed reproduce, to a very high precision, the eigenfunctions and eigenvalues attainable using exact methods.

3.3 Extending the monopole basis for higher multipoles

Although the monopole approximation to the two–centre potential can be a good tool for generating a Dirac spectrum for small internuclear distances, it is by no

Table 3.1: Comparison between eigenvalues generated using numerical and exact methods for U^{91+} for a nuclear radius of 7.4366fm

State	Numerical	Exact	% Difference
$1s_{1/2}$	0.7416885393	0.7416885418	3.4×10^{-9}
	0.7416885625 [31]		3.1×10^{-8}
$2s_{1/2}$	0.9331470857	0.9331470864	7.5×10^{-10}
$3s_{1/2}$	0.9713241318	0.9713241321	3.1×10^{-10}
$2p_{1/2}$	0.9330543217	0.9330543223	6.4×10^{-10}
$3p_{1/2}$	0.9712969007	0.9712969010	3.1×10^{-10}
$4p_{1/2}$	0.9842790113	0.9842790114	1.0×10^{-10}
$2p_{3/2}$	0.9419767163	0.9419767147	1.7×10^{-9}
$3p_{3/2}$	0.9739581129	0.9739581044	8.7×10^{-9}
$4p_{3/2}$	0.9853874153	0.9853874040	1.2×10^{-8}
$3d_{3/2}$	0.9739581128	0.9739581052	7.8×10^{-9}
$4d_{3/2}$	0.9853874152	0.9853874015	1.4×10^{-8}
$5d_{3/2}$	0.9906839624	0.9906839587	3.7×10^{-9}

Table 3.2: Comparison between eigenvalues generated using numerical and exact methods for Pb^{81+}–Pb^{82+} at an internuclear distance of 1 N.U.

State	Numerical	Exact	Difference
$1s_{1/2}$	0.3400200012	0.3400199866	4.3×10^{-8}
$2s_{1/2}$	0.7926716429	0.7926716404	3.2×10^{-9}
$3s_{1/2}$	0.9072970961	0.9072970957	4.4×10^{-10}
$2p_{1/2}$	0.7155414755	0.7155414818	8.8×10^{-9}
$3p_{1/2}$	0.8869937463	0.8869937483	2.3×10^{-9}
$4p_{1/2}$	0.9407301544	0.9407301553	9.6×10^{-10}
$2p_{3/2}$	0.8024865578	0.8024865592	1.7×10^{-9}
$3p_{3/2}$	0.9091668165	0.9091668172	7.7×10^{-10}
$4p_{3/2}$	0.9493080615	0.9493080619	4.2×10^{-10}
$3d_{3/2}$	0.9085890973	0.9085890982	9.9×10^{-10}
$4d_{3/2}$	0.9490365421	0.9490365426	5.3×10^{-10}
$5d_{3/2}$	0.9678360989	0.9678360992	3.1×10^{-10}

means satisfactory once this distance exceeds $\sim 1/\alpha Z$. Beyond these distances, an electron is very unlikely to be preferentially bound to one or the other nucleus. It is for this reason that one must be able to solve the Dirac equation presented in (3.1) for higher multipoles as the internuclear distance increases.

As shall be demonstrated, one need not discard wavefunctions produced via the monopole approximation. These monopole solutions can in fact serve as the basis for solutions of higher orders in the potential expansion. It is important to emphasise at this juncture, that the methods explained from here up to the end of this chapter form half of the two most significant accomplishments of this thesis[2], and represent, to the best of the author's knowledge, an entirely new set of linear algebra procedures with which one may solve the time–independent two–centre Dirac equation.

Recapitulating then, the problem is one of finding eigenfunctions $\Phi_{n\mu}(\mathbf{r})$ of the full, two–centre Dirac Hamiltonian as described in equation (3.1)

$$\hat{\mathbf{H}}_{TC}\Phi_{n\mu}(\mathbf{r}) = E_n\Phi_{n\mu}(\mathbf{r}). \tag{3.4}$$

One proposes that these complete eigenfunctions are made up of monopole eigenfunctions $\varphi^i_{n\kappa\mu}(\mathbf{r})$ of the kind found in section 2.4 according to

$$\begin{aligned}\Phi_{n\mu}(\mathbf{r}) &= \sum_{i,\kappa=-K}^{K} \nu^i_{n\kappa}\varphi^i_{n\kappa\mu}(\mathbf{r}) = \sum_{i,\kappa=-K}^{K} \nu^i_{n\kappa}\frac{1}{r}\begin{pmatrix} \tilde{G}^i_{n\kappa}(r)\,\chi_{\kappa\mu}(\theta\phi) \\ i\tilde{F}^i_{n\kappa}(r)\,\chi_{-\kappa\mu}(\theta\phi) \end{pmatrix} \\ &= \sum_{\kappa=-K}^{K}\begin{pmatrix} \bar{G}_{n\kappa}(r)\,\chi_{\kappa\mu}(\theta\phi) \\ i\bar{F}_{n\kappa}(r)\,\chi_{-\kappa\mu}(\theta\phi) \end{pmatrix},\end{aligned} \tag{3.5}$$

where the sum over splines i is written here explicitly. Once again, the action minimisation principle (2.30) can be employed, this time in finding solutions for $\nu_{n\kappa}$

$$S = \left\langle \Phi \left| \hat{\mathbf{H}}_{TC} - E \right| \Phi \right\rangle, \quad \frac{\mathrm{d}S}{\mathrm{d}\nu_{n\kappa}} = 0. \tag{3.6}$$

In the same manner as for equation (2.31), this leads again to a matrix equation for the undetermined coefficients $\vec{\nu}$

[2]The other being the utilisation of this two–centre basis as part of the solution to the time–dependent Dirac equation, details of which are in chapter 4.

$$\hat{\mathcal{H}}\vec{\nu} = E\vec{\nu}, \quad \text{where}$$
$$\mathcal{H}_{i,j} = \epsilon_j \delta_{i,j} + \left\langle \varphi_i \left| \sum_{L=1}^{2K} V_{TC}^{L}\left(\mathbf{r}, \mathbf{R}\right) \right| \varphi_j \right\rangle, \tag{3.7}$$

the ϵ_i are the existing monopole eigenvalues. In this notation, ϵ_1 would be the lowest energy monopole eigenvalue for $\kappa = -K$, and $\epsilon_{4\times K\times N_m}$ would be the highest energy monopole eigenvalue for $\kappa = K$. In other words, a monopole state, in Dirac notation $|\varphi_{n\kappa\mu}\rangle$ corresponds to a single state $|\varphi_i\rangle$ in the matrix (3.7).

Hence the eigenvalues of $\hat{\mathcal{H}}$ are the new multipole eigenvalues, and the eigenvectors of $\hat{\mathcal{H}}$ are the undetermined coefficients $\nu_{n\kappa}$. Only eigenvectors, whose corresponding eigenvalues fall within a predefined range are selected in the final multipole basis. The derivation of a basis of monopole wavefunctions *as a first step* and their usage in calculating the matrix elements of $\mathcal{H}$ in equation (3.7) *as a second step* is what differentiates the developed method from other methods cf. [15, 39]. Where other techniques employ a "brute force" solution to the two centre problem, i.e. the full two–centre potential is solved in one step, the method proposed here has a significant advantage in terms of computational speed by employment of this two step procedure. The solutions for the monopole approximation to the two–centre potential can be found very quickly, as a result of this, the size of the matrix $\mathcal{H}$ is much smaller than that which would otherwise be derived, and is hence easier to diagonalise.

As an example of the eigenfunctions one may derive as a result of equation (3.5), figure 3.4 displays the large and small components of the wavefunction in equation (3.5). The $1\sigma_g$ state of a U^{92+}–U^{91+} quasi–molecule for different internuclear distances, where 8 different partial waves were used in equation (3.5), i.e. $K = 4$, is displayed. It is quite evident just how amplified the magnitude of the small component (red lines) becomes as the electric field intensifies, clear evidence of the necessity of using relativistic wavefunctions in the eigenbasis.

One useful simplification exists for equation (3.7) if the two–centre potential happens to correspond to a homonuclear system. In this case, only terms of $V_{TC}^{L}\left(\mathbf{r}, \mathbf{R}\right)$ for even L are non–zero, and the spectrum for *gerade* ($\kappa = -1, 2, -3, 4...$) and *ungerade* ($\kappa = 1, -2, 3, -4...$) states may be evaluated separately. From here onwards, the theory will focus on methods available for handling the *time–dependent* Dirac equation.

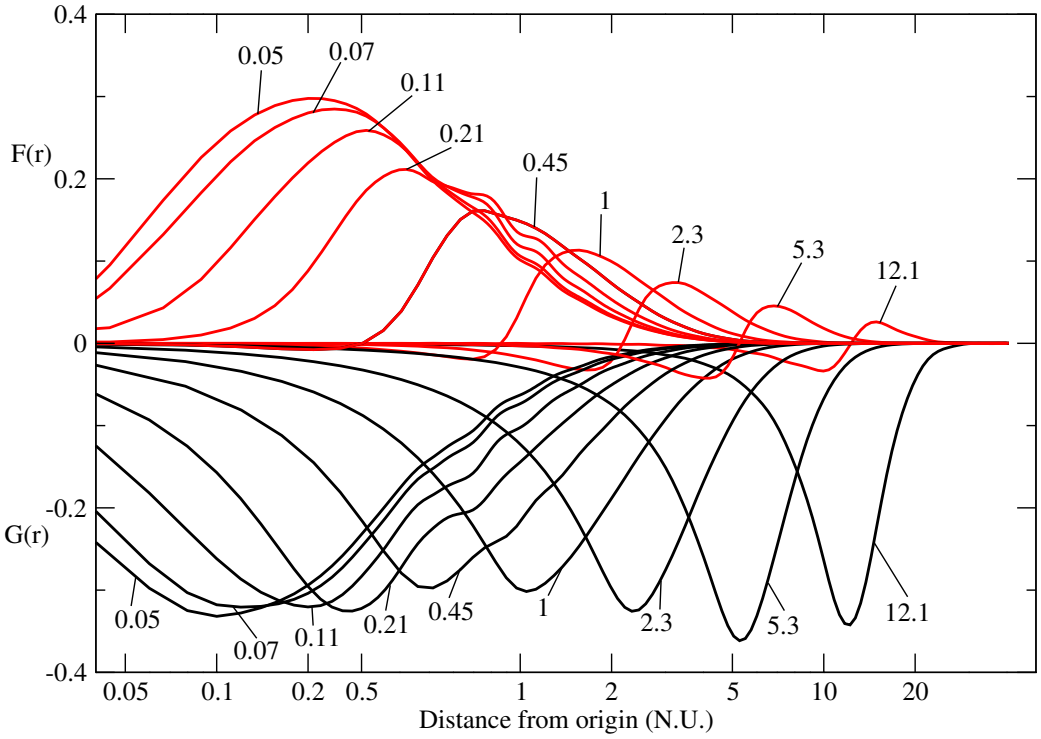

Figure 3.4: The increasing localisation of the large (black curves) and the small components (red curves) for a U^{92+}–U^{91+} quasi–molecule. Eight partial waves are used in the generation of the two–centre basis functions (3.5). At the smallest internuclear distance (0.14 N.U.$\sim$ 44 fm), the peak of the large component is at $\sim$ 44 fm. The internuclear distances, in natural units, which were used for the calculations of the radial components, are specifically designated in the figure and are linked to their corresponding functions.

Chapter 4

The solution of the time–dependent, two–centre Dirac equation

Hitherto, the theory presented has been entirely dedicated to the treatment of the stationary Dirac equation. This is however, only one half of the whole problem. For the atomic systems which will be examined later, the motion of the nuclei adds a time dependency into the Dirac equation which needs accounting for. In this section therefore, the procedure for utilising the numerically derived wavefunctions of the static two–centre Dirac equation, presented in section 3.3, in obtaining solutions to the time–dependent Dirac equation will be elaborated upon. The procedure developed, a type of finite element analysis, is known as the coupled–channel equation; it differentiates itself from other techniques for handling time–dependencies, such as first or second order perturbation theory, in that its application is not limited to systems where the time–dependent fields are small in comparison to the fields of the unperturbed system.

The theory presented here is intended to be general, as there are no overly inhibiting prescriptions for the coupled–channel method that prevent it from being used for an arbitrary time–dependency. For this method, so long as the time–dependency fits the description of an *adiabatic* process, i.e. the Hamiltonian changes slowly enough such that the state function of the system can "instantly" adapt, then the magnitude of the time–dependency is of little concern. It is this general utilisation of the coupled–channel method which commences this section.

4.1 A finite element based approach to treating the time–dependent Dirac equation

The two–centre Dirac equation, for moving nuclei, does not yield a solution analytic in time. In this case, as with its solution in the radial coordinate, numerical procedures must be relied upon. In this section, a type of finite element analysis known as the coupled–channel equation will be presented. The theory of this new method begins with the time–dependent Dirac equation for an arbitrary Hamiltonian $\hat{\mathbf{H}}(t)$

$$i\frac{\partial}{\partial t}\left|\Psi\right\rangle = \hat{\mathbf{H}}(t)\left|\Psi\right\rangle, \tag{4.1}$$

one may separate the state function $|\Psi\rangle$ into temporal and spatial components in the following manner

$$\left|\Psi(t,\mathbf{r})\right\rangle = \sum_n a_n(t)\left|\Phi_n(t)\right\rangle, \tag{4.2}$$

the $\Phi_n(t,\mathbf{r})$ in equation (4.2) are the solutions to the time–independent Hamiltonian, *at a particular fixed time* t. For instance, for the two–centre Dirac equation, these basis functions $\Phi_n(\mathbf{r})$ would simply be those eigenfunctions derived in section 3.3. This expansion is then substituted into the original differential equation (4.1) yielding

$$i\sum_n\left(\frac{\partial a_n(t)}{\partial t}\left|\Phi_n(t)\right\rangle + a_n(t)\left|\frac{\partial\Phi_n(t)}{\partial t}\right\rangle\right) = \sum_k E_k(t)\,a_k(t)\left|\Phi_k(t)\right\rangle, \tag{4.3}$$

left multiplying by $|\Phi_k(t)\rangle$ leads to

$$i\frac{\partial a_k(t)}{\partial t} = E_k(t)\,a_k(t) - i\sum_n a_n(t)\left\langle\Phi_k(t)\left|\frac{\partial\Phi_n(t)}{\partial t}\right\rangle\right. . \tag{4.4}$$

At this point, one must make use of the following relation

$$\begin{aligned}
\frac{\mathrm{d}}{\mathrm{d}t}\hat{\mathbf{H}}(t)\left|\Phi_n(t)\right\rangle &= \frac{\mathrm{d}}{\mathrm{d}t}E_n(t)\left|\Phi_n(t)\right\rangle \\
\frac{\partial\hat{\mathbf{H}}(t)}{\partial t}\left|\Phi_n(t)\right\rangle + \hat{\mathbf{H}}(t)\left|\frac{\partial\Phi_n(t)}{\partial t}\right\rangle &= \frac{\partial E_n(t)}{\partial t}\left|\Phi_n(t)\right\rangle \\
&\quad + E_n(t)\left|\frac{\partial\Phi_n(t)}{\partial t}\right\rangle \\
\left\langle\Phi_k(t)\left|\frac{\mathrm{d}}{\mathrm{d}t}\hat{\mathbf{H}}(t)\right|\Phi_n(t)\right\rangle &= \left\langle\Phi_k(t)\left|\frac{\partial\hat{\mathbf{H}}(t)}{\partial t}\right|\Phi_n(t)\right\rangle \\
&\quad + E_k(t)\left\langle\Phi_k(t)\left|\frac{\partial\Phi_n(t)}{\partial t}\right\rangle\right. \\
&= E_n(t)\left\langle\Phi_k(t)\left|\frac{\partial\Phi_n(t)}{\partial t}\right\rangle\right., \qquad (4.5)
\end{aligned}$$

upon rearranging equation (4.5), one may solve for $\langle\Phi_k(t)\left|\partial\Phi_n(t)/\partial t\right\rangle$

$$\left\langle\Phi_k(t)\left|\frac{\partial\Phi_n(t)}{\partial t}\right\rangle\right. = \frac{\left\langle\Phi_k(t)\left|\frac{\partial\hat{\mathbf{H}}(t)}{\partial t}\right|\Phi_n(t)\right\rangle}{E_n(t) - E_k(t)}, \qquad (4.6)$$

and accordingly, equation (4.4) may be rewritten

$$i\frac{\partial a_k(t)}{\partial t} = E_k(t)\,a_k(t) - i\sum_n a_n(t)\,\frac{\left\langle\Phi_k(t)\left|\frac{\partial\hat{\mathbf{H}}(t)}{\partial t}\right|\Phi_n(t)\right\rangle}{E_n(t) - E_k(t)}\bar{\delta}_{nk}, \qquad (4.7)$$

where $\bar{\delta}_{nk}$ is the anti–Kronecker delta. The next step toward the ultimate evaluation of the expansion coefficients lends itself particularly to those techniques designed to produce basis wavefunctions $|\Phi_n(t)\rangle$ in which the complete spectrum is discretised. The analytic methods described in chapter 2 are only of marginal use with equation (4.7). Basis functions obtained via numerical methods, on the other hand, have a distinct advantage over their analytic counterparts when it comes to solving time–dependent problems with coupled–channel methods since continuum–continuum matrix elements remain easily integrable.

Continuing then under the assumption that the basis is completely discretised, equation (4.7) can be reformulated into a matrix equation

$$
\begin{aligned}
i\frac{\partial \vec{a}\,(t)}{\partial t} &= \hat{M}\,(t)\,\vec{a}\,(t) \quad \text{where} \\
M_{nk} &= E_n\delta_{nk} - i\frac{\left\langle \Phi_k\,(t)\left|\frac{\partial \hat{\mathbf{H}}(t)}{\partial t}\right|\Phi_n\,(t)\right\rangle}{E_n\,(t) - E_k\,(t)}\bar{\delta}_{nk}.
\end{aligned} \tag{4.8}
$$

The following steps rely entirely on more traditional finite element analysis methods; the time derivative on the left hand side of equation (4.8) can only be solved approximately. For this reason, the coupled–channel equation can only be utilised in circumstances where the time–dependencies in the Hamiltonian change slowly enough such that the state function can adjust to them adiabatically. Nevertheless, continuing with the prescribed approach for the time derivative, one obtains

$$
\begin{aligned}
\frac{\partial \vec{a}\,(t)}{\partial t} &\simeq \frac{\vec{a}\,(t+\Delta t) - \vec{a}\,(t)}{\Delta t} = -i\hat{M}\,(t)\,\vec{a}\,(t) \\
\vec{a}\,(t+\Delta t) &= \left(-i\hat{M}\,(t)\,\Delta t + 1\right)\vec{a}\,(t) \simeq e^{-i\hat{M}(t+\Delta t/2)\Delta t}\vec{a}\,(t) + O\left(\Delta t^3\right)
\end{aligned} \tag{4.9}
$$

As a final note, the matrix $\hat{M}$ is exponentiated at $t + \Delta t/2$ in order to preserve the norm of $\vec{a}\,(t)$, expressed differently, it is simply the manifestation of the midpoint rule for numerical integration.

4.2 Coupled–channel methods for the two–centre Dirac equation

The main advantage of coupled–channel techniques in resolving the challenges inherent to the time–dependent, two–centre Dirac equation, is the relative ease with which the time–dependencies may be incorporated into equation (4.9). Here, a brief outline will be given as to how one may embed some typical features of the two–centre Dirac equation into the coupled–channel equation, and as a result, obtain the complete picture of the state function. Specifically, how one may handle collisions with non–zero–impact parameters, as well as alternating electromagnetic fields will be put under the microscope.

Before beginning however, it is imperative to define the trajectory upon which the projectile and target move during the course of the collision. To ensure the most accurate results, the Rutherford trajectories are used for this task, as they correspond to the classical coulomb repulsion. The internuclear distance R, time

t and (for a non–zero–impact parameter) angle ϑ formed between $\mathbf{R}$ and the quantisation axis (z–axis) are parameterised by ξ in the following way

$$\begin{aligned} R &= a(\varepsilon\cosh\xi+1), \quad t=\frac{a}{v_\infty}(\varepsilon\sinh\xi+\xi),\\ a &= \frac{\alpha Z_1 Z_2}{\mu v_\infty^2}, \quad \varepsilon=\left(1+\frac{b^2}{a^2}\right)^{1/2},\\ \vartheta &= 2\arctan\left(\frac{\sqrt{\varepsilon^2-1}\,(\tanh(\xi/2)+1)}{\varepsilon+1-(\varepsilon-1)\tanh(\xi/2)}\right), \end{aligned} \tag{4.10}$$

here, v_∞ is the asymptotic value of the relative velocity of the nuclei at $t=\infty$, b is the impact parameter and $\mu=M_1M_2/(M_1+M_2)$ is the molecular reduced mass. The reason R, t and ϑ are parameterised is due to the fact that the differential equation governing $R(t)$ is autonomous[1], and has no explicit solution in t. Pictorially, this motion and the spatial configuration of this collision is presented in figure 4.1 for the case of a homonuclear collision.

For a collision of two nuclei moving along Rutherford trajectories, with an arbitrary impact parameter, one must utilise a time derivate operator which accounts for the rotation of the internuclear axis. If one assumes that the projectile is deflected by the target in the z–x plane, the new time derivate operator takes the form

$$\frac{\partial}{\partial t}=\frac{\partial\mathbf{R}(t)}{\partial t}\frac{\partial}{\partial R}-i\boldsymbol{\omega}\cdot\mathbf{j}=\frac{\partial\mathbf{R}(t)}{\partial t}\frac{\partial}{\partial R}-i\frac{\mathrm{d}\vartheta}{\mathrm{d}t}\mathbf{j}_y=\frac{\partial\mathbf{R}(t)}{\partial t}\frac{\partial}{\partial R}+\frac{\mathrm{d}\vartheta}{\mathrm{d}t}\frac{(\mathbf{j}_-\mathbf{j}_+)}{2}, \tag{4.11}$$

the ladder operators are defined as

$$\begin{aligned} \mathbf{j}_+|\kappa m_j\rangle &= \sqrt{(j-m_j)(j+m_j+1)}\,|\kappa m_j+1\rangle\\ \mathbf{j}_-|\kappa m_j\rangle &= \sqrt{(j+m_j)(j-m_j+1)}\,|\kappa m_j-1\rangle\,. \end{aligned} \tag{4.12}$$

Using equation (4.11), one may make the appropriate modifications to (4.7) to obtain

[1] One may extract a solution for t which is explicit in terms of R however

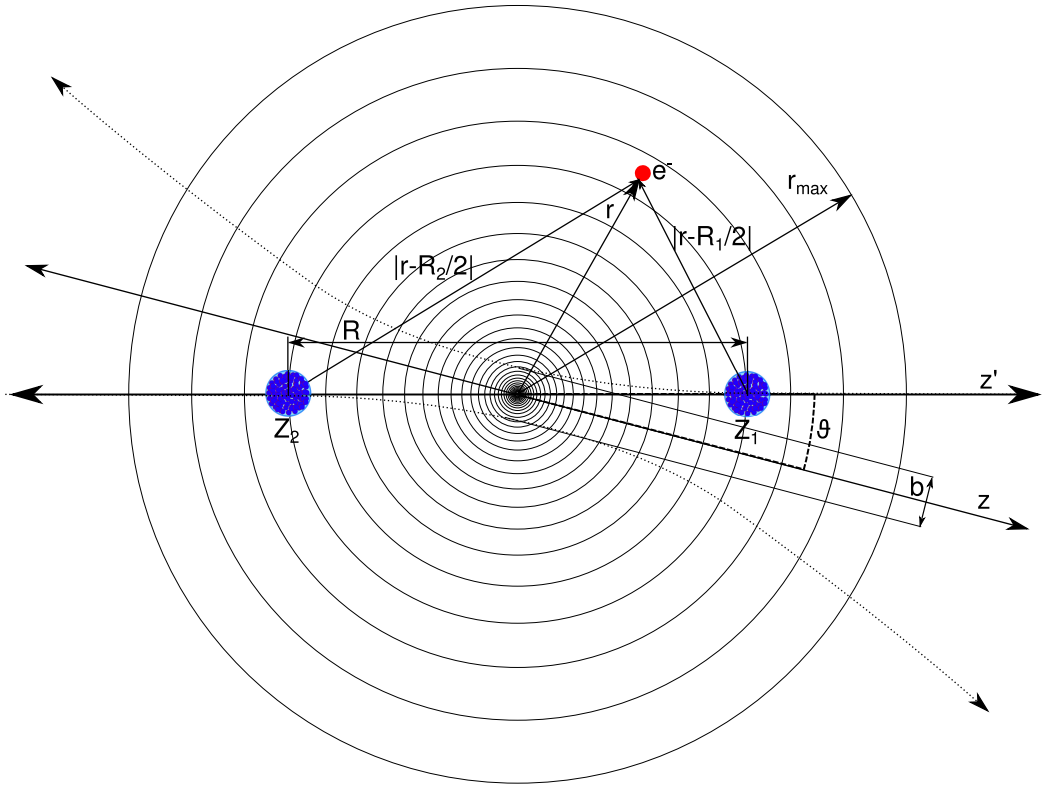

Figure 4.1: A dynamic two–centre system in spherical coordinates showing the trajectories of the projectile and target from the barycentre frame of reference for a collision between nuclei of equal charge and mass. The concentric rings represent the B–spline node boundaries used in the creation of the static two–centre basis, r_{max} shows the extent of the box. The colliding nuclei follow the Rutherford trajectory (dotted, curved lines), furthermore, it is clear to see that for non–zero b, the internuclear axis rotates during the collision.

$$i\frac{\mathrm{d}a_k\left(t\right)}{\mathrm{d}t} = E_k\left(t\right)a_k\left(t\right) - i\sum_n a_n\left(t\right)\left(\frac{\partial R}{\partial t}\frac{\left\langle \Phi_k\left(t\right)\left|\frac{\partial\hat{\mathbf{H}}(t)}{\partial R}\right|\Phi_n\left(t\right)\right\rangle}{E_n\left(t\right)-E_k\left(t\right)}\bar{\delta}_{nk}\right.$$
$$\left. - i\frac{\mathrm{d}\vartheta}{\mathrm{d}t}\left\langle \Phi_k\left(t\right)\left|\mathbf{j}_y\right|\Phi_n\left(t\right)\right\rangle\right). \tag{4.13}$$

The fact that Rutherford trajectories are being employed here means it is sensible to rewrite (4.13) in terms of the parameterising coefficient ξ (4.10). In conjunction with this, appendix B contains a complete discussion as to the simplifications that can be made to equation (4.13) for a zero–impact parameter. Summarising briefly however, should the impact parameter be zero, only states of equal total angular momentum projection can produce non–zero matrix elements for a Hamiltonian of a projectile moving along the z–axis, something which can considerably accelerate the diagonalisation of matrix $\hat{M}$ in equation (4.9).

$$i\frac{\mathrm{d}a_k\left(\xi\right)}{\mathrm{d}\xi} = \frac{\mathrm{d}t}{\mathrm{d}\xi}E_k\left(\xi\right)a_k\left(\xi\right)$$
$$- i\sum_n a_n\left(\xi\right)\left(\frac{\partial R}{\partial \xi}\frac{\left\langle \Phi_k\left(\xi\right)\left|\frac{\partial\hat{\mathbf{H}}(\xi)}{\partial R}\right|\Phi_n\left(\xi\right)\right\rangle}{E_n\left(\xi\right)-E_k\left(\xi\right)}\bar{\delta}_{nk}\right.$$
$$\left. - i\frac{\mathrm{d}\vartheta}{\mathrm{d}\xi}\left\langle \Phi_k\left(\xi\right)\left|\mathbf{j}_y\right|\Phi_n\right\rangle\right). \tag{4.14}$$

With the shift to the parameter ξ, the time dependency in equation (4.9) may be directly substituted by a ξ dependency. Finally, to convey a sense of completeness, it would be wise to give an expression for $a_n\left(t\right)$ that can compensate for any extra time–dependent operator which may be contained within the Hamiltonian. Such an expression would be especially useful when one is confronted with a situation in which the procurement of basis functions with such an additional time–dependent operator becomes excessively prohibitive. Recapitulating, an arbitrary, new Hamiltonian, with an extra time–dependent operator $\hat{\mathbf{L}}$ can be written as

$$\hat{\mathbf{H}}_L\left(t\right) = \hat{\mathbf{H}}\left(t\right) + \hat{\mathbf{L}}\left(t\right), \tag{4.15}$$

where $\hat{\mathbf{L}}\left(t\right)$ may, for instance, take the form of a laser field, in which case

$$\hat{\mathbf{L}}\left(t\right) = \sqrt{\alpha}\boldsymbol{\alpha}\cdot\mathbf{A}\left(\mathbf{r},t\right)e^{i(\mathbf{k}\cdot\mathbf{r}-\omega t)}, \tag{4.16}$$

where $\mathbf{A}(\mathbf{r},t)$ is the vector potential of the laser field and $\mathbf{k}$ the photon wavevector. $\mathbf{A}$ is related to the electric field according to $\mathbf{E}(\mathbf{r},t) = -\partial\mathbf{A}(\mathbf{r},t)/\partial t$. Insertion of this new Hamiltonian into equation (4.1) yields

$$i\frac{\partial}{\partial t}|\Psi\rangle = \hat{\mathbf{H}}(t)|\Psi\rangle + \hat{\mathbf{L}}(t)|\Psi\rangle . \tag{4.17}$$

One may again take equation (4.2) as the expansion for $|\Psi\rangle$, which are still basis functions of $\hat{\mathbf{H}}$. The same procedure between equations (4.2) and (4.14) is then executed, but terms of the operator $\hat{\mathbf{L}}$ remain untouched on the right hand side. One obtains quite simply, where the notation of equation (4.14) has been used

$$\begin{aligned} i\frac{\mathrm{d}a_k(\xi)}{\mathrm{d}\xi} = \frac{\mathrm{d}t}{\mathrm{d}\xi}E_k(\xi)\,a_k(\xi) - i\sum_n a_n(\xi)\Bigg(\frac{\partial R}{\partial\xi}\frac{\left\langle\Phi_k(\xi)\left|\frac{\partial\hat{\mathbf{H}}(\xi)}{\partial R}\right|\Phi_n(\xi)\right\rangle}{E_n(\xi)-E_k(\xi)}\bar{\delta}_{nk} \\ - i\frac{\mathrm{d}\vartheta}{\mathrm{d}\xi}\langle\Phi_k(\xi)|\mathbf{j}_y|\Phi_n(\xi)\rangle + i\frac{\mathrm{d}t}{\mathrm{d}\xi}\left\langle\Phi_k(\xi)\left|\hat{\mathbf{L}}(\xi)\right|\Phi_n(\xi)\right\rangle\Bigg). \end{aligned} \tag{4.18}$$

Further discussion on the inclusion of a laser field in the Hamiltonian has been given in section 7.1. In combination with the two–centre potentials described in section 3.3, the coupled–channel equations (4.14) and (4.18), depending on whether an external field $\hat{\mathbf{L}}$ is present or not, are the second most important, and original, derivation in this thesis. However, no discussion on these numerical methods would be complete without addressing the not inconsiderable computational complexities inherent to their usage, the remainder of this chapter examines therefore, the finer details involved in the implementation of the numerical theory presented thus far.

4.3 Computational implementation of the non–perturbative technique

4.3.1 State tracing and sign

A particularly troublesome, well known [40, 41] programmatical property of using the coupled channel equation, where the basis functions are eigenfunctions of the Hamiltonian (3.1), is ensuring that one can properly trace each state in the eigenvalue spectrum. Ordinarily, linear algebra programs responsible for

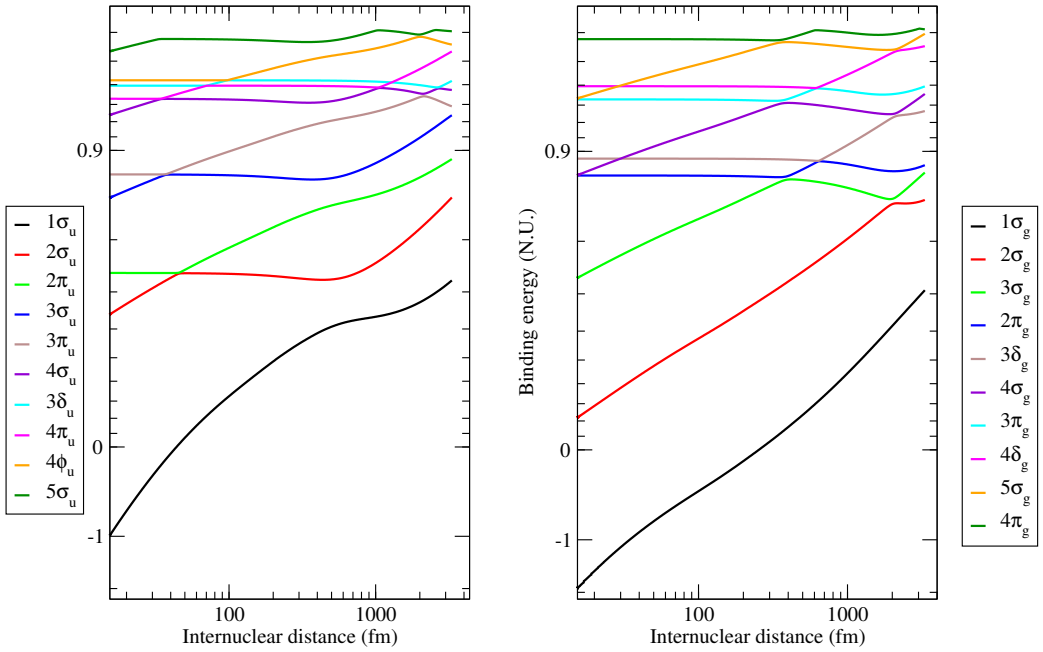

Figure 4.2: The ten lowest *gerade* (right panel) and *ungerade* (left panel) states of a U^{92+}–U^{91+} quasi–molecule as a function of internuclear distance. At 34.487fm internuclear separation, the $1\sigma_g$ state has entered the negative continuum. Of particular note is the crossing of the $4\pi_u$ and the $3\delta_u$ states, the $3\delta_g$ and $4\sigma_g$ states and the $4\delta_g$ and $5\sigma_g$ states. Basis states containing ten different κ, i.e. $\kappa = -5..5$ have been used in determining this spectrum.

determining eigenvalues simply return the eigenvalues, and hence eigenvectors, ordered by energy, and not by quantum numbers, as would be preferable. For a multipole basis, especially in the case of a homonuclear two–centre potential, distinguishing the same state in the eigenvalue spectrum from one time step to the next is an important task to ensure that matrix $\hat{M}$ (4.9) remains well ordered. Figure 4.2 shows clearly that some states in the two–centre spectrum, in this case a U^{92+}–U^{91+} quasi–molecule, definitely cross. The two–centre spectrum shown here utilises ten partial waves (hence $\kappa = -5..5$ in equation (3.5)) and the multipole expansion for the two–centre potential contains therefore 11 terms.

In order to properly sort the two–centre spectrum, it is recommendable to sample the basis functions at each time step, by taking the sum of one or more

components of the basis function[2] $\Phi_{n\mu}(\mathbf{r})$. Introducing the notation

$$\Gamma_n(r) = \sum_{\kappa=-K}^{K} \bar{G}_\kappa(r)\, \chi_{\kappa 1/2}(0,0)\,, \tag{4.19}$$

one may define a sum, conducted at time step t

$$S_{tn} = \left| \sum_i \Gamma_n(x_i) \right|, \tag{4.20}$$

where the x_i are a set of points in the radial coordinate, preferably extending exponentially away from the origin to some sufficiently large value inside the box. This sum S_{tn} can be checked against every other sum calculated in the previous step. The state n which gives the smallest $|S_{t-1,m} - S_{t,n}|$ is then equivalent to the state m of the previous step, the eigenvalue, and expansion coefficients $\nu_{n\kappa}$ for state n should then be reassigned to eigennumber m. This procedure may be further reinforced by restricting the reassignment of eigennumbers only to those states which are "nearest neighbours" in terms of their eigenenergies.

A further problem created by the use of standard linear algebra programs for the diagonalisation of matrix $\mathcal{H}$ in equation (3.7) is the arbitrariness of the sign of the expansion coefficients $\nu_{n\kappa}$. The expansion coefficients are eigenvectors of $\mathcal{H}$, the sign of each expansion coefficient, *relative to every other coefficient* at each new internuclear distance is always correct, however, the sign of the complete set is, if not outright arbitrary then at least highly unpredictable. The result of this cannot be neglected, the matrix elements of two basis states must change smoothly as the internuclear distance between the two centres changes, a sudden change in sign of any of these elements irreversibly distorts the calculation for the ensuing steps.

Again, there exists a method, similar to that employed to counteract the disordering of the eigenvalue spectrum through eigenenergy crossings, to ensure that the sign of each eigenvector remains intact at every time step. Again, one uses a modified sum S_{tn}

$$S_{tn} = \sum_i \Gamma_n(x_i)\,, \tag{4.21}$$

[2] One may choose arbitrarily many components and combinations thereof, sampling of the large and small components in addition to sampling the probability distribution of each state ensures a more reliable check for this procedure

and checks if $|S_{t-1,n} - S_{t,n}| > |S_{t-1,n} + S_{t,n}|$, if this condition is satisfied, a sign change has occurred and one should correspondingly change the sign of the n*th* eigenvalue and eigenvector. It is preferable to also conduct a check of the small component of $\Phi_{n\kappa}(\mathbf{r})$, as the sum over the large component Γ_n, for certain internuclear distances, may approach zero or vice–versa; something which could be a potential source of error in checking the condition $|S_{t-1,n} - S_{t,n}| > |S_{t-1,n} + S_{t,n}|$.

4.3.2 Properties of the basis and the discretised temporal grid

The most demanding task of the non–perturbative treatment of the two–centre Dirac equation outlined here is by far the evaluation of the matrix $\hat{M}$ in equation (4.9). The dimensions of $\hat{M}$, the time required for its evaluation, the accuracy of each individual element and the resources required for its subsequent exponentiation, are dependent on the number of nodes affixed to the B–spline grid, the number of partial waves in the two–centre wavefunctions ($2K$ in equation (3.5)), the size of the box, the cut–off energies of the eigenvalue spectrum, and how finely the temporal grid (or in the case of Rutherford trajectories, ξ grid) is discretised.

The discussion that follows is in part based on heuristics, a result of a long period of trial and error with the non–perturbative approach and its implementation. However some "common sense" decisions can be made about most of the parameters required in the generation of an accurate basis, and for the proper time evolution of the two–centre system.

Firstly, an appropriate box size r_{max} should be relatively simple to find. A box size $O(r_{max}) = 1/(\alpha(Z_1 + Z_2))$ would, for example, be far too small (This value corresponds, in the non–relativistic theory, to the radial expectation value of a ground state electron in a Hydrogen–like system). For atomic systems of very heavy nuclei, where $1/(\alpha(Z_1 + Z_2)) \sim 1$ a box size of $\sim$ 300 N.U. (115000 fm) has been utilised, this of course guarantees that a large portion of the most active bound states are comfortably enclosed within a box of this size.

The number of spline nodes N_m in equation (2.25), and the range of eigenenergies used in the basis must be considered on equal footing, both tend to have an equal contribution to the efficiency of producing $\hat{M}$. A general rule is that doubling the range of the eigenvalue spectrum is as computationally expensive as doubling the number of nodes on the grid. Once more, for the heavy ion collisions considered here, energies of between $-10 < \varepsilon_n < 10$ are acceptable where K– or L– shells are initially populated, non–zero matrix elements of continuum states for energies higher than 10 are strongly suppressed by the factor

$E_n - E_k$ in the denominator of equation (4.8). As for the number of nodes used in the calculations in this thesis, $N_m = 200$ was taken for calculations excluding the negative continuum, and $N_m = 100$ for calculations including the negative continuum. The numerical procedure outlined in this chapter generates an equal number of electron states for energies above and below -1, hence the reason why one may increase the number of splines in the basis, at no extra computational cost, by a factor of two when the negative continuum is excluded.

As for the extent of the temporal grid ξ_{max}, and its subdivisions, a good rule of thumb is to ensure that the range of ξ is chosen such that the maximum internuclear distance of the set of internuclear distances used is at least one order of magnitude larger than $1/(\alpha(Z_1 + Z_2))$. For collisions involving heavy ions, a $\xi_{max} > 6.2$ is usally recommendable, for a 2.33Mev/u U^{92+}–U^{91+} collision, a $\xi_{max} = 6.75$ corresponds to an internuclear separation of $\sim$ 10000fm. Finally, the ξ step $\Delta\xi$ in equation (4.9) should also be sufficiently small, so as to ensure the adiabaticity condition. It has been found that dividing the ξ grid into between 500–1600 steps produces sufficiently similar results.

Though not central to the main message of this thesis, the adjustment of some of these parameters and their interplay is compared in section 7. With the discussion about the computational details and the preceding fundamentals of the developed theory for the non–perturbative treatment of the time–dependent, two–centre Dirac equation complete, the focus now shifts to a brief synopsis of time–dependent perturbation theory. The reader is reminded once more that, considering the novelty of the techniques explained in this chapter, a testbed for comparison is required to ensure that the results given by this non–perturbative technique are able to reproduce those results obtained via the well established perturbation methods. Hence, it would be negligent to not provide the basic theory behind the perturbative approach.

Chapter 5

Time–dependent perturbation theory: Application to the two–centre Dirac equation

Although the main objective of this thesis is to clearly lay out the implementation of the non–perturbative solution method for the time–dependent two–centre Dirac equation, it is not the only method available for the treatment of time–dependent problems. Accordingly, a full account of first order perturbation theory can not be neglected where the two–centre system is strongly heteronuclear, i.e. $Z_2 << Z_1$. The reason for elucidating both methods is because there is no previous theoretical work against which the coupled–channel technique described in chapter 4, which goes beyond the monopole approximation, can be compared. In this sense, the coupled–channel method described here *must* be compared with some other well established technique for dealing with time–dependencies, namely, first order, time dependent perturbation theory.

The method expounded in this section forms the basis for the perturbative calculations which follow in section 6. In order to show the reader the correlation between the figures and tables therein, a brief summary of the theoretical link between the theory shown here, and their appearance in that section is needed. Cross sections for the ionisation of an electron, due to the alpha decay of a heavy nucleus, are calculated using both perturbation theory and the non–perturbative method for the purposes of comparison and confirmation of the validity of the non–perturbative technique laid out in section 4.

Once more, the *DIRAC* program was of assistance in the subsequent calculations using perturbation theory (cf. appendix C).

5.1 Time–dependent perturbation theory

For any quantum mechanical system containing a Hamiltonian in which there exist terms which change with time, a wave equation can be written that describes how the complete wavefunction $|\Psi(\mathbf{r},t)\rangle \equiv |\Psi\rangle$ accomodates these time dependencies. Equations (5.1) to (5.5) have been adapted from [42] and the lecture notes of [43] and are presented here for the case of a *general* perturbation.

To perturbatively reconstruct a solution for $|\Psi\rangle$, one immediately breaks up the Hamiltonian into time–dependent (unperturbed) and time–independent (perturbed) components

$$i\frac{\partial}{\partial t}|\Psi\rangle = \left(\hat{\mathbf{H}}_0 + \lambda\hat{\mathbf{H}}'(t)\right)|\Psi\rangle, \tag{5.1}$$

where $\lambda << 1$, and is a measure of the relative magnitude of the perturbation. The state function is then separated into undetermined time–dependent coefficients and time–independent eigenfunctions of the unperturbed Hamiltonian

$$\begin{aligned}|\Psi\rangle &= \sum_n \sum_{\ell=0}^{\infty} a_n^\ell(t)\,\lambda^\ell \phi_n(\mathbf{r})\, e^{-iE_n t} \\ &= \sum_n \sum_{\ell=0}^{\infty} a_n^\ell(t)\,\lambda^\ell |\phi_n\rangle\, e^{-iE_n t}.\end{aligned} \tag{5.2}$$

The E_n in equation (5.2) are the eigenvalues of the unperturbed Hamiltonian, the term $e^{-iE_n t}$ has been introduced for convenience, but may, if desired, be incorporated into the undetermined coefficient $a_n^\ell(t)$. Inserting equation (5.2) into equation (5.1) one obtains

$$\begin{aligned}i\sum_{\ell=0}^{\infty}\lambda^\ell\left(\frac{\mathrm{d}a_k^\ell(t)}{\mathrm{d}t} - ia_k^\ell(t)\,E_k\right)e^{-iE_k t} = \sum_n\sum_{\ell=0}^{\infty}\lambda^\ell a_n^\ell(t)\Big(E_n \\ + \lambda\left\langle\phi_k\left|\hat{\mathbf{H}}'(t)\right|\phi_n\right\rangle\Big)e^{-iE_n t},\end{aligned} \tag{5.3}$$

where left multiplication by $\langle\phi_k|$, and $\langle\phi_k|\phi_n\rangle = \delta_{n,k}$ has been employed. As is customary, equation (5.3) is sorted into a series of equations for increasing terms in λ. Ignoring the trivial zeroth–order terms, terms to order λ^1 of equation (5.3) are

$$\frac{\mathrm{d}a_k^1(t)}{\mathrm{d}t} = -i\sum_n a_n^0 \left\langle \phi_k \left| \hat{\mathbf{H}}'(t) \right| \phi_n \right\rangle e^{-i\omega t},$$
$$a_k^1(t) = -i\int_{-\infty}^{t} \mathrm{d}\tau \sum_n a_n^0 \left\langle \phi_k \left| \hat{\mathbf{H}}'(\tau) \right| \phi_n \right\rangle e^{-i\omega\tau}, \tag{5.4}$$

the energy difference between states E_n and E_k has been replaced with ω in equation (5.4). For a very broad range of circumstances, it is often not necessary to proceed to second–order perturbation theory, for the sake of providing the reader with a more complete run–down of perturbation theory however, terms of the order λ^2 in equation (5.3) are given by

$$a_k^2(t) = -\int_{-\infty}^{t} \mathrm{d}\tau \int_{-\infty}^{\tau} \mathrm{d}\tau' \sum_n a_n^0$$
$$\left\langle \phi_k \left| e^{iE_k\tau} \hat{\mathbf{H}}'(\tau)\, e^{-i\hat{\mathbf{H}}_0(\tau-\tau')} \hat{\mathbf{H}}'(\tau')\, e^{-iE_n\tau'} \right| \phi_n \right\rangle, \quad \text{introducing}$$
$$\tilde{\mathbf{H}}'(t) = e^{i\hat{\mathbf{H}}_0 t} \hat{\mathbf{H}}'(t)\, e^{-i\hat{\mathbf{H}}_0 t} \quad \text{and} \quad e^{-iE_n t}|\phi_n\rangle = e^{-i\hat{\mathbf{H}}_0 t}|\phi_n\rangle$$
$$a_k^2(t) = -\sum_n a_n^0 \left\langle \phi_k \left| \int_{-\infty}^{t} \mathrm{d}\tau \tilde{\mathbf{H}}'(\tau) \int_{-\infty}^{\tau} \mathrm{d}\tau' \tilde{\mathbf{H}}'(\tau') \right| \phi_n \right\rangle. \tag{5.5}$$

The next stage in the elaboration of perturbation theory, is identifying the correct form of the perturbation Hamiltonian $\hat{\mathbf{H}}'$ for two–centre problems. In this regime, one is in general concerned with the electronic effects induced as a result of some kind of collision. The full Hamiltonian is very similar to that introduced in equation (3.1), however the coordinate centre remains fixed on one nucleus (usually the heavier of the two colliding bodies, otherwise known as a target centred system), and modified to account for the motion of the projectile, again for brevity's sake, point–like nuclei are assumed in the following equations [44]

$$\hat{\mathbf{H}} = \boldsymbol{\alpha}\cdot\mathbf{p} - \frac{\alpha Z_1}{r} - \frac{\gamma(t)\,\alpha Z_2\,(1-\beta(t)\,\boldsymbol{\alpha}_3)}{|\mathbf{r}-\mathbf{R}(t)|} + \boldsymbol{\beta}, \quad \text{where}$$

$$-\frac{\gamma(t)\,\alpha Z_2\,(1-\beta(t)\,\boldsymbol{\alpha}_3)}{|\mathbf{r}-\mathbf{R}(t)|} = \sum_{L=0}^{2K} V_P^L(\mathbf{r},\mathbf{R}(t))$$

$$\sum_{L=0}^{2K} V_P^L(\mathbf{r},\mathbf{R}(t)) = -\gamma(t)\,\alpha Z_2\,(1-\beta(t)\,\boldsymbol{\alpha}_3)$$

$$\times\left[\frac{1}{2\pi^2\gamma(t)}\int\frac{\mathrm{d}^3\mathbf{s}}{s^2-\beta(t)^2\left(\omega/\left(\gamma(t)\,v(t)\right)\right)^2}e^{i\mathbf{s}\cdot(\mathbf{r}-\mathbf{R}(t))}\right], \quad \text{with}$$

$$\beta(t) = v(t)/c, \quad \mathbf{R}(t) = \hat{\mathbf{i}}b + \hat{\mathbf{k}}\gamma(t)\,v(t)\,t,$$

$$R(t) = \left(b^2 + \left(\gamma(t)\,v(t)\,t\right)^2\right)^{1/2},$$

$$\gamma(t) = \left(1-\beta(t)^2\right)^{-1/2}, \tag{5.6}$$

where the electron–projectile interaction is taken to be the Lienerd–Wiechert potential.

The geometry of the collision is displayed in figure 5.1. In equation (5.6), θ is the angle formed between the electron coordinate $\mathbf{r}$ and the quantisation axis and b is the impact parameter. As is often the case for collision events, one usually simplifies $v(t)$ to some constant velocity for a straight line projectile trajectory, this is assumed in equation (5.6).

If the collision corresponds to alpha decay, the Hamiltonian is similar to that of (5.6), but contains some subtle differences [45, 46]

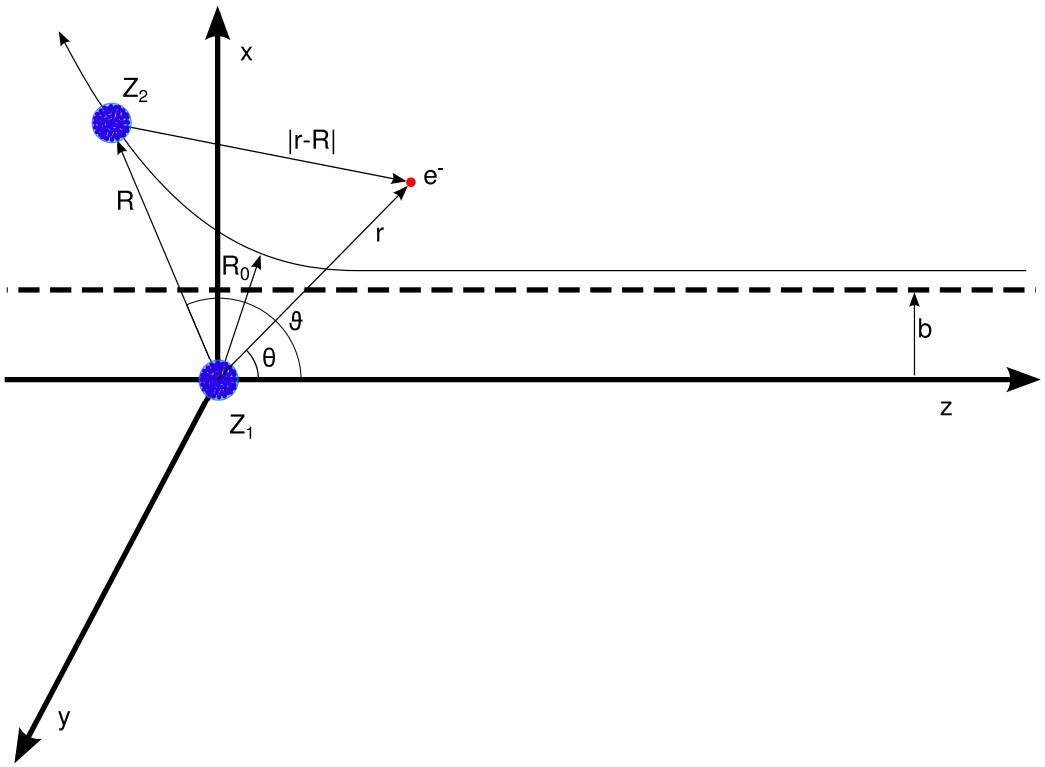

Figure 5.1: A target centred dynamic two–centre system in spherical coordinates showing the trajectory of the projectile for a collision between two different nuclei. If the projectile is assumed to follow the Rutherford trajectory, it moves along the solid, thin, curved line. A common approximation to the particle trajectory however is simply to assume it propagates in the $-z$ direction, along the dashed line, maintaining a constant distance b to the quantisation axis.

$$\begin{aligned}
\hat{\mathbf{H}} = \boldsymbol{\alpha}\cdot\mathbf{p} - \frac{\alpha\left(Z_1+Z_2\right)}{r} + \Theta\left(t\right)\Bigg[& -\frac{\gamma\left(t\right)\alpha Z_2\left(1-\beta\left(t\right)\boldsymbol{\alpha}_3\right)}{\left|\mathbf{r}-\mathbf{R}\left(t\right)\right|} \\
& + \frac{Z_2\alpha}{r} - \frac{\mu}{M_2}\frac{\mathrm{d}^2\mathbf{R}\left(t\right)}{\mathrm{d}t^2}\cdot\hat{\mathbf{K}}\Bigg] + \boldsymbol{\beta} \\
-\frac{\gamma\left(t\right)\alpha Z_2\left(1-\beta\left(t\right)\boldsymbol{\alpha}_3\right)}{\left|\mathbf{r}-\mathbf{R}\left(t\right)\right|} &= \sum_{L=0}^{2K} V_P^L\left(\mathbf{r},\mathbf{R}\left(t\right)\right), \\
V_P^L\left(\mathbf{r},\mathbf{R}\left(t\right)\right) &= -\gamma\left(t\right)\alpha Z_2\left(1-\beta\left(t\right)\boldsymbol{\alpha}_3\right)\times \\
\left[\frac{\rho_<^L\left(rh\left(\theta\right),R\left(t\right)\right)}{\rho_>^{L+1}\left(rh\left(\theta\right),R\left(t\right)\right)}\right. & \left.\times\sqrt{\frac{4\pi}{2L+1}}Y_{L0}\left(\mathbf{r}\right)\right], \\
h\left(\theta\right) &= \sqrt{\sin^2\left(\theta\right)+\gamma\left(t\right)^2\cos^2\left(\theta\right)}, \\
\rho_<\left(r,R\right) = \min(r,R),\ \rho_>\left(r,R\right) &= \max(r,R), \\
\Theta\left(t\right) &= \begin{cases} 1, & t>0 \\ 0, & t\leq 0 \end{cases}. \qquad (5.7)
\end{aligned}$$

For the decay Hamiltonian denoted in equation (5.7), a more detailed approach has been taken in describing the motion of the escaping alpha particle. The terms multiplied by the heaviside function represent the electron–projectile interaction, shake–off and recoil terms respectively. Although the escape trajectory of the alpha particle is always along a straight line[1], in reconstructing the motion of the alpha particle, for best results, one utilises a Coulomb repulsion model, cf. 4.10. It is for this reason that a recoil term resides in the Hamiltonian. As alluded to in equation (3.2), the barycentre should, whenever possible, serve as the coordinate centre, when this is not possible or impractical, a recoil term must be included in the Hamiltonian. In perturbation theory, the requirement of a stable set of atomic basis functions precludes shifting the coordinate centre away from one or the other nucleus[2], hence some term must exist in order to account for the recoiling motion of the parent nucleus after decay. Finally then, this relativistic boost operator $\hat{\mathbf{K}}$ in equation (5.7) has the form [47, 45]

$$\left\langle\phi_n\left|\hat{\mathbf{K}}\right|\phi_k\right\rangle = \frac{E_n+E_k}{2}\left\langle\phi_n\left|\mathbf{r}\right|\phi_k\right\rangle. \qquad (5.8)$$

On the other hand, the non–relativistic boost operator , as applied elsewhere [48], and also applicable to slow moving nuclei, is simply $\hat{\mathbf{K}}=\hat{\mathbf{r}}$.

[1] In this particular case, the alpha particle trajectory is taken along the quantisation axis.

[2] One almost always chooses the coordinate centre as the position of the heaviest nucleus

As dictated by equation (5.1), the time–independent parts of the Hamiltonian must be separated from the time–dependent parts. For the case of a collision event, recognising the perturbation is no difficult task, it is simply $\hat{\mathbf{H}}'(t) = \sum_{L=0}^{\infty} V_P^L(\mathbf{r}, \mathbf{R}(t))$. The perturbation Hamiltonian in the case of alpha decay is simply all those terms contained within equation (5.7) that are multiplied by the heaviside function. This perturbation Hamiltonian is then substituted into equation (5.4) in order to solve for the expansion coefficients a_k^1.

5.2 The evaluation of matrix elements in first order perturbation theory

Once one has identified the perturbation Hamiltonian of a given system, the next task in finding the expansion coefficients of equation (5.2) is the correct evaluation of the matrix elements of the perturbation Hamiltonian.

The analysis of the matrix elements as a result of the perturbation Hamiltonians derived in equations (5.6) and (5.7) is essentially a task of how the matrix element of the time dependent electron–projectile operator is dealt with. The fact that for collision events, the motion of the projectile is often taken to be along a straight line at constant velocity, was not mentioned merely as an observation in passing. It is of significant computational benefit to make this semi–classical approximation. For this case, the matrix element of the electron–projectile operator can be solved analytically, as shall be seen.

If on the other hand, one utilises the Rutherford trajectories in modelling the motion of the projectile (cf. equation (4.10)), then only numerical procedures can be used in evaluating the spatial integrals which arise in these matrix elements. Regarding the evaluation of the matrix elements for the recoil and shake–off operators (5.7), their relatively simple nature should not pose a problem for a moderately experienced theoretician and will not be presented here.

If one observes equation (5.4) once more, it is clear that the matrix element $\left\langle \phi_k \left| \hat{\mathbf{H}}'(\tau) \right| \phi_n \right\rangle$ must be solved. Moreover, per convention, it will be assumed that at $t = -\infty$, a pure state exists, i.e. $a_i^0 = \delta_{n,i}$, hence a first order *transition amplitude* a_{nk} is sought. Using Dirac notation to describe a single state $|\phi_n\rangle \equiv |E_n \kappa m_j\rangle$, equation (5.4) may be reformulated for a perturbation Hamiltonian of the collision given by equation (5.6)

$$a_{nk} = i\int_{-\infty}^{\infty} \mathrm{d}t e^{-i\omega t} \left\langle E_n \kappa_1 m_1 \left| V_P^L \left(\mathbf{r}, \mathbf{R}\left(t\right)\right)\right| E_k \kappa_2 m_2 \right\rangle = -i\,\gamma\alpha Z_2 \int \mathrm{d}^3\mathbf{r}$$
$$\left[\begin{pmatrix} g_{n\kappa_1}\left(r\right)\chi_{\kappa_1}^{m_1} \\ -if_{n\kappa_1}\left(r\right)\chi_{-\kappa_1}^{m_1} \end{pmatrix}^T \int_{-\infty}^{\infty} \mathrm{d}t \frac{e^{-i\omega t}}{\left|\mathbf{r}-\mathbf{R}\left(t\right)\right|} \begin{pmatrix} g_{k\kappa_2}\left(r\right)\chi_{\kappa_2}^{m_2} \\ if_{k\kappa_2}\left(r\right)\chi_{-\kappa_2}^{m_2} \end{pmatrix} - \right.$$
$$\left. \begin{pmatrix} g_{n\kappa_1}\left(r\right)\chi_{\kappa_1}^{m_1} \\ -if_{n\kappa_1}\left(r\right)\chi_{-\kappa_1}^{m_1} \end{pmatrix}^T \int_{-\infty}^{\infty} \mathrm{d}t \frac{e^{-i\omega t}\boldsymbol{\alpha}_3\beta}{\left|\mathbf{r}-\mathbf{R}\left(t\right)\right|} \begin{pmatrix} g_{k\kappa_2}\left(r\right)\chi_{\kappa_2}^{m_2} \\ if_{k\kappa_2}\left(r\right)\chi_{-\kappa_2}^{m_2} \end{pmatrix} \right] \quad (5.9)$$

which may be rearranged as [49]

$$a_{nk} = i\,\alpha Z_2 \sum_{LM} \int_0^{\infty} \frac{s}{s^2-\beta^2q^2}\mathrm{d}s$$
$$\left(-\left\langle \kappa_1 m_1 \left|Y_{LM}\left(\mathbf{r}\right)\right| \kappa_2 m_2 \right\rangle F_{L1}\left(s\right) \right.$$
$$+\beta\left[\left\langle \kappa_1 m_1 \left|\boldsymbol{\sigma}_3 Y_{LM}\left(\mathbf{r}\right)\right| - \kappa_2 m_2 \right\rangle F_{L2}\left(s\right) \right.$$
$$\left. \left. + \left\langle -\kappa_1 m_1 \left|\boldsymbol{\sigma}_3 Y_{LM}\left(\mathbf{r}\right)\right| \kappa_2 m_2 \right\rangle F_{L3}\left(s\right) \right] \right) \times B_{LM}\left(s\right), \quad (5.10)$$

where the path factor $B_{LM}\left(s\right)$ is a direct result of the time integration of the electron–projectile interaction $1/|\mathbf{r}-\mathbf{R}\left(t\right)|$. Using [50, 29, 51]

$$\frac{1}{\left|\mathbf{r}-\mathbf{R}\left(t\right)\right|} = \frac{1}{2\pi^2\gamma}\int \frac{\mathrm{d}^3\mathbf{s}}{s^2-\beta^2q^2} e^{i\mathbf{s}\cdot\left(\mathbf{r}-\mathbf{R}(t)\right)}$$
$$= \frac{1}{2\pi^2\gamma}\int \frac{s^2}{s^2-\beta^2q^2}\mathrm{d}s\, 4\pi \sum_{LM} i^L j_L\left(sr\right)$$
$$\int_0^{\pi}\int_0^{2\pi} \sin\left(\vartheta\right)\mathrm{d}\vartheta\mathrm{d}\varphi Y_{LM}^*\left(\mathbf{s}\right) Y_{LM}\left(\mathbf{r}\right) e^{-i\mathbf{s}\cdot\mathbf{R}(t)}, \quad (5.11)$$

and since

$$\begin{aligned}
\mathbf{s}\cdot\mathbf{R}(t) &= sb\sin(\vartheta)\cos(\varphi)+s\gamma vt\cos(\vartheta) \quad \text{and}\\
\mathscr{F}_{\omega,t}\left(e^{-is\gamma vt\cos(\vartheta)}\right) &= \frac{2\pi}{s}\delta\left(\frac{\omega}{s}-\gamma v\cos(\vartheta)\right), \quad \text{then}\\
\int_{-\infty}^{\infty} e^{-i\omega t}\frac{1}{|\mathbf{r}-\mathbf{R}(t)|} &= \frac{1}{\gamma}\int_0^{\infty}\frac{s}{s^2-\beta^2q^2}\mathrm{d}s\,8\pi\sum_{LM} i^L j_L(sr)\,Y_{LM}(\mathbf{r})\\
&\quad\times Y_{LM}\left(\cos^{-1}\left(\frac{q}{s}\right),0\right)(-i)^M J_M\left(b\sqrt{s^2-q^2}\right),\\
B_{LM}(s) &= 8\pi\, i^L(-i)^M Y_{LM}\left(\cos^{-1}\left(\frac{q}{s}\right),0\right)J_M\left(b\sqrt{s^2-q^2}\right), \qquad (5.12)
\end{aligned}$$

where in equations (5.11) and (5.12), $q=\omega/(\gamma v)$. Only the forms of F and the angular integrals

$$\langle\kappa_1 m_1|Y_{LM}(\mathbf{r})|\kappa_2 m_2\rangle, \quad \text{and} \quad \langle\kappa_1 m_1|\boldsymbol{\sigma}_3 Y_{LM}(\mathbf{r})|\kappa_2 m_2\rangle. \qquad (5.13)$$

need to be determined.

The matrix elements of equation (5.13) can be simplified to [44, 52, 53, 54]

$$\begin{aligned}
\langle\kappa_1 m_1|Y_{LM}(\mathbf{r})|\kappa_2 m_2\rangle &= (-1)^{j_1-m_1}\begin{pmatrix} j_1 & L & j_2\\ -m_1 & M & m_2\end{pmatrix}(-1)^L\\
&\quad\sqrt{2j_1+1}\left\langle\begin{array}{ccc|c} j_1 & L & j_2\\ 1/2 & 0 & 1/2\end{array}\right\rangle\left(1+(-1)^{L+l_1+l_2}\right)\frac{1}{2},\\
\langle\kappa_1 m_1|\boldsymbol{\sigma}_3 Y_{LM}(\mathbf{r})|\kappa_2 m_2\rangle &= (-1)^{j_1-m_1}\sqrt{\frac{3}{4\pi}}\sum_{\ell=0\vee L-1}^{L+1}\left[\left\langle\begin{array}{cc|c} L & 1 & \ell\\ M & 0 & M\end{array}\right\rangle\right.\\
&\quad\sqrt{(2\ell+1)(2L+1)(2j_2+1)(2j_1+1)(2l_2+1)}\\
&\quad\left\langle\begin{array}{cc|c} l_2 & L & l_1\\ 0 & 0 & 0\end{array}\right\rangle\left\{\begin{array}{ccc} l_1 & 1/2 & j_1\\ l_2 & 1/2 & j_2\\ L & 1 & \ell\end{array}\right\}\\
&\quad\left.\begin{pmatrix} j_1 & \ell & j_2\\ -m_1 & M & m_2\end{pmatrix}\right]. \qquad (5.14)
\end{aligned}$$

In the equations (5.14), the 3×3 array in curly braces is a Wigner–9j symbol, the 2×3 array in parenthesis is a Wigner–3j symbol. Finally, the functions F take the following form

$$
\begin{aligned}
F_{L1}(s) &= \int_0^\infty r^2 \mathrm{d}r \, \left(g_{n\kappa_1}(r)\, g_{k\kappa_2}(r) + f_{n\kappa_1}(r)\, f_{k\kappa_2}(r)\right) j_L(sr) \\
F_{L2}(s) &= \int_0^\infty r^2 \mathrm{d}r \, (i) \left(g_{n\kappa_1}(r)\, f_{k\kappa_2}(r)\right) j_L(sr) \\
F_{L3}(s) &= \int_0^\infty r^2 \mathrm{d}r \, (-i) \left(f_{n\kappa_1}(r)\, g_{k\kappa_2}(r)\right) j_L(sr)\,,
\end{aligned} \tag{5.15}
$$

The case of calculating transition amplitudes where nuclear alpha decay induces a perturbation to the system will now be examined. As mentioned earlier, for this particular type of "collision," the ability to switch to the momentum representation, as is the case for straight trajectories and constant projectile velocities, is no longer of satisfactory precision. One of the main reasons for studying the effect alpha decay has on surrounding electrons, is to correctly account for the sudden appearance of the alpha particle at some initial distance from its parent nucleus. In alpha decay, for an arbitrary final velocity, this starting distance can be calculated using the Rutherford trajectories (4.10) at $t = 0$, which is inherently based on motion due to Coulomb repulsion. It is sensible then to utilise the realistic motion of the escaping alpha particle for $R(t)$ in equation (5.7).

In persisting with calculations in coordinate space, a more direct approach to the evaluation of the radial integrals must be taken. As before, a shorthand form for the radial integrals which arise from the perturbation Hamiltonian of (5.7) can be obtained

$$
\begin{aligned}
\mathfrak{F}_{L1}(R) &= \frac{1}{R^{L+1}} \int_0^R r^L r^2 \mathrm{d}r \, \left(g_{n\kappa_1}(r)\, g_{k\kappa_2}(r) + f_{n\kappa_1}(r)\, f_{k\kappa_2}(r)\right) \\
&\quad + R^L \int_R^\infty \frac{1}{r^{L+1}} r^2 \mathrm{d}r \, \left(g_{n\kappa_1}(r)\, g_{k\kappa_2}(r) + f_{n\kappa_1}(r)\, f_{k\kappa_2}(r)\right) \\
-i\mathfrak{F}_{L2}(R) &= \frac{1}{R^{L+1}} \int_0^R r^L r^2 \mathrm{d}r \, \left(g_{n\kappa_1}(r)\, f_{k\kappa_2}(r)\right) \\
&\quad + R^L \int_R^\infty \frac{1}{r^{L+1}} r^2 \mathrm{d}r \, \left(g_{n\kappa_1}(r)\, f_{k\kappa_2}(r)\right) \\
i\mathfrak{F}_{L3}(R) &= \frac{1}{R^{L+1}} \int_0^R r^L r^2 \mathrm{d}r \, \left(f_{n\kappa_1}(r)\, g_{k\kappa_2}(r)\right) \\
&\quad + R^L \int_R^\infty \frac{1}{r^{L+1}} r^2 \mathrm{d}r \, \left(f_{n\kappa_1}(r)\, g_{k\kappa_2}(r)\right).
\end{aligned} \tag{5.16}
$$

One may choose to integrate equations (5.16) directly, or utilise solutions to the following differential equation [51].

$$\begin{aligned}\mathfrak{F}_{L}^{nk}\left(R\right) &= \frac{1}{R^{L+1}}\int_{0}^{R} r^{L}r^{2}\mathrm{d}r\ \left(\mathfrak{R}_{n}\left(r\right)\mathfrak{r}_{k}\left(r\right)\right)\\ &\quad + R^{L}\int_{R}^{\infty}\frac{1}{r^{L+1}}r^{2}\mathrm{d}r\ \left(\mathfrak{R}_{n}\left(r\right)\mathfrak{r}_{k}\left(r\right)\right)\\ \Big(\frac{\mathrm{d}^{2}}{\mathrm{d}R^{2}}+\frac{2}{R}\frac{\mathrm{d}}{\mathrm{d}R}-\frac{L\left(L+1\right)}{R^{2}}\Big)\mathfrak{F}_{L}^{nk}\left(R\right) &= -\left(2L+1\right)\mathfrak{R}_{n}\left(R\right)\mathfrak{r}_{k}\left(R\right).\end{aligned} \tag{5.17}$$

In equation (5.16), owing to the non–relativistic velocities of the alpha particle, the assumption $\gamma\sim 1$ has been made where the evaluation of the angular integrals is concerned; the troublesome term $h\left(\theta\right)$ in equation (5.7) under this assumption is always 1. The derivation of a complete expression of the transition amplitudes due to the electron–alpha particle interaction of alpha decay events can thus be described in terms of the angular matrix elements, and the functions defined in (5.16)

$$\begin{aligned}a_{nk} = -\alpha Z_{2}\sum_{L}\sqrt{\frac{4\pi}{2L+1}}\int_{0}^{\infty}\mathrm{d}t\,\gamma\left(t\right)e^{-i\omega t}\\ \Bigg(\left\langle\kappa_{1}m_{1}\left|Y_{L0}\left(\mathbf{r}\right)\right|\kappa_{2}m_{1}\right\rangle\mathfrak{F}_{L1}\left(R\left(t\right)\right)\\ +\beta\left(t\right)\Big(\left\langle\kappa_{1}m_{1}\left|\boldsymbol{\sigma}_{3}Y_{L0}\left(\mathbf{r}\right)\right|-\kappa_{2}m_{1}\right\rangle\mathfrak{F}_{L2}\left(R\left(t\right)\right)\\ +\left\langle-\kappa_{1}m_{1}\left|\boldsymbol{\sigma}_{3}Y_{L0}\left(\mathbf{r}\right)\right|\kappa_{2}m_{1}\right\rangle\mathfrak{F}_{L3}\left(R\left(t\right)\right)\Big)\Bigg).\end{aligned} \tag{5.18}$$

The only remaining time–dependent part of equation (5.7) which contains angular components is the recoil operator, due to the dot product between $\mathbf{R}(t)$ and $\mathbf{r}$. Since $\mathbf{R}/R=\hat{\mathbf{k}}$ for zero–impact parameter systems such as this, it is clear to see that $\mathbf{R}(t)\cdot\mathbf{r}=rR(t)\cos\left(\theta\right)$. To generate the angular matrix element for this operator, one may use the first of equations (5.14) due to the relation $2\left(\pi/3\right)^{1/2}Y_{10}\left(\theta,0\right)=\cos\left(\theta\right)$.

One special property to note about the representation of transition amplitudes for decay processes is, given the inherent zero–impact–parameter nature of the problem, transitions between states of different total angular momentum projection are strictly forbidden, consequently, there is no sum over M in equation (5.18) as there is in equation (5.10).

Although only the derivation in first order perturbation theory has been laid out here, as shall be shown in tables 6.2 and 6.4, its accuracy and reliability,

when prudently applied, is undoubted. Notwithstanding the value of second order perturbation theory, for the cases considered in later section, the imposition of such an increase in complexity for so little gain is hardly sensible.

Chapter 6

Application of the non–perturbative solution method to the two–centre Dirac equation

Having concluded the rather laborious exposition of the theory, both perturbative and non–perturbative, for time–dependent two–centre problems, the application thereof can now be tested. In this section, two tasks shall be undertaken. The first of these tasks is the comparison of the newly developed non–perturbative technique against perturbation theory. To accomplish this, the cross sections for the alpha decay induced ionisation of electrons initially in the K– and L–shells of heavy nuclei[1] shall be calculated using both techniques. As will be shown, the excellent agreement between both methods provides ample justification for the extension of the non–perturbative theory into regimes involving collisions between heavy, highly charged ions.

Despite the principle achievement of this work being the development and implementation of a working, non–perturbative theory for two–centre problems, the caluclations performed using perturbation theory, for the alpha decay of heavy nuclei are also original, and are derived using the most up to date relativistic operators. Previous studies on the electronic effects of nuclear alpha decay within perturbation theory did not make use of the Lienerd–Wiechert potential to describe the electron–alpha particle interaction, moreover, the relativistic operator for recoil (5.8) has also not been employed previously.

The second task of this section is the non–perturbative analysis of collisions between very heavy, highly–charged nuclei, specifically a U^{92+}–U^{91+} collision. The interest in their study is mainly due to the extremely high potentials that can be generated when the colliding nuclei are brought close enough together,

[1] Only nuclear spin zero nuclei are considered

in this regime, positron–electron pair production, something which should soon be experimentally realised at the upcoming FAIR facility in Darmstadt, Germany [55] becomes a theoretical possibility.

A multitude of works [39, 56, 57, 58, 59, 18, 60, 35] already exist specifically dedicated, in one way or another, to the examination of collisions between heavy, highly charged nuclei and the effects on the bound electrons. The calculations performed in section 6.2 set themselves apart from these previous studies thanks to the unique method of generating basis functions using many terms in the multipole expansion of the two–centre potential, and the implementation of these basis functions with the coupled–channel equation in numerically solving the time–dependent, two–centre Dirac equation.

6.1 Alpha decay

The case chosen for the aforementioned method comparison, the alpha–decay of heavy ions, should provide the perfect theoretical proving ground for the newly developed coupled–channel technique elucidated in section 4.1 and 4.2.

The specific test to be conducted is the evaluation of K– and L–shell ionisation cross sections of electrons emitted as the result of the alpha decay of an initially Hydrogen–like Polonium nucleus. In tables 6.2 and 6.4, the planned comparisons between the exact numerical method, and perturbation theory has been shown.

A subsidiary set of calculations have also been conducted, in deference to the potential shown by alpha decay induced ionisation for use in experimental research. Many phenomena, resulting from the production of vacancies in electronic lower bound states, can be observed should these vacancies be produced as a result of alpha decay. Furthermore, there continues to be strong interest shown in the possibility of vacancy production in lower bound states of highly charged ions [61, 62, 63], alpha decay is one of many vehicles for this process. For this reason, extra calculations have been performed for ionisation cross sections of multiple *neutral* nuclei, Gadolinium, Polonium and Thorium to be precise.

Though these calculations are not directly related to the main intention of comparing the two different time–dependent techniques, the fact that the comparison calculations are conducted for Hydrogen–like nuclei, does not make their results particularly relevant for day to day experimentation. This is especially so in the case where the electron initially resides in the L–shell. Such a construction would most likely be synthesised, and would hence be of limited experimental interest due to the considerable difficulty involved in preparing these heavy, Hydrogen–like ions in an excited state. Furthermore, the inclusion and results of these extra calculations exhibit a certain self consistency, an important characteristic which imparts an additional measure of scientific rigour to the work

performed.

6.1.1 K–shell ionisation probability of Gadolinium, Polonium and Thorium via alpha decay

As mentioned, a comparison is made between the cross sections obtained via non–perturbative and perturbative techniques for the emission of an electron, due to the alpha decay of an initially Hydrogen–like Polonium ion. Moreover, mainly for the sake of maintaining some relevance to experiment and naturally occurring systems, the electron emission probability due to the alpha decay of *neutral* Gadolinium, Polonium and Thorium has been calculated as per the perturbative outline given in section 5.2 for the Hamiltonian (5.7). The same array of calculations for L–shell electron emission will also be carried out in section 6.1.2. Before focussing on the content of the tables and figures herein, a brief outline of the computational methods employed is necessary.

In figures 6.1 and 6.3, and their corresponding values in tables 6.2 and 6.4, the non–perturbative process described in section 4.1 has been used. Partial waves in equation (3.5) range from $\kappa = -3..3$, whilst the multipole expansion for the two–centre potential (3.1) must contain terms $L = 0..6$.

The monopole basis holds 200 B–splines of eighth order confined to a box which extends to 10^5 fm from the coordinate centre, only eigenfunctions with corresponding eigenenergies between $0 < \varepsilon_{n\kappa} < 10$ are included in the final two–centre basis; negative continuum states are excluded from the basis. For these parameters, the final two–centre basis contains approximately 300 different functions $\Phi_{n\mu}(\mathbf{r})$ (cf. equation(3.5)). The electron is assumed to initially occupy the $1s_{1/2}$ state of a *Hydrogen–like* Polonium atom which as located not at the origin, but at $R = R_0\, M_{He}/M_{Po}$, where R_0 is the distance at which the alpha particle first appears, having tunnelled outside of the nuclear potential[2]. The functions of this united atom basis are projected onto the Pb–α basis, whereupon the new occupation probabilities for all states are taken as the initial conditions for the expansion coefficients $a_n(0)$. In order to obtain the ionisation probability with the non–perturbative technique, the sum of the absolute value squared of the expansion coefficients (cf. equation (4.2)) of basis states whose energies exceed 1 is conducted.

$$\sigma_{nm_j} = \lim(t \to \infty) \sum_{n,\varepsilon_n > 1} |a_n(t)|^2 \tag{6.1}$$

[2]A review of this process can be found in [64]

Table 6.1: The screened nuclear charge and corresponding binding energies for Gd, Po and Th for K– and L–shell states

Gd				
	$1s_{1/2}$	$2s_{1/2}$	$2p_{1/2}$	$2p_{3/2}$
Z_{scr}	59.25	48.61	47.35	45.98
E_{exp}	0.9017	0.9836	0.9845	0.9858
Po				
	$1s_{1/2}$	$2s_{1/2}$	$2p_{1/2}$	$2p_{3/2}$
Z_{scr}	78.86	67.66	66.37	63.29
E_{exp}	0.8178	0.9669	0.9682	0.9730
Th				
	$1s_{1/2}$	$2s_{1/2}$	$2p_{1/2}$	$2p_{3/2}$
Z_{scr}	84.82	73.72	72.45	68.67
E_{exp}	0.7854	0.9599	0.9615	0.9681

In figures 6.2, 6.4, 6.5, 6.6 and 6.7, and their corresponding cross section values in tables 6.2, 6.3, 6.4 and 6.5, the perturbation approach has been employed for the calculations. Here, exact, analytic single–centre Dirac wavefunctions form the basis. The transition amplitudes for each of the three interactions, e^-–α interaction, shake–off and recoil, are added together to form a total transition amplitude $a_{\eta k}$ between an initial bound state $\eta = |n\kappa m_j\rangle$ and a final continuum state $k = |\varepsilon\varkappa\mu\rangle$, which can then be used to establish an electron emission cross section

$$\sigma_{nm_j} = \sum_{\varkappa,\mu_s=\pm 1/2} \int_0^\infty \mathrm{d}\varepsilon \int \mathrm{d}\Omega \, |a_{\eta k}|^2 \,. \tag{6.2}$$

The integral over ε in equation (6.2) cannot be executed analytically, hence values for $a_{\eta k}$ at discrete energies in the continuum are found, and an interpolating function is passed through these points, and substituted into (6.2). Six partial waves were used in the final continuum state $|\varepsilon\varkappa\mu\rangle$ (cf. equation (2.15)), hence terms in the multipole expansion of the two–centre potential (3.1) encompass values of $L = 0..3$.

With regard to the "screened" wavefunctions used to emulate a neutral atom, a simplified screening technique, has been chosen. The eigenenergies of the single centre states (cf. equation (2.8)) are, through variance of the charge Z, matched with the experimentally obtained energies given in [65]. This Z is changed each time a cross section is calculated for a different initial bound state, the first few Z_{scr} for each of Gadolinium, Polonium and Thorium are presented in table 6.1

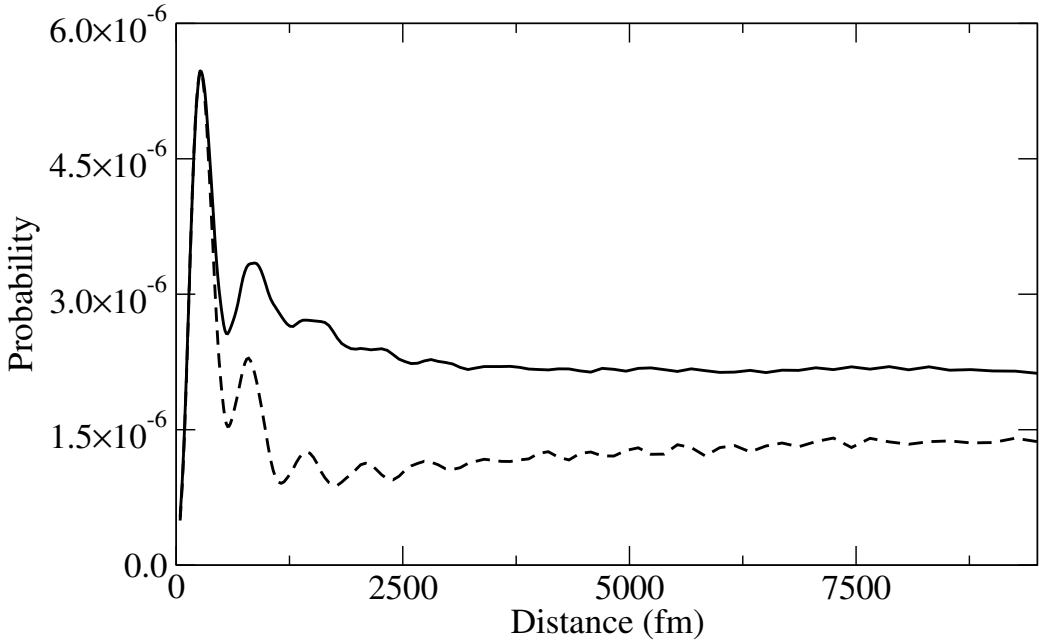

Figure 6.1: The total ionisation probability as a function of internuclear distance of an electron initially bound in the $1s_{1/2}$ state to a Hydrogen–like Polonium atom due to the emergence of a 5.304MeV alpha particle. Curves generated using the non–perturbative technique. The solid line represents calculations performed with s, p and d states *and* seven terms in the two–centre potential expansion, the dashed line represents the monopole approximation to the two–centre potential, thus only s states are included in its eigenbasis.

With these computational subtleties clarified, attention can now turn to the evaluation of cross sections for ionisation of alpha decay susceptible heavy nuclei. The first such calculation, presented in figure 6.1 is the ionisation probability of an electron, initially in the K–shell, as a result of the 5.304MeV alpha decay of Hydrogen–like Polonium. The asymptotic value of the solid line in figure 6.1 is reproduced in table 6.2, and compared against the perturbative calculation for the same atomic process. As can be seen, for the K–shell, the results agree to within less than 1%.

One remark that can be made about figure 6.1 is the inability of the monopole approximation (dashed curve), even for this *almost* spherically symmetric, two–centre potential, to reproduce an acceptable result. These effects are even more pronounced for L–shell electron emission, as will be seen. On the other hand, it is in part confirmation of the probity of the numerical method, that for small internuclear distances, as one would expect, very little difference exists between the monopole approximation, and its more exact counterpart.

Table 6.2: K–shell ionization probability of $^{210}Po^{+83}$ following α–decay. The non–perturbative calculations, performed for $R \to \infty$ by using the monopole as well as exact approximations to the two–center potential, are compared with the first–order perturbation results. The asymptotic kinetic energy of the α particle $T_{\rm kin} = 5.304$ MeV is from Ref. [66]. All probabilities are scaled $\times 10^5$.

Perturbative	Non–perturbative	
	monopole	exact
0.209	0.14	0.21
0.181[46]		
0.203[67]		

The second such calculation for K–shell ionisation is presented in figure 6.2 where the partial electron emission probability $\mathrm{d}p/\mathrm{d}E$ and the full electron emission probability (solid and dashed lines respectively) are presented for Gadolinium, Polonium and Thorium. The kinetic energy of the alpha particles, as per [66], are 3.182, 5.304 and 5.423 MeV respectively. These graphs are based on calculations using semi–classical perturbation theory, as explained in section 5.2. As one would expect, a larger charge for the parent nucleus results in a decreased ionisation probability, a direct result of the fact that heavier parent nuclei have deeper binding energies, thus increasing the threshold for ionisation. The asymptotic values of the dashed lines, the total ionisation probability, are presented in table 6.3.

Table 6.3 also indirectly validates the results in table 6.2 (or vice–versa). Consideration of table 6.1 reveals that the difference between the screened potentials and binding energies, and those of unscreened charges and energies, is quite marginal. The energy of the $1s_{1/2}$ state of unscreened Polonium is according to (2.8) 0.8012 N.U., the screened ground state energy of table 2.8 for Polonium is only 2% greater. Thus, one would expect when comparing probabilities of K–shell ionisation between bases using screened and unscreened wavefunctions, that the difference would be only very subtle. This is indeed the case, for initially neutral and Hydrogen–like Polonium, the difference in K–shell cross sections calculated with perturbation theory is less than 3%.

6.1.2 L–shell ionisation probability of Gadolinium, Polonium and Thorium via alpha decay

In this section, the second comparison calculation between time–dependent methods is presented. The treatment given to the calculation of various K–shell cross sections is applied once more here. The comparison between perturbative and

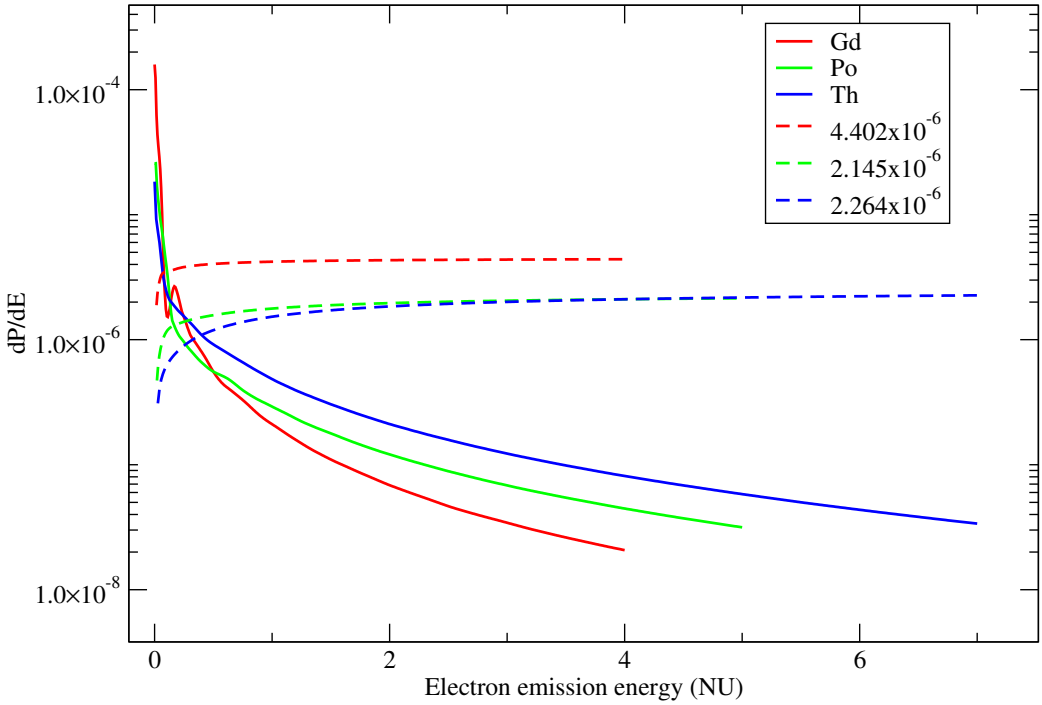

Figure 6.2: The partial ionisation probability of an electron, initially in the $1s_{1/2}$ state, due to the emergence of an alpha particle from an electrically neutral Gadolinium (red), Polonium (green) and Thorium (blue) atom. Alpha particle energies are 3.182, 5.304 and 5.423 MeV respectively. Perturbation methods with a screened potential have been used. The dashed lines are the integrals of their correspondingly coloured solid lines, their asymptotic values are total electron emission probability, and are displayed in the legend.

Table 6.3: K–subshell ionization probabilities of neutral ^{148}Gd, ^{210}Po and ^{228}Th following α–decay. The asymptotic kinetic energy of α particle $T_{\rm kin} = M_\alpha v_\infty^2/2$ from Ref. [66] is given in the second column. Probabilities are scaled $\times 10^5$

Atom	$T_{\rm kin}$ MeV	Perturbation th. shielded potential
^{148}Gd	3.182	0.4402
^{210}Po	5.304	0.2145
^{228}Th	5.423	0.2264

Table 6.4: L–shell ionization probability of $^{210}Po^{+83}$ following α–decay. The non–perturbative calculations, performed for $R \to \infty$ by using the monopole as well as exact approximations to the two–center potential, are compared with the first–order perturbation results. The asymptotic kinetic energy of the α particle $T_{\rm kin} = 5.304$ MeV is from Ref. [66]. All probabilities are scaled $\times 10^5$.

State	Perturbative	Non–perturbative	
		monopole	exact
$2s_{1/2}$	4.80 4.75[46]	4.0	4.96
$2p_{1/2}$	0.54 0.50[46]	0.3	0.64
$2p_{3/2}$	0.61 0.60[46]	0.04	0.61

non–perturbative methods is conducted first, where cross sections for the electron ejection from $2s_{1/2}$, $2p_{1/2}$ and $2p_{3/2}$ shells are evaluated for Po^{83+}. Subsequent to this, calculations of the same cross sections of the alpha decay of screened Gadolinium, Polonium and Thorium nuclei using only perturbation methods.

Table 6.4 represents the second in the set of planned comparisons between perturbation methods, and the exact numerical procedure, the non–perturbative values entered in this table are the asymptotes of the curves visible in figure 6.3. In this figure, the electron emission probability of a Hydrogen–like Polonium ion, where the electron is initially in one of the $2s_{1/2}$, $2p_{1/2}$ or $2p_{3/2}$ states has been calculated using the non–perturbative technique outlined in section 4. The lower panel of figure 6.3 shows the *total* ionisation probability for the $2p_{3/2}$ state, where cross sections of electron emission from subshells with total angular momentum projection $|m_j| = 1/2$ and $|m_j| = 3/2$ have been added together.

For the L–shell ionisation cross sections in table 6.4, both methods seem to produce congruent results, the largest discrepancy is for the $2p_{1/2}$ shell, where the results diverge by some $\sim$19%. The sum of all ionisation probabilites of the L–shell for perturbation theory and the exact numerical approach, match to within less than 5%. One obvious characteristic of the numerical procedure, is that usage of the monopole approximation to the two–centre potential is at best only a weak substitute for calculations utilising higher multipole terms, as witnessed by the woefully poor monopole estimate for the emission probability of an electron from the $2p_{3/2}$ shell.

The secondary objective in this section, generation of a more physically real-

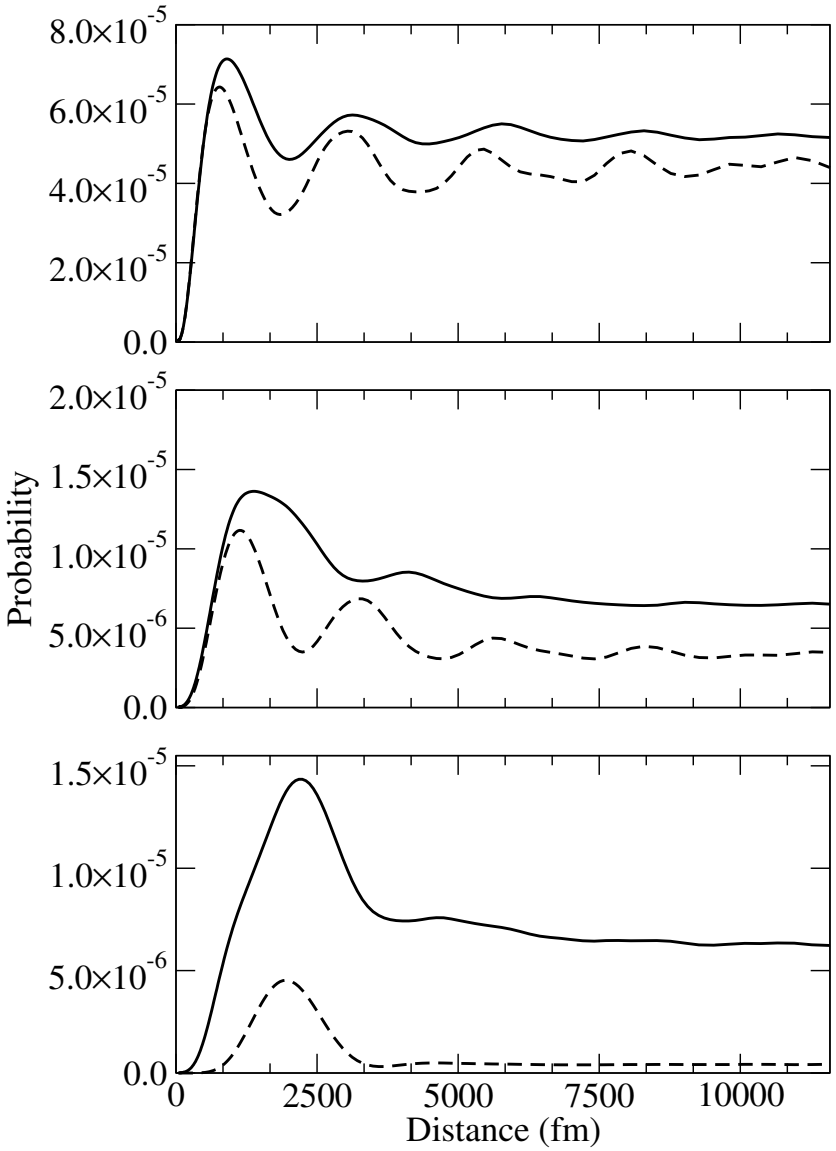

Figure 6.3: The total ionisation probability as a function of internuclear distance of an electron initially bound in the $2s_{1/2}$ (top panel), $2p_{1/2}$ (middle panel) and $2p_{3/2}$ (lower panel) states of a Hydrogen–like Polonium ion due to the emergence of an alpha particle. The solid line represents calculations performed with s, p and d states *and* seven terms in the two–centre potential expansion, the dotted line represents the monopole approximation to the two–centre potential, thus only s, $p_{1/2}$ and $p_{3/2}$ states are included in the eigenbasis respectively.

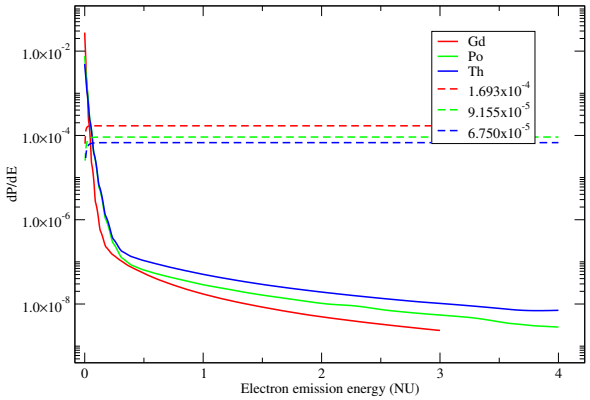

Figure 6.4: The partial ionisation probability of an electron, initially in the $2s_{1/2}$ state, due to the emergence of an alpha particle from an electrically neutral Gadolinium (red), Polonium (green) and Thorium (blue) atom. Perturbation methods with a screened potential has been used. The dashed lines are the integrals of their correspondingly coloured solid lines, their asymptotic values are total electron emission probability.

istic picture of the electronic effects of alpha decay in heavy ions, is accomplished in figures 6.4, 6.5, 6.6 and 6.7. The partial and full electron emission probability has been calculated for an electron initially in the $2s_{1/2}$, $2p_{1/2}$, $2p_{3/2,m_j=1/2}$ and $2p_{3/2,m_j=3/2}$ states respectively with the aid of perturbation theory. Separate graphs have been included for the $2p_{3/2,m_j=1/2}$ and $2p_{3/2,m_j=3/2}$ states in order to calculate the alignment A_{20}, which is defined as

$$A_{20} = \frac{\sigma_{3/2} - \sigma_{1/2}}{\sigma_{1/2} + \sigma_{3/2}}, \tag{6.3}$$

an important factor for any theoretical predictions of any subsequent angular distribution of photons emitted as a result of higher bound electrons which decay into the vacancy created.

A summary of the results attained via perturbation methods is given in table 6.5 for the emission probability of an electron from a neutral alpha emitter. Of particular note is the strongly negative value of A_{20}, the alignment, in each case. Given that the quantisation axis has been chosen along the alpha particle escape vector, this shows that the more the total angular momentum of an electron is projected *parallel* to this axis, the less likely it is that ionisation or indeed excitation will occur.

The results of tables 6.2 and 6.4 should do enough to convince one of the fidelity of the exact numerical method, as outlined in section 4.2. Where perturbation theory can only be applied in scenarios involving small disturbances to an

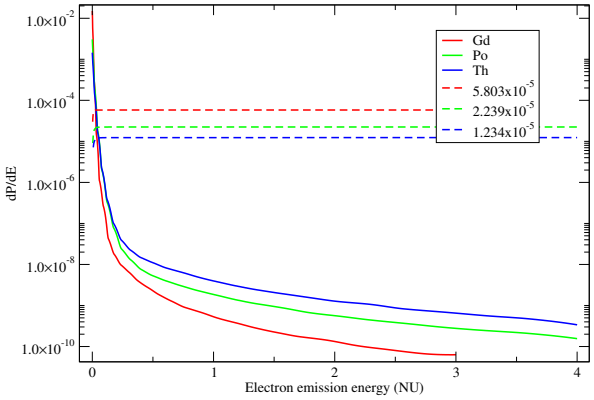

Figure 6.5: The partial ionisation probability of an electron, initially in the $2p_{1/2}$ state, due to the emergence of an alpha particle from an electrically neutral Gadolinium (red), Polonium (green) and Thorium (blue) atom. Perturbation methods with a screened potential has been used. The dashed lines are the integrals of their correspondingly coloured solid lines, their asymptotic values are total electron emission probability.

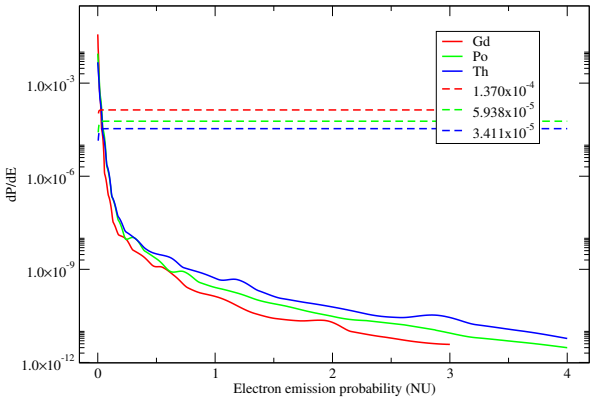

Figure 6.6: The partial ionisation probability of an electron, initially in the $2p_{3/2}$, $m_j = \pm 1/2$ state, due to the emergence of an alpha particle from an electrically neutral Gadolinium (red), Polonium (green) and Thorium (blue) atom. Perturbation methods with a screened potential has been used. The dashed lines are the integrals of their correspondingly coloured solid lines, their asymptotic values are total electron emission probability.

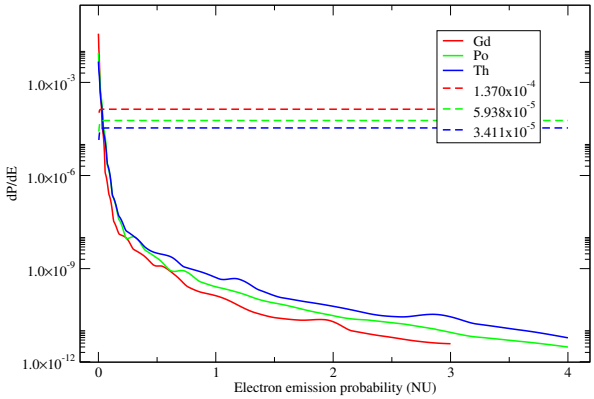

Figure 6.7: The partial ionisation probability of an electron, initially in the $2p_{3/2}$, $m_j = \pm 3/2$ state, due to the emergence of an alpha particle from an electrically neutral Gadolinium (red), Polonium (green) and Thorium (blue) atom. Perturbation methods with a screened potential has been used. The dashed lines are the integrals of their correspondingly coloured solid lines, their asymptotic values are total electron emission probability.

Table 6.5: L–subshell ionization probabilities of neutral ^{148}Gd, ^{210}Po and ^{228}Th following α–decay. The asymptotic kinetic energy of α particle $T_{\rm kin} = M_\alpha v_\infty^2/2$ from Ref. [66] is given in the second column. Probabilities given are scaled $\times 10^5$

Atom	$T_{\rm kin}$	State	Perturbation th. shielded potential
^{148}Gd		$2s_{1/2}$	16.93
		$2p_{1/2}$	5.803
		$2p_{3/2}$, $m_j = \pm 1/2$	13.74
		$2p_{3/2}$, $m_j = \pm 3/2$	1.765
		A_{20}	-0.772
^{210}Po		$2s_{1/2}$	9.155
		$2p_{1/2}$	2.239
		$2p_{3/2}$, $m_j = \pm 1/2$	5.938
		$2p_{3/2}$, $m_j = \pm 3/2$	0.7699
		A_{20}	-0.770
^{228}Th		$2s_{1/2}$	6.750
		$2p_{1/2}$	1.234
		$2p_{3/2}$, $m_j = \pm 1/2$	3.411
		$2p_{3/2}$, $m_j = \pm 3/2$	0.4481
		A_{20}	-0.768

otherwise stable system, a direct solution to the time–dependent Dirac equation for a two–centre potential should be applicable to any scenario[3]. The calculations provided in this section show this to be the case, therefore, the application of the numerical solution method to the time–dependent Dirac equation can now be applied to systems involving more extreme fields.

6.2 Non–perturbative systems

With the vindication of the non–perturbative, numerical method provided by the encouraging results of section 6.1, this method may now be applied to solving the time–dependent Dirac equation for the case of a collision between U^{91+} and U^{92+} ions with a zero–impact parameter. The examination thereof has been split into two categories:

- A collision for which the velocities of the nuclei at $t = \pm\infty$ are *not* high enough to bring the nuclei beyond the critical distance R_c [16], the distance below which, depending on the nuclei involved, the ground state will possess energy $E < -1$.

- A collision for which the projectile *does* have sufficient initial energy to breach the critical distance, and force the ground state deep into the negative continuum.

For reference in regard to this critical distance, a graph of the ground state $1\sigma_g$ of the U^{92+}–U^{91+} quasi–molecule is shown in figure 6.8. An over–critical collision is one which would cause the nuclei to come within less than 34fm, and thus result in the diving of the $1\sigma_g$ state into the negative continuum.

The difference in results of these two cases is considerable enough to warrant separate consideration. Furthermore, there exists some computational nuances which need to be employed for the case of diving of the ground state into the negative energy continuum, nuances which are in need of general explanation. Finally, detailed 3D images of the evolution of the ground state wavepacket have also been produced for the collision between U^{91+} and U^{92+} ions at 2.33MeV/u, an indicator of the potential of this method to be used for such complex tasks as charge transfer calculations.

[3] Provided the adiabaticity condition is satisfied

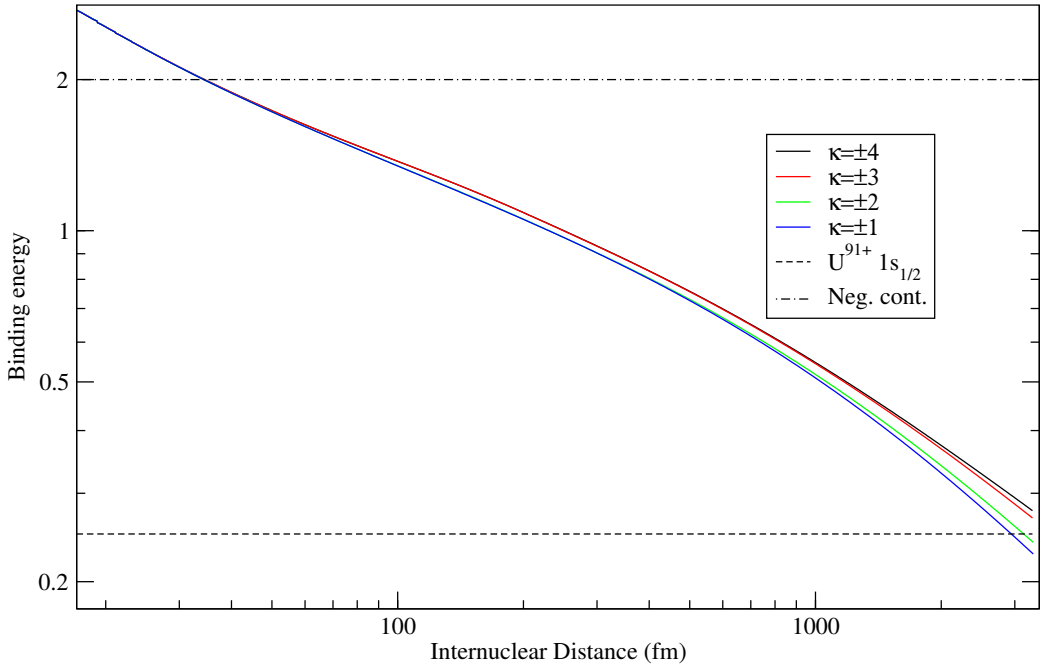

Figure 6.8: The ground state binding energy of the U^{92+}–U^{91+} quasi–molecule as a function of internuclear distance. Also indicated on the graph is the binding energy of the $1s_{1/2}$ state of U^{91+} (dashed line) and the boundary of the negative continuum (dot dashed line). The notation $\kappa = \pm K$ indicates the usage of a two–centre basis containing partial waves from $\kappa = -K \rightarrow K$ (cf. equation (3.5)).

6.2.1 Zero–impact parameter collision between U^{91+} and U^{92+} ions, non–critical velocities

In order to furnish the reader with instructive results, figures and tables have been produced in which bound state excitation and ionisation probability due to a collision between two heavy nuclei will be shown. Before introducing each of the separate graphs, a few words must be given once more to explaining the computational background.

Calculations for the occupation probability of each state $|a_n|^2$ have been conducted for an increasing number of partial waves in the multipole basis. Bound state occupancies are calculated for bases containing 2, 4, 6 and 8 distinct partial waves, or, expressed differently partial waves for $\kappa = -1..1,\ -2..2,\ -3..3,\ -4..4$ respectively. This also implies an equal number of *gerade* and *ungerade* states[4].

Unfortunately, due to the onerous demand on physical resources, calculations including more partial waves in the basis functions were not possible[5]. The box size used extends to just beyond 10^5 fm, 100 different B–splines of eighth order were used for the monopole basis, functions with energies between $-10 < \varepsilon_{n\kappa} < 10$ were used. For a basis comprised of 8 partial waves, this corresponds to about 320 different two–centre basis functions for each of the *gerade* and *ungerade* bases. As for initial conditions, the electron is assumed to be localised in the ground state on one or the other of the Uranium nuclei, this is achieved by setting $a_{1\sigma_g} = a_{1\sigma_u} = 1/\sqrt{2}$. The collision is assumed to "begin" at approximately 8000fm in both of the cases considered. The existence of non–zero coupling matrix elements as R$\rightarrow \infty$ has been accounted for by the introduction of a gaussian dampening function for internuclear distances larger than 5000fm; a common approach to ensure satisfactory boundary conditions [18, 68]. The temporal grid contains 800 nodes equally spaced in ξ, for both types of collision, $\Delta\xi$ of equation (4.9) is ~ 0.017.

Regarding the parameters actually calculated, figures 6.9, 6.10, and 6.12 display bound state occupancies for the two different projectile velocities. Predominantly σ states are shown, as these are the only states produced in the spectrum that are present for all calculations where an increasing number of partial waves are used, comparisons between other bound states would likely be overly confusing, if not outright ill–posed. Moreover, since the electron is assumed to occupy the 1σ state intially, the strongest transitions occur between

[4] these are denoted later on by the subscripts u and g.

[5] Author's note: Though the processor time per step remains acceptably small for more partial waves, the demands on RAM increase considerably. The cluster made available for calculations had only 4GB of RAM at its disposal, almost all of which was required for a calculation with a basis using 10 partial waves, for 12 partial waves, the projected RAM usage exceeds 10GB

σ_g and σ_u states.

In figure 6.11, the total occupancy of the positive continuum is shown for the 2.33MeV/u projectile velocity. In other words, $P_+(R)$

$$P_+(R) = \sum_{\varepsilon_n > 1, n} |a_n|^2 . \tag{6.4}$$

Furthermore, the substantial difference between critical and non–critical collisions is shown in table 6.6, where the probability of excitation among bound *gerade* and *ungerade* states, which is significantly enhanced for an over–critical collision, is compared for both projectile velocities. As the internuclear distance decreases, the *ungerade* part of the ground state electron wavefunction maintains smaller energy gaps between each state in comparison with the *gerade* states. Due to the still very high velocity of the projectile in the 6.717MeV/u collision for internuclear distances between $\sim$ 45 and 16fm and the extremely strong field generated by this heavy quasi–molecule, the $1\sigma_u$ state becomes depleted. This depletion of the $1\sigma_u$ state is thus a significant contributor to the occupancy of states possessing higher energy. Finally, the evolution of the ground state part of the full wavepacket is shown in figure 6.13, the production of which is evidence of the ability for the developed program to be used in calculations of charge transfer probabilities. In the following figures, negative internuclear distances are displayed. These distances correspond to those points during the collision *before* the nuclei have reached the point of nearest approach.

What is evident in figures 6.9 and 6.10 for bound state occupancies, is the inability of the bound state coefficients to quickly converge to an asymptotic value, as a function of increasing partial waves in the basis, especially for the two lowest *gerade* bound states. It is also quite evident that, although a basis containing fewer partial waves exhibits the same general structure as bases of more partial waves, where the calculation of occupancy is concerned, it is in no way a guarantor of reliable results. A discussion on when a basis is "complete" enough to be provide reliable results follows in the conclusion.

On the other hand, the total occupancy of the positive continuum exhibits a remarkably fast convergence toward an asymptotic value, a convergence which one could say is at least as fast as that of the ionisation of an electron due to the far less extreme potential created by the alpha decay of a heavy nucleus. The occupancy of the positive continuum and the intially populated 1σ state at the "end" of the calculation is presented in table 6.6.

Another conclusion which can be made from observation of figure 6.11 is that at the point where the motion of the nuclei is reversed, the tendency of the bound electron to be "shaken–off" into the continuum increases dramatically, small wonder, as at times less than 0, the electrical potential well only increases

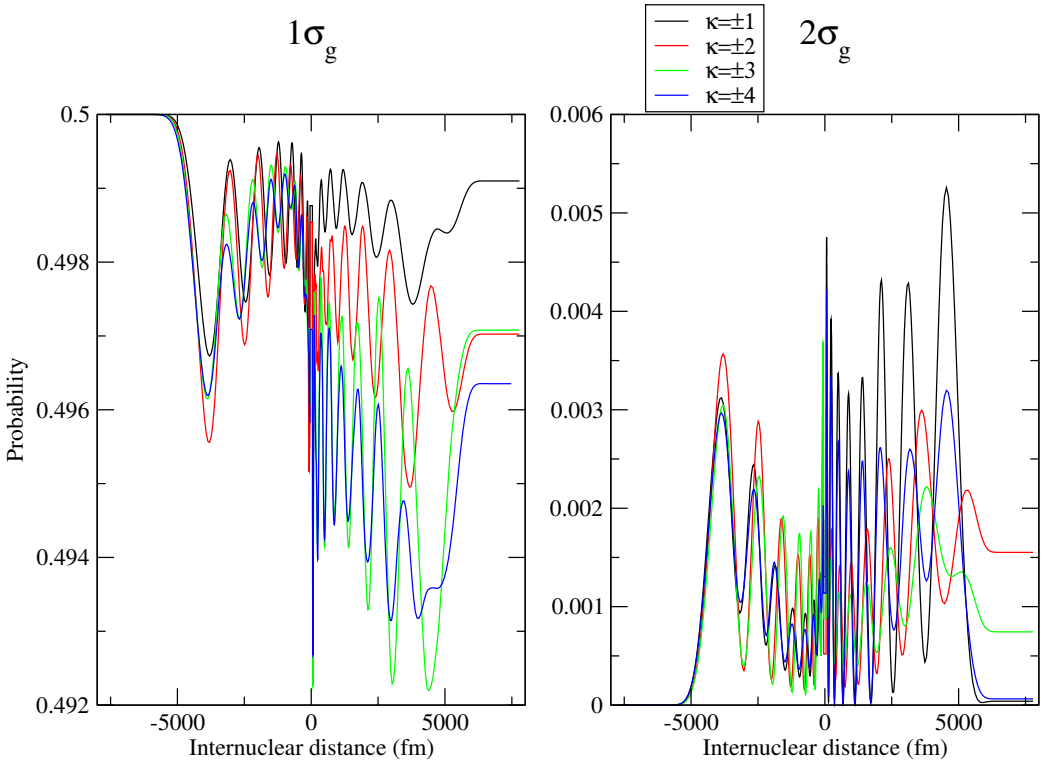

Figure 6.9: Bound state occupancies for the first 2 σ_g states during the collision of U^{92+} and U^{91+} where the projectile moves with an initial velocity of 2.33MeV/u. The electron is initially in the 1σ state.

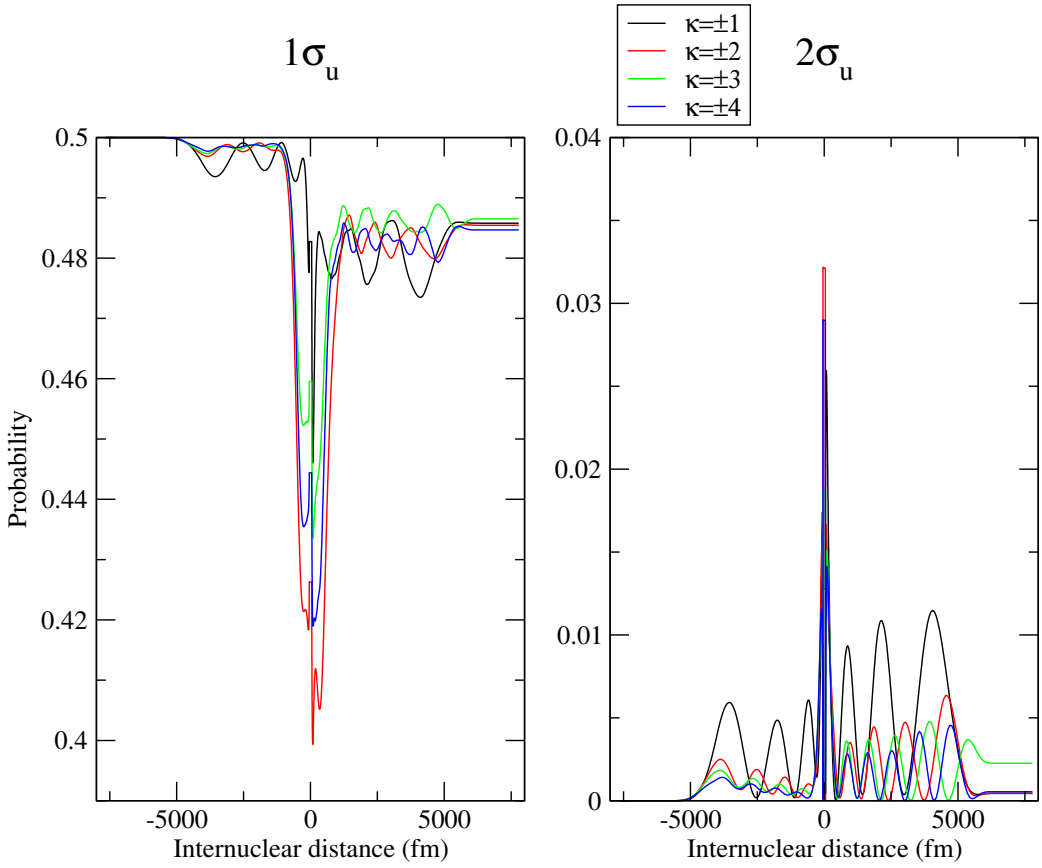

Figure 6.10: Bound state occupancies for the first 2 σ_u states during the collision of U^{92+} and U^{91+} where the projectile moves with an initial velocity of 2.33MeV/u. The electron is initially in the 1σ state.

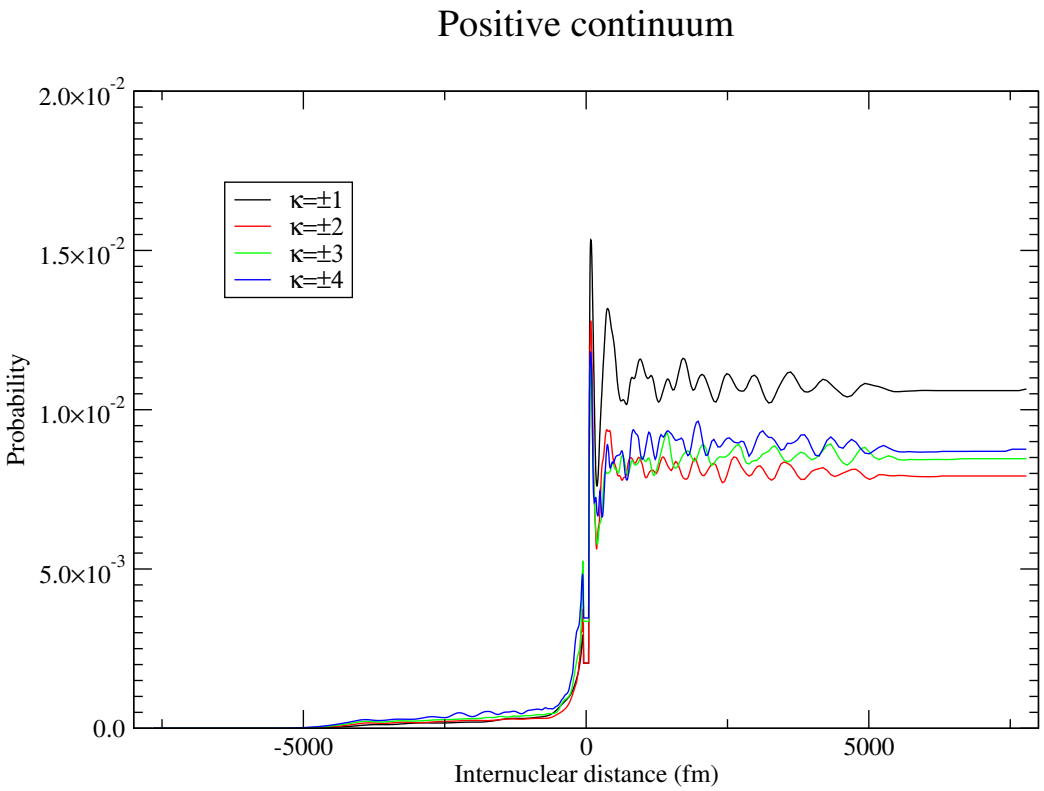

Figure 6.11: Total occupancy of the positive $P_+(R)$ continuum during the collision of U^{92+} and U^{91+} where the projectile moves with an initial velocity of 2.33MeV/u. The electron is initially in the 1σ state.

in depth, after $t = 0$, this potential is weakened and the probability of ejection of the electron from the system increases correspondingly.

6.2.2 Zero–impact parameter collision between U^{91+} and U^{92+} ions at 6.717 MeV/u, diving into the negative continuum

For a higher projectile velocity, it becomes inevitable that the eigenvalue of the $1\sigma_g$ state will assume values lower than -1, hence one refers to such a situation as the "diving" of the ground state into the negative continuum. A special challenge is presented to the theoretician at this point, since simply designating the lowest bound state by observation of the eigenvalue spectrum becomes no longer plausible, failure to account for this can lead to the evolution matrix and the set of expansion coefficients (4.9) becoming disordered.

Fortunately, it is known that states in the negative continuum are localised well away from either nucleus, on the other hand, the true ground state is localised mostly within a region $r = 0..1/(\alpha(Z_1+Z_2))$, as has been shown in figure 3.3. Furthermore, since only the $1\sigma_g$ state dives into the negative continuum, *and* that the monopole approximation is suitable for the description of the wavepacket for small internuclear distances (cf. figure 6.8), one may check the partial normalisation of the $s_{1/2}$ partial waves of all states in the negative continuum, over the range $r = 0..1/(\alpha(Z_1 + Z_2))$. Within this range, only the true ground state will approach the normalisation condition $\int_0^{r_{max}} \mathrm{d}r\, \Phi^*_{n\mu}(\mathbf{r})\, \Phi_{n\mu}(\mathbf{r}) = 1$. This partial normalisation method ensures the traceability of the ground state as it moves through the negative continuum.

However, a problem with the usage of this normalisation technique in tracing the *true* $1\sigma_g$ state while it is in the negative continuum is the fact that its energy is no longer, in the strictest sense, discrete [69, 18, 41]. The distribution of the ground state energy shifts from that of a dirac delta function to a gaussian–like distribution. Although the tracing method mentioned above eliminates the possibility of erroneously selecting a positron state as the $1\sigma_g$ state, there is no 100% guarantee that the state which best fills the tracing criteria is actually the closest to the true resonance peak. Methods do exist for circumventing this problem, such as using a static basis in the coupled channel equation for those internuclear distances where the two nuclei are within the critical distance R_c. The state function produced from this procedure is then projected onto the true adiabatic basis [18].

Such an exhaustive approach into properly accounting for the ground state resonance in the negative continuum is not necessarily within the scope of this thesis, but will however be the subject of future work. For the meantime, some

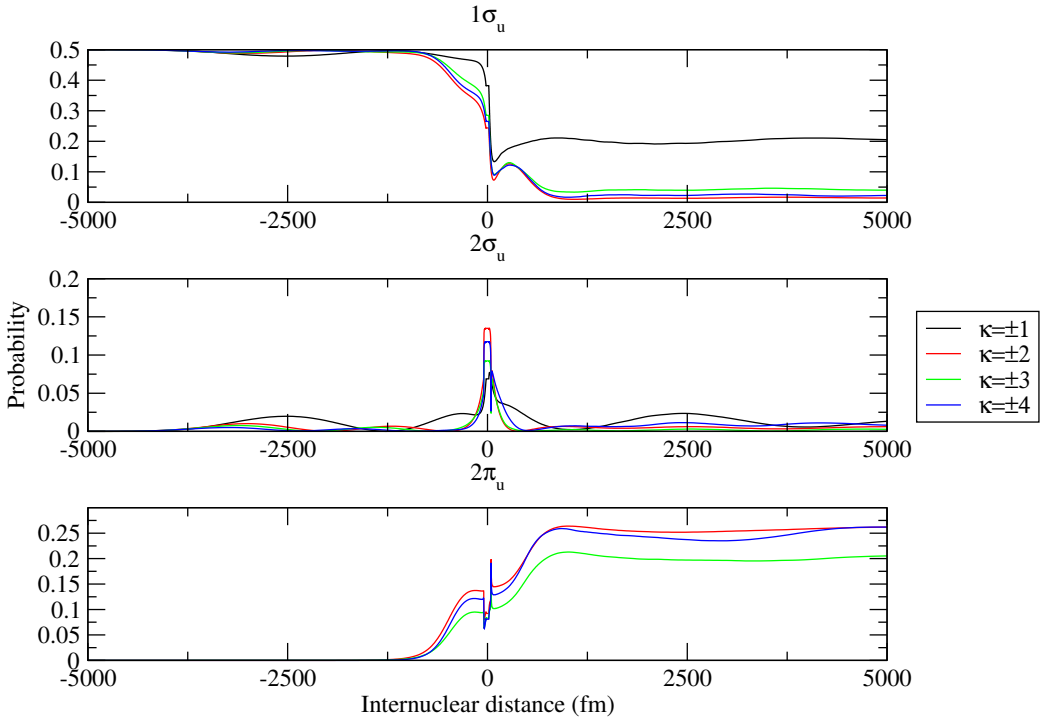

Figure 6.12: Bound state occupancies for the first 3 σ_u states during the collision of U^{92+} and U^{91+} where the projectile moves with an initial energy of 6.717MeV/u. The electron is initially in the 1σ state. The $2\pi_u$ state of non–monopole bases is also shown, it serves to further deplete the population of the $1\sigma_u$ state.

results of the 6.717MeV/u collision between U^{92+} and U^{91+} can be presented without need of such extensive alterations. The *ungerade* states evolve separately from the *gerade* states, and none of these states undergo diving into the negative continuum, hence the lowest *ungerade* state does not become a resonance. A graphic of the evolution of the lowest few bound *ungerade* states is given in figure 6.12.

The most immediately obvious feature of figure 6.12 is of course the increased amplitude of the depletion of the ground state. At these higher collision energies, the much smaller energy gaps between the bound states in the *ungerade* spectrum make excitations and ionisation much more probable than in the case of the 2.33MeV/u collision shown earlier. Where for a projectile energy of 2.33MeV/u, at 44fm the projectile is halted by coulombic repulsion, at 6.717MeV/u, the projectile continues to move at approximately $0.07c$. When combined with the extremely strong fields created for internuclear distances approaching 15fm, transitions among the *ungerade* states are greatly amplified. The result of this, in

Table 6.6: The occupancy of the positive continuum and the 1σ bound state as $t \to \infty$ of a collision between U^{92+}–U^{91+} at a projectile energy of 2.33MeV/u. The $1\sigma_u$ state of a collision between U^{92+}–U^{91+} at 6.717MeV/u, owing to the fact that it is unaffected by "diving" into the negative continuum, is also shown for comparison. These are denoted with the superscript *. The electron is initially in the 1σ state.

Projectile energy (MeV/u)	Partial waves	$\varepsilon > 1$ continuum	$1\sigma_g$	$1\sigma_u$
2.33	$\kappa = -1..1$	0.0107	0.4991	0.4858, 0.2041*
	$\kappa = -2..2$	0.00792	0.4970	0.4854, 0.0143*
	$\kappa = -3..3$	0.00846	0.4971	0.4865, 0.0402*
	$\kappa = -4..4$	0.00876	0.4964	0.4847, 0.0237*

the monopole approximation, is that the continuum is populated at the expense of the $1\sigma_u$ state. Most interestingly however, and again proof of the need to account for higher multipoles, is the significant effect the $2\pi_u$ state has when a basis of higher multipoles is used. The $1\sigma_u$ state is depleted even further in this case, with the $2\pi_u$ state population experiencing a sharp increase, this has also been shown in figure 6.12.

To conclude, the total ground state wavepacket $\left|\langle \mathbf{\Psi}_{1\sigma} | \mathbf{\Psi}_{1\sigma} \rangle\right|^2$ as a function of internuclear distance for a sub–critical collision is presented in figure 6.13. In spite of the full wavepacket not being shown, the fact that, the combined $|a_{1\sigma_g}|^2 + |a_{1\sigma_u}|^2$ occupancy is still almost 100% of the total, for most of the duration of the collision, the ground state wavepacket is by far the most dominant contribution to the total wavepacket and hence provides a good general indication of its overall evolution.

One can conclude from figure 6.13 that the electron "hops" from one nucleus to the other during the part of the collision when the internuclear distance is less than approximately 3000fm. Although figure 6.13 only shows the hopping of the electron for one particular collision velocity, the frequency with which it moves between the nuclei is strongly dependent on the projectile velocity. From a calculational perspective, without proper dampening of the non–diagonal matrix elements, the probability of charge transfer is very much dependent on the point chosen for the commencement of the collision.

From figure 6.13, it is visible that charge transfer processes are taking place, though this is not explicitly calculated here, it is already well understood [35] how dependent this process is on projectile velocity and the point in time where the computational procedure is "turned on."

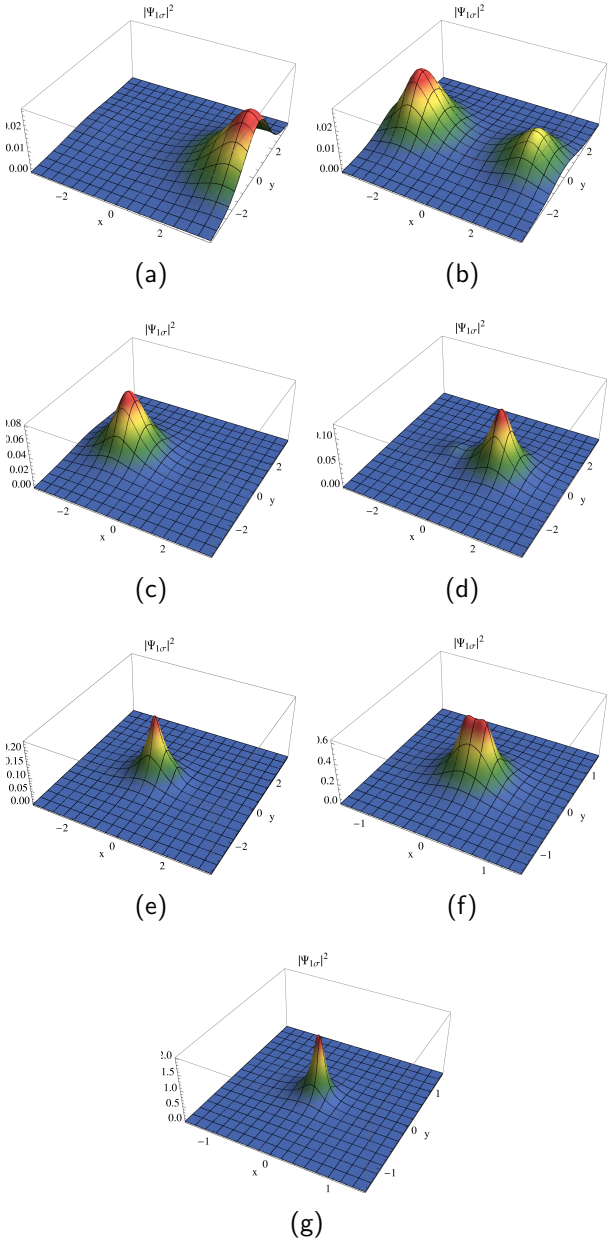

Figure 6.13: The evolution of the 1σ electron before (a→c→e→g) and after (f→d→b) $t = 0$ during a U^{92+}–U^{91+} collision at a projectile velocity 2.33MeV/u. Here $R \sim 2764, 1364, 403$ and 45 fm for panels (a), (c), (e) and (g) respectively and $R \sim 2049, 806$, and 150 fm for panels (b), (d) and (f) respectively. The axes in the horizontal plane are position coordinates in natural units. The delocalisation of the electron is most evident when comparing panels (a) and (b) and (e) and (f). The electron is initially in the 1σ state.

Chapter 7

Conclusions and outlook

A new theoretical method for handling relativistic two–centre problem problems has been developed. Numeric basis functions for single– and two–centre Coulomb potentials have been described in section 3. The programs written implementing these numeric basis functions have shown an excellent agreement with those programs which follow the analytic procedure for extended nuclei explained in section 2.4, usually this agreement is of the order of $10^{-8}\%$ for eigenvalues and capably produces essentially identical bound state eigenfunctions.

For the purposes of comparison, an analytic single–centre basis was used as part of a semi–classical perturbation theory approach in the determination of ionisation cross–sections of an electron from either a K– or the L–shells of Hydrogen–like atoms which undergo alpha decay. The numerical technique against which these results were compared, was derived from the treatment of two–centre potentials given in section 3.3, after which the coupled channel equation mapped this two centre equation (4.14) onto a temporal grid. The results of this non–perturbative technique in finding solutions to the two–centre Dirac equation has proven itself more than capable of reproducing the cross sections obtained via established perturbation methods, as shown in tables 6.2 and 6.4.

The non–perturbative technique was then applied to modelling the state occupancies during a zero–impact parameter collision between U^{92+} and U^{91+}. The astounding consequences of collisions for non– and over–critical projectile velocities for the occupancies of the bound and continuum states are clear to see in table 6.6, where the $1\sigma_u$ displays a strong tendency toward populating higher energy states.

Some computational restrictions do however mean that the non–perturbative method for solving the time–dependent Dirac equation, as it has been programmed and implemented here, should be streamlined for future use. Principle among the shortcomings of this program are its excessive memory requirements, though it does seem realistic that these may be circumvented with minimal or no

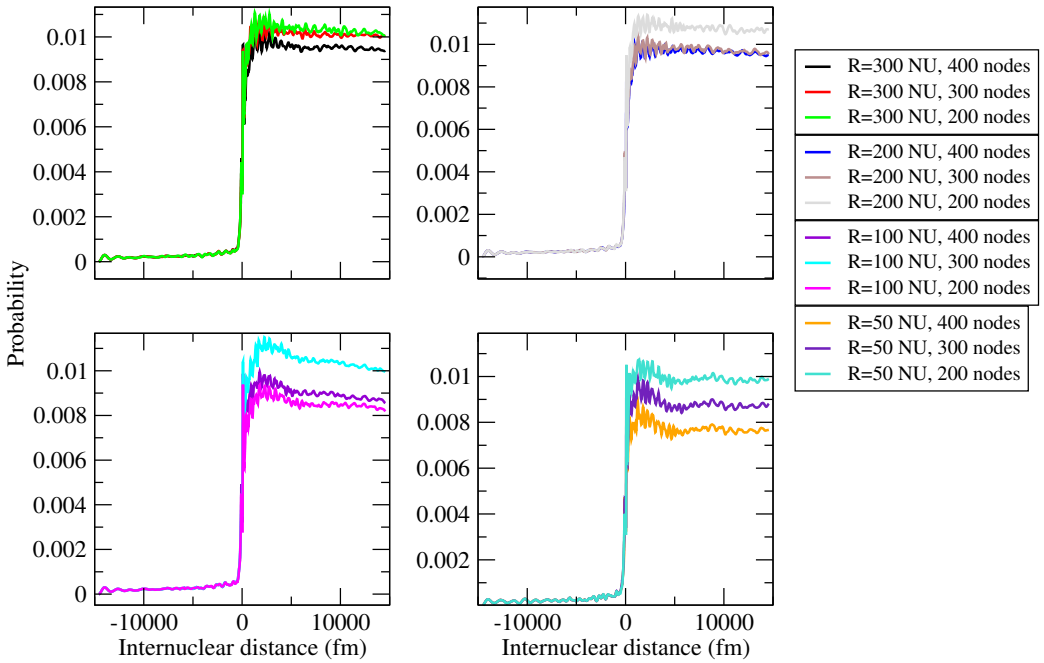

Figure 7.1: The variance of the ionisation probability of an electron, initially in the 1σ state, as a function of box size and spline node during a U^{92+}–U^{91+} collision. The projectile velocity is 2MeV/u and eight partial waves comprise the basis.

increase in computation time. Another issue of the numerical method, especially where the strong fields of heavy nuclei are present, is the completeness of the basis.

The ionisation probability of a U^{92+}–U^{91+} collision is presented in figure 7.1. Each of the panels represents usage of a different box size, ranging from $\sim$ 19300fm to $\sim$ 100000fm. The accuracy of each of the methods is reasonably good, each indicate that the ionisation probability is around 0.008 to 0.01. The bottom right panel of figure 7.1 however, clearly demonstrates the worst precision, this is understandable, as a box size of only 50fm is probably not large enough to accurately encompass some of the more active higher bound states. For increasing box size, the results tend to converge better toward their asymptotic values. Even though, with increasing box size, the precision is constantly improved, increasing the number of spline nodes does not necessarily contribute as much to the distribution of the end result. Given the evidence of 7.1, an accuracy for the results presented for very heavy ion collisions cannot be claimed to anything better than at least 15%.

Another important question regarding the method of calculation in the non–

Table 7.1: The *gerade* and *ungerade* ground state energies of a U^{92+}–U^{91+} quasi–molecule at an internuclear distance of 14625.8fm

$\pm\kappa$	1	5	10	11	12	13
$E(1\sigma_g)$	0.9359	0.8847	0.8390	0.8314	0.8258	0.8184
$E(1\sigma_u)$	0.9426	0.8862	0.8382	0.8320	0.8252	0.8188

perturbative approach is the interlinked problem of boundary conditions and translated wavefunctions. It is quite well known [70, 71, 68, 72, 73] that usage of the coupled channel equation where the basis is comprised of true molecular orbitals, will, at a large enough internuclear distance, erroneously produce non–diagonal matrix elements.

In reality, at extremely large internuclear distances, all non–diagonal matrix elements of $\hat{M}$ in equation (4.9) must be zero. One method to ensure the convergence of these non–diagonal matrix elements to zero is by utilising a "translated wave" modification [74] to the state function as presented in equation (4.2)

$$|\Psi(t,\mathbf{r})\rangle = \sum_n a_n(t)\, e^{-i\gamma_\pm \mathbf{v}\cdot\mathbf{r} - 1/2 v^2 \gamma_\pm^2 t - i\int_{-\infty}^{t} \mathrm{d}\tau\, \varepsilon_n(\tau)} |n(t)\rangle\,, \tag{7.1}$$

where $\gamma_+ = M_1/(M_1+M_2)$ and $\gamma_- = M_2/(M_1+M_2)$. Quite evidently, the term $e^{-1/2 v^2 \gamma_\pm^2 t}$ will unambiguously force all non–diagonal elements to 0 at large t and therefore large R. The only reason one would introduce this modification to the state function is simply due to the fact that the set of basis functions, for the numerical methods used here, cannot accurately produce well defined, Coulomb–Dirac wavefunctions, centred on each nucleus at very large internuclear distances.

This brings into question the choice of boundary conditions. If there are no states in the basis which correspond to the ground state of, in this case, U^{91+}, have prudent choices been made for the initial conditions? It is already clear from figure 6.8, that beyond $\sim$ 2750fm, a basis of only two partial waves will no longer contain a ground state which corresponds to the ground state energy of U^{91+} (0.741135 N.U., for an infinitely deep Coulomb potential). At even larger internuclear distances, as table 7.1 demonstrates, where the ground state energies for many partial wave eigenfunctions are given, only by using the translated wave modification in (7.1), could one expect results of some reasonable validity.

Admittedly, starting the computational routine modelling a collision between two Uranium ions at an internuclear distance of over 14000fm is undoubtedly ill–posed. However, should it be necessary to account for such large internuclear distances, the rightmost column of table 7.1 indicates that even for very many partial waves (26 for the rightmost column of table 7.1), a true ground state of U^{91+} cannot be generated by a pure two–centre spectrum with so few partial

waves, hence, the use of travelling wavefunctions (7.1) may prove more computationally efficient. Travelling wavefunctions have been crudely implemented in the calculations made in this thesis, simply by enforcing a guassian dampening in the off–diagonal matrix elements for the U^{92+}–U^{91+} collision beyond an internuclear separation of 5000fm.

Clearly however, if highly accurate results for heavy quasi–molecule collisions are desired, then many more partial waves will be needed in the basis, possibly between 20–40, certainly more than the maximum eight that were used in section 6.2. Once access is gained to expanded physical resources, these desired expansions will be implemented.

As for the future of the non–perturbative technique developed here, the most obvious, and perhaps easiest to implement extension would be the calculations of cross sections for non–zero–impact parameters. Despite already being reasonably well explored using perturbative techniques [75, 76, 77], such a direct, non–perturbative treatment of the two–centre Dirac equation, where the rotation of the internuclear axis must be accounted for, has, to the author's knowledge, not been quantitatively treated yet, at least for two–centre potentials more complex than the monopole approximation. For experimental purposes, where non–zero–impact parameters are naturally the norm, the future usage of the non–perturbative technique described here shows a great deal of potential.

Despite having already alluded to the extension to non–zero–impact parameter calculations for the numerical treatment of the time–dependent, two–centre Dirac equation, there exists other fields in which an even greater degree of interest would be generated should it produce acceptable results, chief among these field would surely be laser assisted collisions of heavy quasi–molecules.

7.1 Laser assisted collisions

Perhaps the most exciting branch of research for the program developed for treating non–perturbative problems is in the area of laser assisted collisions between two–centres. The tantalising prospect of heavy–ion collisions being able to spontaneously produce positron–electron pairs has unfortunately one major drawback, the interaction time between species able to induce the diving of the ground state into the negative continuum is on the order of zeptoseconds, in general not a long enough time to provide a substantial electron–positron yield.

It has therefore been proposed [78, 79, 80, 81] to combine the effects of intense electromagnetic fields of x–ray frequencies with the strong electrical field created by heavy nuclei, in order to provide the necessary energy "kick" required to better stimulate electron–positron pair production.

As alluded to earlier in section 4.2, a full recount as to how one may incorpo-

rate an electromagnetic field into the coupled–channel equation (4.18) shall be shown here. The Hamiltonian is assumed to have the form of equation (4.15) where a time dependent laser field $\hat{\mathbf{L}}(t)$ is present, the photons propagate along the quantisation axis z, and are polarised in the x direction

$$\begin{aligned}\hat{\mathbf{L}}(t) &= \sqrt{\alpha}\boldsymbol{\alpha}\cdot\mathbf{A}e^{i(\mathbf{k}\cdot\mathbf{r}-\omega t)} = \sqrt{\alpha}\boldsymbol{\alpha}_2 A_0 e^{i(\mathbf{k}\cdot\mathbf{r}-\omega t)} \\ &= 4\pi\sqrt{\alpha}\boldsymbol{\alpha}_2 A_0 e^{-i\omega t}\sum_{L=0}^{\infty} i^L\sqrt{4\pi\left(2L+1\right)}j_L\left(kr\right)Y_L^0\left(\theta,0\right). \end{aligned} \tag{7.2}$$

It is immediately apparent from the form of (7.2) that the following angular matrix elements will be required

$$\begin{aligned}\left\langle \kappa_2 m_2\left|\boldsymbol{\sigma}_2 Y_{L0}\left(\mathbf{r}\right)\right|\kappa_1 m_1\right\rangle &= \sum_{\ell=1}^{L+1}\left\langle\begin{array}{ccc|c} L & 1 & \ell \\ 0 & 0 & 0\end{array}\right\rangle \\ &\sqrt{\left(2\ell+1\right)\left(2L+1\right)\left(2j_2+1\right)\left(2l_2+1\right)\frac{3}{4\pi}}\left\langle\begin{array}{ccc|c} l_2 & L & l_1 \\ 0 & 0 & 0\end{array}\right\rangle \\ &\left\{\begin{array}{ccc} l_1 & 1/2 & j_1 \\ l_2 & 1/2 & j_2 \\ L & 1 & \ell\end{array}\right\}\left(\left\langle\begin{array}{ccc|c} j_2 & \ell & j_1 \\ m_1+1 & -1 & m_1\end{array}\right\rangle - \right. \\ &\left.(-1)^{L+1-\ell}\left\langle\begin{array}{ccc|c} j_2 & \ell & j_1 \\ m_1-1 & 1 & m_1\end{array}\right\rangle\right), \end{aligned} \tag{7.3}$$

which furthermore sets the condition $m_2 = m_1 \pm 1$. Using equation (7.3) a matrix $\hat{\mathcal{L}}$ can be established which agglomerates each different matrix element $\left\langle n\left(t\right)\left|\hat{\mathbf{L}}\left(t\right)\right|p\left(t\right)\right\rangle$

$$\begin{aligned}\mathcal{L}_{np} = \sum_{L=0}^{2K}\sum_{\kappa_n=\pm M_n}^{\pm K}\sum_{\kappa_p=\pm M_p}^{\pm K}\Bigg[& \\ & i\left(\int_0^\infty \mathrm{d}r\,\bar{G}_{p\kappa_p}\left(r\right)j_L\left(kr\right)\bar{F}_{n\kappa_n}\left(r\right)\right)\left\langle\kappa_p m_p\left|\boldsymbol{\sigma}_2 Y_{L0}\left(\mathbf{r}\right)\right|-\kappa_n m_n\right\rangle - \\ & i\left(\int_0^\infty \mathrm{d}r\,\bar{F}_{p\kappa_p}\left(r\right)j_L\left(kr\right)\bar{G}_{n\kappa_n}\left(r\right)\right)\left\langle-\kappa_p m_p\left|\boldsymbol{\sigma}_2 Y_{L0}\left(\mathbf{r}\right)\right|\kappa_n m_n\right\rangle\Bigg] \\ & \times i^L\,4\pi\sqrt{\alpha}\,\sqrt{4\pi\left(2L+1\right)}A_0\,e^{-i\omega t}, \quad M_i = \left|m_i\right|+1/2, \end{aligned} \tag{7.4}$$

where $\bar{G}_{n\kappa}\left(r\right)$ and $\bar{F}_{n\kappa}\left(r\right)$ are defined in equation (3.5). Equation (7.4) indicates the existence of a special consequence, which is most evident for collisions

of homonuclear species. The angular matrix element (7.3) clearly allows mixing between states of different parity. For a homonuclear collision, absent an external electromagnetic field, mixing between the *gerade* and *ungerade* states simply cannot occur, neither due to the changing electrostatic potential, nor due to the rotation of the internuclear axis, should the collision be for a non–zero–impact parameter.

It has already been shown in table 6.6 how significantly the $1\sigma_u$ state is depleted in favour of the occupancy of states of higher energy for over–critical collision velocities, if there should exist some mechanism, such as a powerful electromagnetic field, which could open transition channels between the $1\sigma_g$ state as it dives into the negative continuum, and the *ungerade* positive continuum into which an electron may suddenly be easily promoted, the probability for electron–positron pair production should increase correspondingly.

7.2 Closing remarks

The intended objectives of this compilation have been to grant the reader an insight as to how one can efficiently handle dynamic two–centre problems in relativistic atomic physics and to show the value of the non–perturbative method developed for solving the time–dependent two–centre Dirac equation directly. Despite understandably not providing an exhaustive recount of the solution methods for analytic Dirac eigenfunctions, the set of wavefunctions either quoted (analytic wavefunctions) or derived (numerical non–perturbative wavefunctions) should ensure a versatile set of basis functions is at one's disposal. In combination with the treatment of time–dependencies (chapter 4, section 7.1 and appendix B), a useful, if modest set of theoretical tools have been laid out for the reader.

As for the procedure developed for the non–perturbative treatment of two–centre problems, whilst not wishing to detract from the excellent work already completed in this field, time–dependent analyses of collision events, in which usually the complexity of the basis has been restricted to the monopole approximation, is an area that when considering the demonstrated ability of the method employed here to accomodate higher multipole terms in the basis functions and in the coupled channel equation (4.14), is underdeveloped and which the techniques offered here could go a long way to countering.

Finally, with an eye to future experiments on highly charged quasi–molecules (among other more conventional decay/collision experiments), one may safely assume that the theory, as presented here, has a busy future ahead of it. The groundwork however has already been laid, and it is the author's desire to continue the trajectory of development already undertaken, in meeting the ever mounting challenges which arise as a result of atomic physics experiments.

Appendices

Appendix A

Matrices comprising the Dirac equation

The following matrices are needed for the description of the Hamiltonian (2.2) in the Dirac equation.

$$
\begin{aligned}
\boldsymbol{\alpha} &= \boldsymbol{\alpha}_x\hat{i} + \boldsymbol{\alpha}_y\hat{j} + \boldsymbol{\alpha}_z\hat{k} = \boldsymbol{\alpha}_1\hat{i} + \boldsymbol{\alpha}_2\hat{j} + \boldsymbol{\alpha}_3\hat{k} \\
\boldsymbol{\alpha}_i &= \begin{pmatrix} 0 & \boldsymbol{\sigma}_i \\ \boldsymbol{\sigma}_i & 0 \end{pmatrix} \\
\boldsymbol{\sigma}_x &= \begin{pmatrix} 0 & 1 \\ 1 & 0 \end{pmatrix} \qquad \boldsymbol{\sigma}_y = \begin{pmatrix} 0 & -i \\ i & 0 \end{pmatrix} \qquad \boldsymbol{\sigma}_z = \begin{pmatrix} 0 & 1 \\ -1 & 0 \end{pmatrix} \\
\boldsymbol{\beta} &= \begin{pmatrix} \mathbf{I}_2 & 0 \\ 0 & -\mathbf{I}_2 \end{pmatrix} \qquad \mathbf{I}_2 = \begin{pmatrix} 1 & 0 \\ 0 & 1 \end{pmatrix} \\
\mathbf{p} &= -i\hbar\boldsymbol{\nabla}.
\end{aligned} \tag{A.1}
$$

Appendix B

Modifications to the non–perturbative treatment of the time–dependent Dirac equation for a rotating internuclear axis

The number of eigenfunctions required to generate a complete basis for a dynamic two–centre problem can be significantly reduced if none of the time dependencies induce transitions between states of different momentum projection. For a zero–impact parameter collision between two nuclei, absent any electromagnetic field, the Hamiltonian in equation (5.6) fulfils these conditions. Starting from equation (4.14) for the determination of the expansion coefficients of a two–centre potential

$$\begin{aligned} i\frac{\mathrm{d}a_k(\xi)}{\mathrm{d}\xi} = & \frac{\mathrm{d}t}{\mathrm{d}\xi} E_k(\xi)\, a_k(\xi) \\ & - i\sum_n a_n(\xi) \left(\frac{\partial R}{\partial \xi} \frac{\left\langle k(\xi) \left| \frac{\partial \hat{\mathbf{H}}(\xi)}{\partial R} \right| n(\xi) \right\rangle}{E_n(\xi) - E_k(\xi)} \bar{\delta}_{nk} \right. \\ & \left. - i\frac{\mathrm{d}\vartheta}{\mathrm{d}\xi} \langle k(\xi) | \mathbf{j}_y | n(\xi) \rangle \right), \end{aligned} \tag{B.1}$$

one can, for the zero–impact parameter collision mentioned, explicitly define a state $|n\rangle$ in terms of energy, and a fixed total angular momentum projection μ. It makes sense to set μ to be the momentum projection of the initial state, K–shell

ionisation for instance would imply $\mu = \pm 1/2$. The subsequent simplification for equation (B.1) gives a more explicit expression

$$i\frac{\mathrm{d}a_{\varepsilon}\left(\xi\right)}{\mathrm{d}\xi} = \frac{\mathrm{d}t}{\mathrm{d}\xi}\varepsilon\left(\xi\right)a_{\varepsilon}\left(\xi\right) - i\sum_{E} a_{E}\left(\xi\right)\left(\frac{\partial R}{\partial \xi}\frac{\left\langle k_{\varepsilon}\left(\xi\right)\left|\frac{\partial \hat{\mathbf{H}}(\xi)}{\partial R}\right|n_{E}\left(\xi\right)\right\rangle}{E\left(\xi\right)-\varepsilon\left(\xi\right)}\right)\bar{\delta}_{E\varepsilon}. \tag{B.2}$$

If, however, symmetry breaking conditions like that of a non–zero–impact parameter, or an electromagnetic field are introduced, defining a single state $|n\rangle$ must account for different momentum projections, using the notation in equation (3.5), this may be achieved in the following way

$$|n\rangle \equiv |n\mu\rangle = \sum_{i,\kappa=-K}^{K}\begin{cases} 0, & |\kappa| < |\mu| + 1/2 \\ \nu^{i}_{n\kappa}\phi^{i}_{n\kappa\mu}(\mathbf{r}), & |\kappa| \geq |\mu| + 1/2 \end{cases}. \tag{B.3}$$

The consquences of extending the basis when accounting for interactions which induce transitions between states of differing μ are clear: If one includes N different angular momentum projection substates for each eigenenergy, the size of the matrix in equation (B.2) increases N^2–fold. In the calculation using 8 different partial waves in sections 6.2.1 and 6.2.2, using momentum projections from $-3/2..3/2$ would have resulted in the creation of a basis of 1280 functions for *each* of the *gerade* and *ungerade* states, thus in total 2560 basis functions. The diagonalisation of such a large matrix[1] is a considerably laborious task for commercially available processors. For this reason, the theoretician needs to proceed judiciously when considering how best to program his/her code.

[1] 104.8576 MB for double precision complex entries

Appendix C

The DIRAC package for Mathematica

To assist with the perturbative calculations performed in sections 6.1.1 and 6.1.2, use was made of the *DIRAC* program for *Mathematica*. The *Mathematica* version [26] of this program is an update from an earlier *Maple* program [25].

Many functions used in perturbation theory, such as $B_{LM}(s)$ and the $F_L(s)$ of equations (5.12) and (5.15) respectively, are implemented in *DIRAC* and require no programmatic derivation. Furthermore, other such useful features, like quickly converting measurements between unit systems, hydrogen–like eigenvalues and eigenfunctions (including those for extended nuclei) are also available among other features.

It is important to point out that this package is not limited to calculations involving two–centre problems, it contains many common subroutines required for the study of a variety of time–dependent and time–independent problems.

Bibliography

[1] P. A. M. Dirac, "The quantum theory of the electron," *Proc. R. Soc. Lond. A*, vol. 117, pp. 610–624, 1928.

[2] B. Bransden and C. Joachain, *Physics of Atoms and Molecules*. John Wiley & Sons, New York, 1983.

[3] E. A. Hylleraas, "Über die elektronenterme des wasserstoffmoleküls," *Z. Phys. A: Hadron Nucl.*, vol. 71, pp. 739–763, 1931.

[4] G. Jaffé, "Zur Theorie des Wasserstoffmolekülions," *Z. Phys. A: Hadron Nucl.*, vol. 87, pp. 535–544, 1934.

[5] O. Burrau, "Berechnung des energiewertes des wasserstoffmolekel-ions (H2+) im normalzustand," *Kong. Dansk. Vidensk.*, vol. 7, p. 14, 1927.

[6] V. Guillemin and C. Zener, "Hydrogen ion wave function," vol. 15, no. 4. National academy of Science, 1929, pp. 314–318.

[7] P. M. Morse and E. C. G. Stückelberg, "Diatomic molecules according to the wave mechanics I: Electronic levels of the hydrogen molecular ion," *Phys. Rev.*, vol. 33, pp. 932–947, 1929.

[8] E. Teller, "Über das Wasserstoffmolekülion," *Z. Phys. A: Hadron Nucl.*, vol. 61, pp. 458–480, 1930.

[9] B. N. Dickinson, "The normal state of the hydrogen molecule-ion," *J. Chem. Phys.*, vol. 1, no. 5, pp. 317–318, 1933.

[10] D. R. Bates, K. Ledsham, and A. L. Stewart, "Wavefunctions of the hydrogen molecular ion," *Phil. Trans. R. Soc. Lond. A*, vol. 246, pp. 215–240, 1953.

[11] H. O. Pritchard and H. A. Skinner, "Some considerations on the strengths of hybrid bonds in excited states of the hydrogen molecule-ion," *J. Chem. Soc.*, vol. 2, pp. 945–952, 1951.

[12] W. Gordon, "Die Energieniveaus des Wasserstoffatoms nach der Diracschen Quantentheorie des Elektrons," *Z. Phys. A: Hadron Nucl.*, vol. 48, pp. 11–14, 1928.

[13] W. Pieper and W. Greiner, "Interior electron shells in superheavy nuclei," *Z. Phys. A: Hadron Nucl.*, vol. 218, pp. 327–340, 1969.

[14] U. Becker, N. Grün, W. Scheid, and G. Soff, "Nonperturbative treatment of excitation and ionization in $U^{92+} + U^{91+}$ collisions at 1 gev/amu," *Phys. Rev. Lett.*, vol. 56, pp. 2016–2019, 1986.

[15] B. Müller, J. Rafelski, and W. Greiner, "Solution of the dirac equation with two coulomb centres," *Phys. Lett. B*, vol. 47, no. 1, pp. 5 – 7, 1973.

[16] J. Rafelski and B. Müller, "The critical distance in collisions of heavy ions," *Phys. Lett. B*, vol. 65, no. 3, pp. 205 – 208, 1976.

[17] J. Reinhardt and W. Greiner, "Quantum electrodynamics of strong fields," *Rep. Prog. Phys.*, vol. 40, no. 3, pp. 219–295, 1977.

[18] J. Reinhardt, B. Müller, and W. Greiner, "Theory of positron production in heavy-ion collisions," *Phys. Rev. A*, vol. 24, pp. 103–128, 1981.

[19] G. Soff, W. Greiner, W. Betz, and B. Müller, "Electrons in superheavy quasimolecules," *Phys. Rev. A*, vol. 20, no. 1, pp. 169–193, 1979.

[20] K.-H. Wietschorke, P. Schluter, and W. Greiner, "The dirac equation in orthogonal coordinate systems. II. The two-centre dirac equation," *J. Phys. A: Math. Gen.*, vol. 16, no. 9, pp. 2017–2034, 1983.

[21] Y. B. Zeldovich and V. S. Popov, "Electronic structure of superheavy atoms," *Sov. Phys. Uspekhi*, vol. 14, no. 6, p. 673, 1972.

[22] H. Backe, "Heavy ion collisions and atomic physics," *Nucl. Phys. A*, vol. 400, pp. 451 – 472, 1983.

[23] O. Kullie and D. Kolb, "High accuracy dirac-finite-element (FEM) calculations for H^{2+} and Th^{179+}," *Eur. Phys. J. D*, vol. 17, no. 2, pp. 167–173, 2001.

[24] A. N. Artemyev, A. Surzhykov, P. Indelicato, G. Plunien, and T. Stöhlker, "Finite basis set approach to the two-centre dirac problem in cassini coordinates," *J. Phys. B: At., Mol., Opt.*, vol. 43, no. 23, p. 235207, 2010.

[25] A. Surzhykov, P. Koval, and S. Fritzsche, "Algebraic tools for dealing with the atomic shell model. I. Wavefunctions and integrals for hydrogen-like ions," *Comput. Phys. Commun.*, vol. 165, pp. 139–156, 2004.

[26] S. R. McConnell, S. Fritzsche, and A. Surzhykov, "Dirac: A new version of computer algebra tools for studying the properties and behavior of hydrogen-like ions," *Comput. Phys. Commun.*, vol. 181, no. 3, pp. 711 – 713, 2010.

[27] W. Greiner, *Relativistic Quantum Mechanics: Wave Equations*, 3rd ed. Springer–Verlag, 1981.

[28] H. A. Bethe and E. E. Salpeter, *Quantum mechanics of one- and two-electron atoms*. Springer, 1957.

[29] J. Eichler and W. E. Meyerhof, *Relativistic Atomic Collisions*. Academic Press, 1995.

[30] B. Müller, J. Rafelski, and W. Greiner, "Electron wave functions in over-critical electrostatic potentials," *Il Nuovo Cimento A*, vol. 18, pp. 551–573, 1973.

[31] R. T. Deck, J. G. Amar, and G. Fralick, "Nuclear size corrections to the energy levels of single–electron and –muon atoms," *J. Phys. B: At., Mol., Opt.*, vol. 38, no. 13, pp. 2173–2186, 2005.

[32] W. Johnson, S. Blundell, and J. Sapirstein, "Finite basis sets for the dirac equation constructed from B splines," *Phys. Rev. A*, vol. 37, pp. 307–315, 1988.

[33] V. M. Shabaev, I. I. Tupitsyn, V. A. Yerokhin, G. Plunien, and G. Soff, "Dual kinetic balance approach to basis-set expansions for the dirac equation," *Phys. Rev. Lett.*, vol. 93, no. 13, p. 130405, 2004.

[34] G. B. Deineka, I. A. Maltsev, I. I. Tupitsyn, V. M. Shabaev, and G. Plunien, "Relativistic calculations of electronic excitation probabilities in U^{92+}–U^{91+} (1s) collisions in the monopole approximation," *Russ. J. Phys. Chem. A*, vol. 6, pp. 224–228, 2012.

[35] I. I. Tupitsyn, Y. S. Kozhedub, V. M. Shabaev, G. B. Deyneka, S. Hagmann, C. Kozhuharov, G. Plunien, and T. Stöhlker, "Relativistic calculations of the charge-transfer probabilities and cross sections for low-energy collisions of H–like ions with bare nuclei," *Phys. Rev. A*, vol. 82, p. 042701, 2010.

[36] F. Fillion-Gourdeau, E. Lorin, and A. Bandrauk, "Numerical solution of the time-independent dirac equation for diatomic molecules: B splines without spurious states," *Phys. Rev. A*, vol. 85, p. 022506, 2012.

[37] C. de Boor, *A practical guide to splines*. Springer, 1978.

[38] A. Igarashi, "B-spline expansions in radial dirac equation," *J. Phys. Soc. Jpn.*, vol. 75, no. 11, p. 114301, 2006.

[39] E. Ackad and M. Horbatsch, "Calculation of electron-positron production in supercritical Uranium–Uranium collisions near the coulomb barrier," *Phys. Rev. A*, vol. 78, p. 062711, 2008.

[40] K.-H. Wietschorke, P. Schluter, G. Soff, K. Rumrich, and W. Greiner, "Relativistic two-center continuum," *Phys. Rev. A*, vol. 36, no. 1, pp. 377–380, 1987.

[41] K. Rumrich, W. Greiner, G. Soff, K.-H. Wietschorke, and P. Schluter, "Continuum states of the two-centre dirac equation," *J. Phys. B: At., Mol., Opt.*, vol. 22, no. 2, pp. 165–187, 1989.

[42] H. Eyring, J. Walter, and G. Kimball, *Quantum Chemistry*. John Wiley & Sons, 1946.

[43] V. S. Batista, "Introductory quantum chemistry," 2002, http://www.chem.yale.edu/ batista/vvv/v570.pdf.

[44] S. R. Valluri, U. Becker, N. Grün, and W. Scheid, "K-shell ionisation in relativistic heavy-ion collisions," *J. Phys. B: At., Mol.*, vol. 17, no. 21, p. 4359, 1984.

[45] R. Anholt and P. A. Amundsen, "K-shell ionization during α decay," *Phys. Rev. A*, vol. 25, no. 1, pp. 169–177, 1982.

[46] J. Law, "Inner shell electron ejection in the alpha-decay of ^{210}Po," *Nucl. Phys. A*, vol. 286, no. 2, pp. 339 – 353, 1977.

[47] P. A. Amundsen, "On the role of dipole transitions in the semiclassical approximation for K-shell ionisation," *J. Phys. B: At., Mol., Opt.*, vol. 11, no. 18, p. 3197, 1978.

[48] J. S. Blair and R. Anholt, "Theory of K-shell ionization during nuclear resonance scattering," *Phys. Rev. A*, vol. 25, no. 2, pp. 907–920, 1982.

[49] S. R. McConnell, A. N. Artemyev, and A. Surzhykov, "Alignment of atomic inner-shells following alpha-decay-induced ionization," *J. Phys. B: At., Mol., Opt.*, vol. 44, no. 14, p. 145204, 2011.

[50] L. Kocbach, "On the evaluation of SCA matrix elements for inner shell ionization by heavy charged particles," *Z. Phys. A: Hadron Nucl.*, vol. 279, pp. 233–236, 1976.

[51] L. Kocbach, J. Hansteen, and R. Gundersen, "Review of the SCA method for inner shell ionization - results, limitations and possibilities," *Nucl. Instrum. Methods*, vol. 169, pp. 281–291, 1980.

[52] D. Brink and G. Satchler, *Angular momentum*. Clarendon Press, 1968.

[53] M. Rose, *Elementary theory of angular momentum*. John Wiley & Sons, 1957.

[54] V. V. Balashov, A. N. Grum-Grzhimailo, and N. M. Kabachnik, *Polarization and Correlation Phenomena in Atomic Collisions: A Practical Theory Course*. Kluwer Academic, 2000.

[55] A. Gumberidze, T. Stöhlker, H. Beyer, F. Bosch, A. Bräuning-Demian, S. Hagmann, C. Kozhuharov, T. Kühl, R. Mann, P. Indelicato, W. Quint, R. Schuch, and A. Warczak, "X-ray spectroscopy of highly-charged heavy ions at FAIR," *Nucl. Instrum. Meth. B*, vol. 267, no. 2, pp. 248 – 250, 2009.

[56] U. Müller, T. de Reus, J. Reinhardt, B. Müller, W. Greiner, and G. Soff, "Positron production in crossed beams of bare uranium nuclei," *Phys. Rev. A*, vol. 37, pp. 1449–1455, 1988.

[57] W. Betz, G. Soff, B. Müller, and W. Greiner, "Direct formation of quasimolecular 1sσ vacancies in uranium-uranium collisions," *Phys. Rev. Lett.*, vol. 37, pp. 1046–1049, 1976.

[58] U. Müller-Nehler and G. Soff, "Electron excitations in superheavy quasimolecules," *Phys. Rep.*, vol. 246, no. 3-4, pp. 101 – 250, 1994.

[59] K. Momberger, N. Grün, and W. Scheid, "Coupled channel analysis of electron-positron pair production in relativistic heavy ion collisions," *Z. Phys. D: At., Mol., Cl.*, vol. 18, pp. 133–137, 1991.

[60] K. Rumrich, G. Soff, and W. Greiner, "Ionization and pair creation in relativistic heavy-ion collisions," *Phys. Rev. A*, vol. 47, no. 1, pp. 215–228, 1993.

[61] M. Lepy, J. Plagnard, and L. Ferreux, "Measurement of 241am l x-ray emission probabilities," *Appl. Radiat. Isot.*, vol. 66, no. 6-7, pp. 715 – 721, 2008.

[62] T. Stöhlker, A. Krämer, S. R. Elliott, R. E. Marrs, and J. H. Scofield, "Measurement of l-shell electron-impact ionization cross sections for highly charged uranium ions," *Phys. Rev. A*, vol. 56, pp. 2819–2824, 1997.

[63] R. E. Marrs, S. R. Elliott, and J. H. Scofield, "Measurement of electron–impact ionization cross sections for hydrogenlike high–z ions," *Phys. Rev. A*, vol. 56, pp. 1338–1345, 1997.

[64] H.-H. Boie, "Bremsstrahlung emission probability in the alpha decay of ^{210}Po," Ph.D. dissertation, Combined Faculties for the Natural Sciences and for Mathematics of the Ruprecht Karl University of Heidelberg, 2009.

[65] J. A. Bearden and A. F. Burr, "Re–evaluation of x-ray atomic energy levels," *Rev. Mod. Phys.*, vol. 39, no. 1, pp. 125–142, 1967.

[66] R. B. Firestone, *Table of Isotopes*, 8th ed., C. M. Baglin and S. Y. F. Chu, Eds. New York: John Wiley & Sons, 1996.

[67] H. J. Fischbeck and M. S. Freedman, "Spectroscopy of α and K- and L-electron continua and L-electron pickup in ^{210}Po α decay," *Phys. Rev. Lett.*, vol. 34, no. 4, pp. 173–176, 1975.

[68] U. Heinz, W. Greiner, and B. Müller, "Electron-translation effects in heavy-ion scattering," *Phys. Rev. A*, vol. 23, pp. 562–596, 1981.

[69] E. Ackad and M. Horbatsch, "Numerical calculation of supercritical dirac resonance parameters by analytic continuation methods," *Phys. Rev. A*, vol. 75, p. 022508, 2007.

[70] R. D. Piacentini, "Translation factors in atomic collisions," *Int. J. Quant. Chem.*, vol. 23, no. 2, pp. 567–575, 1983.

[71] L. F. Errea, L. Mendez, and A. Riera, "On the choice of translation factors for approximate molecular wavefunctions," *J. Phys. B: At., Mol.*, vol. 15, no. 1, p. 101, 1982.

[72] S. B. Schneiderman and A. Russek, "Velocity-dependent orbitals in proton-on-hydrogen-atom collisions," *Phys. Rev.*, vol. 181, pp. 311–321, 1969.

[73] B. H. Bransden, "Charge exchange in ion-atom collisions," *Contemp. Phys.*, vol. 31, no. 1, pp. 19–33, 1990.

[74] D. R. Bates and R. McCarroll, "Electron capture in slow collisions," *P. Roy. Soc. Lond. A. Mat.*, vol. 245, no. 1241, pp. 175–183, 1958.

[75] P. A. Amundsen and K. Aashamar, "Impact parameter dependence of K–shell ionisation by relativistic ions," *J. Phys. B: At., Mol.*, vol. 14, no. 21, p. 4047, 1981.

[76] R. Anholt, "Molecular theory of K-vacancy production in heavy-ion-atom collisions at small impact parameters," *Z. Phys. A: Hadron Nucl.*, vol. 295, pp. 201–208, 1980.

[77] U. Becker, N. Grün, and W. Scheid, "Cross sections for K–shell ionisation in relativistic heavy-ion collisions," *J. Phys. B: At., Mol.*, vol. 18, no. 23, p. 4589, 1985.

[78] A. I. Milstein, C. Müller, K. Z. Hatsagortsyan, U. D. Jentschura, and C. H. Keitel, "Polarization-operator approach to electron-positron pair production in combined laser and coulomb fields," *Phys. Rev. A*, vol. 73, p. 062106, 2006.

[79] K. Dietz and M. Pröbsting, "The structure of the qed vacuum and electron - positron pair production in super-intense, pulsed laser fields," *J. Phys. B: At., Mol., Opt.*, vol. 31, no. 8, p. L409, 1998.

[80] C. Müller, A. B. Voitkiv, and N. Grün, "Nonlinear bound-free pair creation in the strong electromagnetic fields of a heavy nucleus and an intense x-ray laser," *Phys. Rev. Lett.*, vol. 91, p. 223601, 2003.

[81] C. Deneke and C. Müller, "Bound-free $e+e-$ pair creation with a linearly polarized laser field and a nuclear field," *Phys. Rev. A*, vol. 78, no. 3, p. 033431, 2008.